

Measuring strain caused by ion implantation in GaN

Pedro José de Sousa Mendes

Thesis to obtain the Master of Science Degree in

Engineering Physics

Supervisors: Professor Katharina Lorenz

Doctor Sérgio Nuno Canteiro de Magalhães

Examination Committee

Chairperson: Professor Pedro Miguel Félix Brogueira

Supervisor: Doctor Sérgio Nuno Canteiro de Magalhães

Member of the Committee: Professor Rui Manuel Coelho da Silva

June 2018

Acknowledgments

I would, first and foremost, like to start to express my gratitude to my supervisors, Doctor Katharina Lorenz and Doctor Sérgio Magalhães. It was their unconditional availability to teach and guide me in everything I needed and comprehension to repeat it as many times as necessary that made the realization of this project possible. I feel extremely lucky for having had the opportunity of working with two exceptional people, both professionally and personally.

From CTN, I also want to thank Doctors Eduardo Alves and Rui Silva, for the assistance when working with the RBS/C system, Djibril Faye and Norberto Catarino, for all the help regarding the data analysis and the elaboration of this document, Jorge Rocha, for his availability to explain me the implantation process and providing some of the figures here presented, and Rita, for the yoga classes that surely helped me releasing some of the inevitable accumulated stress (not just the one inside crystalline structures). A particular mention to “Marmita Club”, for making the “social part” of this stay at CTN and providing good lunch laughs: Luís Ferreira, Helena Casimiro, Marco Peres, Miguel Sequeira, Daniela Pereira, Rita Faustino, Dirkjan Verheij and, specially, to Przemek “Nattan” Józwik, not only for having the patience to meet me on Sundays to talk about simulation software but also for his important help in interpreting the results. Dona Amália will also be remembered for her kindness in the canteen.

For the possibility of staying in Bobadela for the whole period of elaboration of this thesis, a big acknowledgment must be given to my house lord, Sr. Manuel, who provided me way more than I needed to feel at home. It is impossible to thank all my friends who contributed and motivated me for this project, however I want to mention, among others who I apologize for inevitably forgetting to write, José Silva, Bárbara Diogo, Bernardo Alegria, João Louro, João Rocha, Francisco Guerreiro, Francisco Cunha, António João Costa, Henrique Alexandre, João Costa, Nuno Simões, João Amante, José Miguel Teixeira, João Oliveira, Vítor Lobo, Paulo Costa, João Peixoto, Marta Silva, Beatriz Simões, Francisco Viana, Rodrigo Rama, Inês Almeida, Diogo Cunha, Zé Maria Bento, Pedro Réquio, Sacha Medaer and Kamila Laskowska.

My first visit to CTN took place during my second year and it was only possible due to Professor Maria José Gomes. Her total availability and attention to the problems of the people who surround her helped me crucially in a lot of seemingly unsolvable situations during the past six years. I owe her all my academic success.

Finally, my biggest acknowledgment goes to my girlfriend, Hanna, for her love and strength to fight for our relationship that makes everything seems possible, and to my family, who I cannot also mention entirely: my siblings, Maria and Filipe, tios Minda and Manel, tia Paula, tios Ico, Ana and my godson João Miguel, tios João Paulo and Inês, my grandparents and, the most important ones, my parents, Inês and Fernando. Their sacrifices to raise three children studying in universities far from our home can never be properly acknowledged, and their values and example are the reason why I am the person I am today. Thank you very much.

Resumo

O Nitreto de Gálio (GaN), cujas aplicações na tecnologia valeram a atribuição do Prémio Nobel da Física de 2014, é uma das matérias-primas mais importantes da nova geração de dispositivos optoelectrónicos. Para estudar a sua reacção à implantação iónica (dopagem), catorze amostras, sete crescidas segundo o plano *a* (não polares) e outras sete segundo o plano *c* (polares), num substrato de safira, foram implantadas com iões Árgon (Ar) com uma energia de 300 keV a temperatura ambiente. As fluências implantadas variaram entre 5×10^{12} átomos/cm² a 8×10^{15} átomos/cm². A análise estrutural subsequente foi realizada usando duas técnicas, Espectroscopia de Retrodispersão de Rutherford/Canalização (RBS/C, da sigla inglesa para Rutherford BackScattering/Channeling) e Difração de Raios-X (XRD, da sigla inglesa para X-Ray Diffraction) de alta resolução. Os resultados não só permitem especular quanto à validade da hipótese em vigor de que a deformação perpendicular causada pela implantação pode ser a força-motriz por detrás dos processos de transformação dos defeitos dentro da estrutura, mas também aparentam confirmar um nível relativo de defeitos, RDL (da sigla inglesa para Relative Defect Level), inferior para o *a*-GaN implantado com 8×10^{15} átomos/cm² em comparação com *c*-GaN com a mesma fluência de implantação, tal como foi observado previamente. Mesmo não sendo conclusivos, estes são resultados promissores numa altura em que a investigação das aplicações de nitretos não-polares em LEDs e lasers – que, em comparação com nitretos polares, evitam os fenómenos de polarização – está em constante desenvolvimento.

Palavras-Chave: Nitreto de Gálio, Implantação, Retrodispersão, Canalização, Difração de Raios-X, Deformação.

Abstract

Gallium nitride (GaN), whose applications in technology were responsible for the award of the 2014 Nobel Prize in Physics, is one of the most important groundwork materials for the new generation of optoelectronic devices. To study its reaction to ion implantation (doping) fourteen samples, seven grown along a-plane (non-polar) and another seven along c-plane (polar), on a sapphire substrate were implanted with 300 keV Argon (Ar) ions, at room temperature (RT). The implanted fluences ranged from 5×10^{12} atoms/cm² to 8×10^{15} atoms/cm². The subsequent structural analysis was performed using two techniques, Rutherford Backscattering/Channeling (RBS/C) and high-resolution X-Ray Diffraction (XRD). The results allow not only further speculation on the existing hypothesis that perpendicular strain caused by implantation may be the driving force behind defect transformation processes inside the lattice, but also seem to confirm a lower Relative Defect Level (RDL) for a-GaN implanted with 8×10^{15} at/cm², in comparison with c-GaN for the same implantation fluence, as reported previously. Even if not conclusive, these are promising results as the research on the applications of non-polar nitrides in LEDs and lasers, which, in comparison to polar nitrides, avoid polarization phenomena, is constantly developing.

Keywords: Gallium Nitride, Implantation, Backscattering, Channeling, X-Ray Diffraction, Strain.

Table of Contents

CHAPTER 1	INTRODUCTION	1
1.1	MOTIVATION AND BACKGROUND	1
1.2	OBJECTIVES AND OUTLINE	2
CHAPTER 2	STATE OF THE ART	3
2.1	GALLIUM NITRIDE STRUCTURAL PROPERTIES	3
2.2	BASIC PRINCIPLES OF ION IMPLANTATION	5
2.3	ION IMPLANTATION IN GAN.....	6
2.3.1	<i>Defect formation</i>	6
2.3.2	<i>Strain</i>	8
2.3.3	<i>Previous work</i>	9
CHAPTER 3	EXPERIMENTAL TECHNIQUES.....	13
3.1	SAMPLE GROWTH AND ION IMPLANTATION.....	13
3.1.1	<i>Sample growth</i>	13
3.1.2	<i>Ion implantation</i>	14
3.1.3	<i>Experimental equipment</i>	15
3.2	RUTHERFORD BACKSCATTERING SPECTROMETRY/CHANNELING (RBS/C).....	16
3.2.1	<i>Basic principles</i>	16
3.2.2	<i>Ion channeling</i>	20
3.2.3	<i>Experimental equipment</i>	21
3.2.4	<i>Data analysis</i>	23
3.3	X-RAY DIFFRACTION (XRD)	27
3.3.1	<i>Discovery of the x-rays</i>	27
3.3.2	<i>Laue and Bragg's contribution</i>	28
3.3.3	<i>Experimental equipment</i>	30
3.3.4	<i>Scan types</i>	32
3.3.5	<i>Data simulation software</i>	35
CHAPTER 4	RESULTS.....	39
4.1	RUTHERFORD BACKSCATTERING/CHANNELING (RBS/C)	39
4.1.1	<i>Calculation of Relative Defect Level</i>	41
4.2	HIGH-RESOLUTION X-RAY DIFFRACTION (XRD).....	43
4.2.1	<i>RaDMaX simulations</i>	46
4.1	DISCUSSION	51
CHAPTER 5	CONCLUSIONS	53
REFERENCES	55	

List of Figures

Figure 1 – Wurtzite crystal structure of GaN. Adapted from [33].	3
Figure 2 - Illustration of a) a representation of c-plane orientation in terms of Miller-Bravais indexes, b) a representation of a-plane orientation in terms of Miller-Bravais indexes and c) definition of the Miller-Bravais indexes for the wurtzite structure. Adapted from [34], [35].	4
Figure 3 – a) illustration of the different types of defects: vacancies and composition defects (substitutional and interstitial) are classified as point defects, while dislocations are line defects and consist of uncoordinated planes of atoms. b) illustrates the formation of a stacking fault, where full planes switch positions inside the lattice. Adapted from [58], [59].	7
Figure 4 - Primitive wurtzite unit cell and non-primitive zinc-blend unit cell. Open circles stand for cations, while filled circles represent anions. Adapted from [59].	8
Figure 5 - The accumulation of strain taken from XRD (left x-axis) and the maximum value of dislocation concentration profiles taken from RBS/C (right x-axis) for 320 keV Ar-implanted GaN for fluences ranging from 5×10^{12} atoms/cm ² to 3×10^{15} atoms/cm ² . Taken from Turos [29].	9
Figure 6 – The experimental relative defect level as a function of the implanted fluence for a-plane, c-plane and m-plane GaN (symbols) is compared to the simulated Hecking's model curves (represented by straight lines). Taken from Lorenz et al. [30]. These values correspond to percentages, where 1 is equal to 100%.	10
Figure 7 - Normal (perpendicular) strain, in percentage, versus the implanted Eu fluence. S1 and S2 represent, respectively, the same first and second saturations reported in [61]. Taken from [12].	12
Figure 8 - Schematic of the samples grown in both planar directions, c and a. The relation between the substrate and the film thicknesses is not at scale.	13
Figure 9 - SRIM a) Ar ion profile and b) total, Ga and N vacancies profiles. By multiplying the curve in a) by the fluence, one can obtain the concentration profile of the implanted Argon atoms. Y-axis scale presented logarithmically so that it can be easier understood the 380 nm maximum range. In b), the number of vacancies is given per Angstrom and per ion.	14
Figure 10 - Danfysik 1090 schematics. This High Current Ion Implanter model (HCII) is equipped with a CHORDIS 920 ion source. Courtesy of Jorge Rocha, LATR, CTN.	15
Figure 11 – Schematic of an elastic collision of an ion with a nucleus at the surface. The impact parameter (b) represents the deviation between the central axis of the nucleus and the trajectory of He ⁺ ; the smaller it gets, the bigger the backscattering angle is.	17
Figure 12 – The kinematic factor of N, Ar, and Ga, for a collision with a He ⁺ ion, as a function of the backscattering angle.	18
Figure 13 - SRIM calculation of the stopping power of helium in GaN. The grey dashed line represents the values of incident energy for which RBS/C is typically performed.	19
Figure 14 - Trajectory of the channeling of a particle.	20
Figure 15 - Van de Graaff accelerator schematics. Courtesy of Jorge Rocha, LATR, CTN.	21
Figure 16 – RBS experimental chamber at CTN. Motors 1 and 2 are controlled by computer and linked to the data acquisition system.	23

Figure 17 - Calibration sample (ErGeSiO) RBS spectrum. The arrows indicate the position of the surface channels for each element. 24

Figure 18 - Linear fit of the four experimental points gives the calibration curve. 25

Figure 19 - RBS spectra for an implanted and non-implanted c-GaN samples, where the aligned spectra follow the direction (0001). These spectra were shifted and normalized by using MSpectra, a Matlab code developed by Doctor Sérgio Magalhães. A minimum yield of 2.6% for as-grown sample and 5.6% for the implanted one was calculated. 26

Figure 20 - Thomas Edison and Nikola Tesla correspondence from the 1890s. Edison wrote to Tesla in 1896: "My dear Tesla, Many thanks for your letter. I hope you are progressing and will give us something that will beat Röntgen". 28

Figure 21 - Electromagnetic waves being scattered in crystallographic planes (schematic). Adapted from [90]. 29

Figure 22 - Photo of Bruker D8 Discover diffractometer. 30

Figure 23 - Bruker D8 Discover photograph of the main components used for this work. 1 – scintillation detector, 2 – place of the 0.1 mm width slit, 3 – 6-axes goniometer, 4 – two-crystal Germanium (220) monochromator to control the vertical divergence of the beam and select only the $K_{\alpha 1}$ emission line, 5 – 0.2 mm width slit, 6 – Göbel mirror, for the focusing process of the beam and to make it parallel, and 7 – X-Ray Cu source. 31

Figure 24 - Sample reference frame, illustrating the axes of rotation from the goniometer. ω refers to the incident angle, which was presented as ϑ in Figure 21. 2ϑ stands for the angle between incident and diffracted beams. D refers to the detector and X indicates the direction of the X-Rays. Adapted from [19]. 31

Figure 25 - Schematic representation of one symmetric reflection, where the atomic planes are parallel to the sample surface. The angles ω_i and ω_e are, respectively, the incident and the exit angles, while k_i and k_e are the incident wavevector and the exit wavevector. The measured planes are always perpendicular to the wave transfer vector $Q = k_e - k_i$ 32

Figure 26 - XRD 2ϑ - ω scans around the (0002) symmetric reflection for an implanted fluence of 5×10^{14} atoms/cm² sample and as-grown sample for c-GaN. The main Bragg peak corresponds to the diffraction from the deep, unimplanted GaN volume, while the lower peak at lower angle reveals the expansion of the lattice parameter in the implanted volume. The intensity is presented in arbitrary units and as a function of both the perpendicular strain and the 2ϑ angle. The diffractograms were vertically translated to achieve a better visualization of their differences. 33

Figure 27 - Comparison of a RaDMaX fit with two MROX fits, one of them including the effect of the $K_{\alpha 2}$ line. While the fitting for the same conditions for both codes is roughly the same, MROX gives a better solution when considering the $K_{\alpha 2}$ effect. The implanted fluence is of 5×10^{13} atoms/cm² for a-plane GaN. 36

Figure 28 – a) schematic of the simulation of the damage inside the sample fitted in Figure 27, with its b) strain and c) DW factor profiles. Ten layers with the same thickness were defined, with a pre-defined Gaussian-like shape for strain profile (in red) and its "mirror" for DW. The damage depth is 380 nm, from SRIM. The relation between thickness values of damaged and undamaged regions and substrate in a) is not at scale. 37

Figure 29 - Simulation of an implanted fluence of 1×10^{15} atoms/cm² for c-plane implanted GaN with MROX, which has the possibility of simulating the deep AlN layer inside the sample and indicated by the grey, dashed arrow..... 38

Figure 30 - c-GaN RBS/C spectra, aligned along the <0001> axis, for different implantation fluences, including as-grown and random spectra..... 39

Figure 31 - a-GaN RBS spectra, aligned along the <1120> axis, for different implantation fluences, including as-grown and random spectra. It is possible to identify a peak occurring between the channels 420 and 450, which was attributed to an instrumental malfunction..... 40

Figure 32 - Relative defect level profiles derived from the RBS/C spectra using a two-beam model for both planar orientations. Numbers on the right side of each row indicate the three different damage build-up stages. The distributions of argon and vacancies simulated using the code SRIM are included for comparison, with arbitrary units. The area between 100 and 150 nm is highlighted as it corresponds to the depth window used to plot the damage build-up (Figure 33)..... 41

Figure 33 - Damage build-up curves. Simulated curves using Hecking's model at 15 K [30], [71] are shown for comparison with measured points (symbols and dashed lines) for both a-GaN and c-GaN..... 42

Figure 34 - XRD diffractograms (symbols) around the (0002) reflection for c-GaN (a) and the (1120) reflection for a-GaN (b), implanted to different fluences. For the lower x-axis, the 2θ angle was converted to perpendicular strain. The low-intensity peaks at the high angle side of the main peak (more evident for a-GaN) are attributed to instrumental artifacts due to an incomplete filtering of the $K_{\alpha 2}$ Cu X-Ray line by the monochromator. Fluences are expressed in 10^{14} atoms/cm². Lines indicate RaDMaX fits and as it is easier to distinguish lines from dots, the legend is given in function of the lines. The diffractograms were vertically translated to achieve a better visualization of their differences. 44

Figure 35 - Comparison between both planar orientations. a) indicates the value of strain for the damage peak per fluence, while b) indicates the relative "height" of the peak, calculated as the quotient between the intensity of the peak attributed to the implanted volume and the one of the main Bragg peak. Fluences range from 5×10^{13} at/cm² to 2×10^{15} at/cm². 45

Figure 36 - Strain profiles derived using the RaDMaX code for a) c-GaN and b) a-GaN as a function of depth. The range of 380 nm for the depth axis corresponds to the maximum argon atom range obtained from SRIM simulations. The SRIM vacancy-profile is included for comparison with arbitrary units..... 46

Figure 37 - DW factor profiles derived using the RaDMaX code for a) c-GaN and b) a-GaN as a function of depth, corresponding to the strain profiles presented in Figure 36. The range of 380 nm for the depth axis corresponds to the maximum argon atoms range obtained from SRIM simulations..... 47

Figure 38 - Alternative strain profiles derived using the RaDMaX code for the fitting of the diffractograms of five a-GaN samples as a function of depth. The range of 380 nm for the depth axis corresponds to the maximum range of the argon atoms obtained from SRIM simulations. The SRIM vacancy-profile is included with arbitrary units. The red profile has been taken from Figure 36b for comparison. 48

Figure 39 - Alternative RaDMaX fits to the diffractograms for a-GaN samples implanted with fluences ranging from 5×10^{13} at/cm² to 2×10^{15} at/cm², following the strain profiles presented in Figure 38. 49

Figure 40 - Comparison of the experimental data with as-grown sample diffractograms for a-GaN. The grey window indicates the range where the negative strain values from all fluences showed in Figure 38 falls. 50

Figure 41 - Alternative DW Factor profiles for the fitting of the diffractograms of five a-GaN samples as a function of depth. The range of 380 nm for the depth axis corresponds to the maximum range Argon atoms reach from SRIM simulations. The red profile has been taken from Figure 37b for comparison. 50

Figure 42 - RDL (relative defect level) and strain values for the depth window and regimes presented in Figure 32 as a function of the fluence. 51

List of Tables

Table 1 - wurtzite-GaN main characteristics at 300 K..... 5

Table 2 - Kinematic factor values for erbium, germanium, silicon, and oxygen. This calculation allows us to determine the relationship between energy and channels. 24

List of symbols and acronyms

a-GaN	a-plane oriented gallium nitride
AlN	Aluminum nitride
at/cm²	Atoms per square centimeter
c-GaN	c-plane oriented gallium nitride
CTN	Campus Tecnológico e Nuclear
DECO	DEfect COncentration
DW	Debye-Waller (factor)
FET	Field Effect Transistor
GaN	Gallium nitride
LATR	Laboratório de Aceleradores e Tecnologias de Radiação
LED	Light Emission Diode
LT	Low Temperature
MOVPE	MetalOrganic Vapour Phase Epitaxy
MROX	Multiple Reflection Optimization package for X-ray diffraction
RaDMaX	Radiation Damage in Materials analysed with X-ray diffraction
RBS/C	Rutherford Backscattering Spectrometry/Channeling
RDL	Relative Defect Level
RT	Room Temperature (300 K)
SiN	Silicon nitride
SRIM	Stopping and Range of Ions in Matter
XRD	X-Ray Diffraction
TEM	Transmission Electron Microscopy
TRIM	TRansport of Ions in Matter
UV	Ultraviolet

Chapter 1 Introduction

1.1 Motivation and background

Gallium nitride (GaN), discovered in 1932 [1] is a chemical compound which belongs to the family of the III-nitride compounds (gallium, the cation, is an element in the group 3 of the periodic table and has an abundance on Earth of 13 ppm). Gallium nitride and associated semiconductor devices are among the most important optoelectronics breakthroughs of the last decades. Ever since the development of Shuji Nakamura's first GaN-based light-emitting diodes (LEDs) [2] in the early 90s, which would later win 2014 Nobel Prize in Physics *"for the invention of efficient blue light-emitting diodes, which has enabled bright and energy-saving white light sources"* [3], nitride-based semiconductors became worldwide known. GaN-based violet lasers are the groundwork of the Blu-Ray system, one of the examples of new generation's optical data storage processes [4]. This format made it possible to increase the information storage capacity of an optical disc from 4.7 Gb to 54 Gb. High-Electron Mobility Transistors (HEMTs) and Field-Effect Transistors (FETs) are other technologically relevant examples of the applications of GaN electronics [5], [6].

The turning point usually regarded for the start of the popularity of GaN-based devices was the improvement of the crystalline, optical and morphological properties of GaN thin films grown by MOVPE (MetalOrganic Vapor Phase Epitaxy) following a two-step growth on a c-plane Al₂O₃ (sapphire) substrate [7]. Its potential to overcome the performance of Silicon in conducting electrons from 10 to 1000 times, as well as presenting a higher reliability [6], [8] make GaN the leading candidate to allow Moore's law [9], predicted to be outdated in the next few years, to remain as accurate as ever.

Semiconductors are characterized by the possibility of modulating their conducting properties by an intentional and controlled introduction of external elements into their crystalline structure. Three key material properties are fundamental to host ion implantation doping for optical application: damage resistance, thermal stability and wide direct bandgap [10], and these are all characteristics of GaN and related materials, making them excellent candidates. Ion implantation allows both controlling the local dopant distribution and introducing more than one dopant while the solubility limits can possibly be overcome. However, this technique also presents an important drawback as it creates structural defects in the crystal lattice, which highly diminishes the optical performance.

One of the most efficient techniques to study implantation damages is the Transmission Electronic Microscopy (TEM), which provides the possibility of determining the nature of implantation defects by a direct observation of these; for this reason, while this technique has not been used to perform this work, references to the work of several groups on TEM will be frequent [11]–[15]. Other techniques include Rutherford Backscattering Spectrometry/Channeling (RBS/C) [16], [17] – to determine the dependence of defects with depth – and X-Ray Diffraction (XRD) [18], [19], which provides an overview of the strain caused by the creation of structural defects as well as techniques

probing the optical and electric properties of the materials. While c-GaN implantation has been widely studied [20]–[29], there are considerably fewer articles regarding a-GaN – which has been pointed out as being more resistant and presenting distinct extended defects [30], [31]. It is proposed that strain caused by implantation defects is one of the driving forces for the formation of extended defects [11], [15], [29], so by measuring it both damage and annealing processes can be better comprehended.

1.2 Objectives and outline

The goal of this Master's dissertation is to study and compare the argon-implantation damage formation in gallium nitride grown following the a-plane orientation and the c-plane orientation (usually referred henceforward as a-GaN and c-GaN). This will continue the work presented in [30] using a combination of RBS/C and TEM, with the improvement of using the XRD technique to complement this data and analyze an implantation process in similar conditions and to compare those results with the published literature. We aim to understand the strain caused by ion implantation because it is believed that it is the cause of the atoms' motion in the lattice leading to defect transformation [29] and this has not been studied in a-GaN yet.

The choice of implanting Argon relies on the fact that it is an inert element. While its implantation is used for fundamental research only, it plays a key role in understanding how other dopants behave – structural defects are the same regardless of the implanted atom –, thus contributing to a better understanding of the potential applications of ion implantation for the fabrication of GaN-based electronics.

While the sample growth process took place in the group of Prof. Scholz at the Institute of Optoelectronics, University of Ulm, Germany, all the subsequent phases of this project, from the implantation of the samples to the experimental techniques and data analysis was performed at LATR (Laboratory of Accelerators and Radiation Technologies) at Campus Tecnológico e Nuclear, Instituto Superior Técnico, Lisbon.

The structure of this thesis includes five chapters, organized via the following outline:

- **Chapter 1**, presenting the motivation and objectives for this work;
- **Chapter 2**, consisting of an overview on the state-of-the-art regarding ion-implantation and the study of induced strain in GaN;
- **Chapter 3**, introducing the experimental techniques and the software used for both data acquisition and data analysis;
- **Chapter 4**, describing and treating the experimental results and comparing both techniques;
- **Chapter 5**, briefing the most relevant conclusions to retain from the presented data in the previous chapter and giving some suggestions for future work.

Chapter 2 State of the art

2.1 Gallium nitride structural properties

III-nitrides present two common crystal structures, zinc-blende, and wurtzite, being the latter the most stable structure for GaN. This structure is characterized by two parameters, “c” and “a”. C-planes are polar planes as they contain either only gallium or nitrogen atoms, while a-planes present the same number of each element: by imagining a replication of the crystalline structure presented in Figure 1, four Ga^{3+} ions are shared at the corner between six hexagonal cells each ($4/6 \times 3^+$ charges) and two N^{3-} ions are shared between three hexagonal cells each ($2/3 \times 3^-$ charges), thus a-planes are non-polar planes [32].

Figure 1 presents a schematic of GaN crystalline wurtzite structure, including the crystallographic planes relevant for this work.

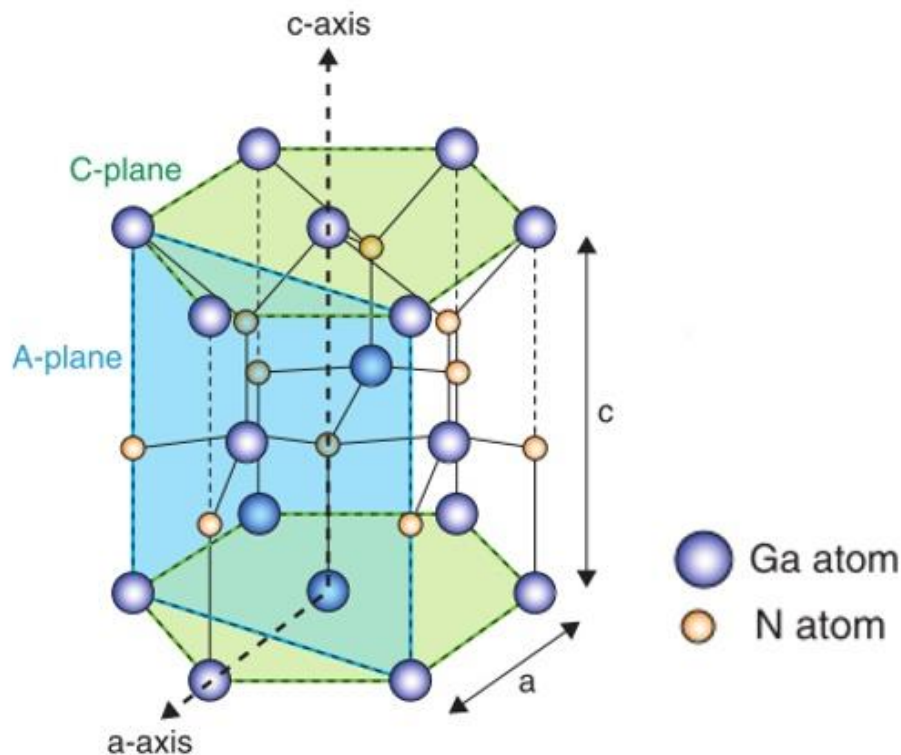


Figure 1 – Wurtzite crystal structure of GaN. Adapted from [33].

It is usual to identify the various planes on a wurtzite structure by using the so-called Miller-Bravais indexes $hkil$, where $-i = h + k$ is defined to better understand the similarity of the planes parallel to the c-axis. Figure 2 illustrates the definition of the Miller-Bravais indexes and the sketch of c- and a-planes. The four indexes $[hkil]$ are related to the three unitary vectors **a**, **b**, **d** and **c**, respectively. According to the Miller-Bravais indexes system, the c-orientation is defined as $\langle 0001 \rangle$ and the a-orientation comes as $\langle 11\bar{2}0 \rangle$ by permutation of the indexes [34]. Each GaN wurtzite lattice

contains two c-planes (represented in green on Figure 1) and six a-planes (represented in blue on Figure 1), where c-planes are perpendicular to a-planes.

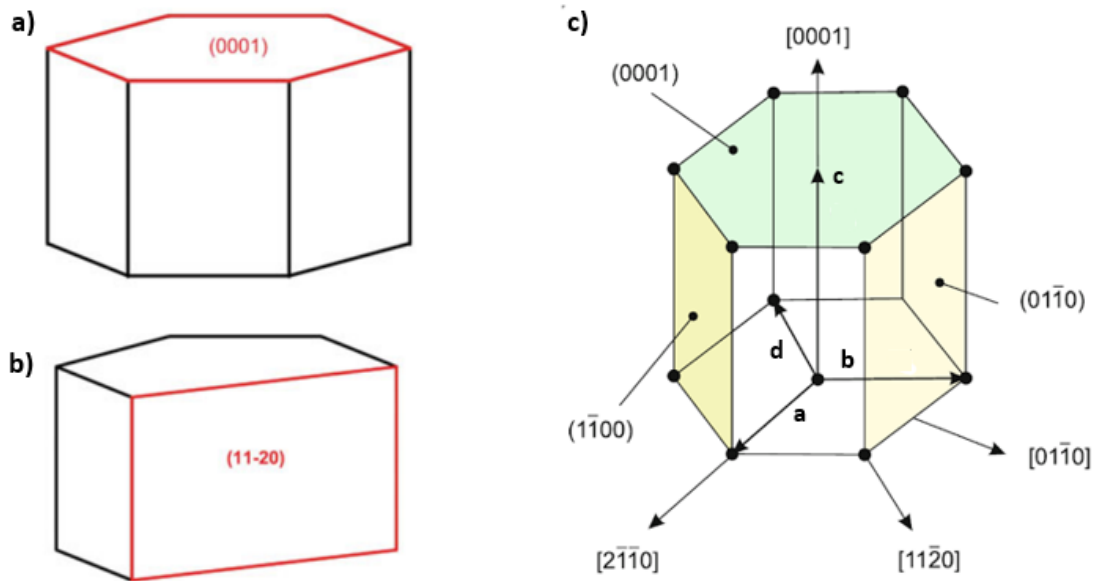


Figure 2 - Illustration of a) a representation of c-plane orientation in terms of Miller-Bravais indexes, b) a representation of a-plane orientation in terms of Miller-Bravais indexes and c) definition of the Miller-Bravais indexes for the wurtzite structure. Adapted from [34], [35].

The wurtzite structure has two interpenetrating hexagonal sublattices, where every atom of each element is surrounded by four of the other element. Its lattice parameter values are widely reported in the literature for relaxed crystals [36], [37], however, these parameters can be influenced by the free-electron concentration, defects, impurities or strain [38].

The energy required in GaN to promote an electron from the valence band to the conduction band, thus originating a current flow, is of 3.4 eV [33], [39], making this material a wide bandgap semiconductor – it is also defined as direct bandgap because the crystal momentum of holes and electrons is the same in both bands. This value corresponds to an emission wavelength of 365 nm. GaN is considered as a very good thermal conductor, a quantity that has been shown to decrease with the doping density [40], [41]. This characteristic makes applications of GaN in optoelectronics and high-power/high-temperature very promising.

As mentioned before, GaN films are usually grown on sapphire substrates [7], whose lattice parameters are different between both materials thus creating a so-called lattice mismatch of 14-16% [38], [42]. Even with the introduction of AlN and SiN_x buffer layers [7], [43]–[45] to reduce this mismatch, it cannot be entirely eliminated. Adding up to the different thermal expansion coefficients between film and substrate, tensions will inevitably be created on the grown films. It has been shown that piezoelectric and spontaneous polarizations are present in GaN films grown on the c-plane (polar), attributed to the macroscopic polarization between III-V nitrides heterojunctions [46]. This phenomenon affects the optoelectronic properties of devices such as LEDs and lasers, so the

research on the growth of non-polar films [32], [42], [47] is becoming popular in the past years as they have been shown to overcome this problem [48].

Table 1 summarizes some of the properties of GaN at room temperature (RT). The calculated molar mass is of 83.2254 g/mol. Further information on other GaN characteristics (such as binding and cohesive energies) can be found in references [49], [50].

Crystalline structure	wurtzite
Space group	$C_{6v}^4-P6_3mc$ [51]
Density (g/cm ³)	6.15 [51]
Atomic density (10 ²² atoms/cm ³)	8.9 [51]
a_0 lattice parameter	0.3189 Å [51]
c_0 lattice parameter	0.5186 Å [51]
Bandgap (eV)	3.39, direct [51]
Average displacement energies (eV)	45 eV – Ga [25] 109 eV – N [25]

Table 1 - wurtzite-GaN main characteristics at 300 K.

2.2 Basic principles of ion implantation

Ion beam processing of materials results from the introduction of atoms into a solid substrate by bombardment of the material with ions typically within the energy range from tens of kiloelectron-volts to few megaelectron-volts. Optical, mechanical, electrical, magnetic and superconducting properties are all affected (or even dominated) by the presence of the implanted atoms. Using energetic ions allows introducing a wide variety of atomic species independently of thermodynamic factors – making it conceivable to obtain impurity concentrations and distributions of interest which otherwise would not be attainable. These benefits have been stimulated by the opportunities of synthesizing novel materials with eventual applications in the tribological, corrosion, semiconductor and optical fields. Ion beam processing provides an alternative and non-equilibrium technique of introducing dopant atoms into a matrix [10].

One of the most important considerations in any description of ion-solid interactions is the depth/range distribution of the implanted ions. Furthermore, lattice disorder and radiation-damage effects are produced in the crystal by the incident ion. Collisions between ions and target atoms result in the slowing down of the ion, and the energy loss resulting from nuclear and electronic stopping contributes significantly to determining the ion's range. As this energy is transferred to lattice atoms, then enough energy may be relocated from the ion to displace an atom from its lattice site. Lattice atoms that are displaced by incident ions can, in turn, displace other atoms, thus creating a cascade of atomic collisions. This leads to a distribution of vacancies, interstitial atoms and other types of disorder in the region around the ion and recoil tracks. As the number of incident ions increases the individual

disordered regions begin to overlap, which leads to the formation of a heavily damaged layer. The total amount of disorder and the distribution in depth depend on ion species (in particular mass), energy, temperature, channeling effects, flux and total fluence as well as the host material itself [10].

The energy required to displace a lattice atom permanently represents the displacement threshold. If in the collision process the energy transfer to the lattice atom is less than both the binding and displacement energies, the struck atom undergoes large amplitude vibrations without leaving its lattice position. If it is higher than the binding energy but smaller than the displacement energy, the atom will momentarily leave its position; however, no Frenkel-pairs will be created as the atom will eventually return to its original position. If the energy transfer is higher than the displacement energy, it can move out of the potential well that represents its stable lattice site and move off into the lattice as a displaced atom, which leaves a vacancy and occupies an interstitial site in the lattice (*Frenkel defect*). A range of displacement energies exist for the creation of this defect, as it depends on the direction of the momentum of the target atom. A weighted average over the displacement directions leads to an average displacement energy; regarding GaN, the threshold displacement energy for gallium is ~45 eV and that for nitrogen is ~109 eV in GaN [25].

The first implantation study in c-plane GaN took place in 1974 [20] when Pankove and Hutchby studied its photoluminescence following Zn implantation. Nearly 20 years ago, Tan *et al.* [21] observed that low fluence implantation, followed by 1100 °C annealing, created a wide defect network, while for high fluences it could lead to amorphization. Kalinina *et al.* presented a study of Mg implanted GaN p-n junctions [22]. Kucheyev *et al.* reviewed early studies on the ion-beam processing of GaN in 2001 [23]. The same Australia-based group typically combined RBS/C and TEM techniques to study ion bombardment in $\text{Al}_x\text{Ga}_{1-x}\text{N}$ films [26]. All these studies were performed on thin films grown following the c-plane orientation. The effects of ion implantation are characterized by strong dynamic annealing [23], [26], [52], i.e. point defects created during the implantation are very mobile and can either recombine or gather to form extended defects such as stacking faults and dislocation loops during the implantation process [28], [42]. The diffusion and formation/annealing of defects has been widely studied [13], [23], [52]–[54].

2.3 Ion implantation in GaN

2.3.1 Defect formation

Ion implantation and subsequent thermal processing will form defects, which may be categorized as point, line, planar and volume defects. A point defect is a deviation in the periodicity of the lattice arising from a single point. Other defects, such as dislocations and stacking faults, extend over many lattice sites. For semiconductors, point defects not only cause structural disturbances but also often introduce electronic states in the band gap. If an attractive potential exists between a native defect and an impurity atom, they may interact and form a defect complex such as a vacancy-impurity pair [10].

Line defects in a crystalline material are known as dislocations, which are formed in processes such as ion implantation, thermal processing, and epitaxial growth. Under local equilibrium unchanged conditions, dislocations may form in GaN, creating a surface pit whose size will be affected by the growth kinetic process [55]. Native point defects, which consist of interstitials, vacancies and Frenkel defects (vacancy created by an atom moving to an interstitial site) [10], along with substitutional ones, are represented in Figure 3a.

Planar defects include grain boundaries, twins and stacking faults. These defects are also formed during ion implantation and thermal processing, and all the three types are enclosed by a single dislocation or by an array of dislocations separating the faulted area from the normal one or delineating the lack of orientation between various areas of the semiconductor. Stacking faults, shown in Figure 3b, in GaN can be created during crystal growth processes [42], [56] or formed during implantation [28], [29] and very high temperatures are needed to remove them during annealing [57]. Volume defects include voids and local regions of different phases, such as a precipitate or an amorphous phase [10].

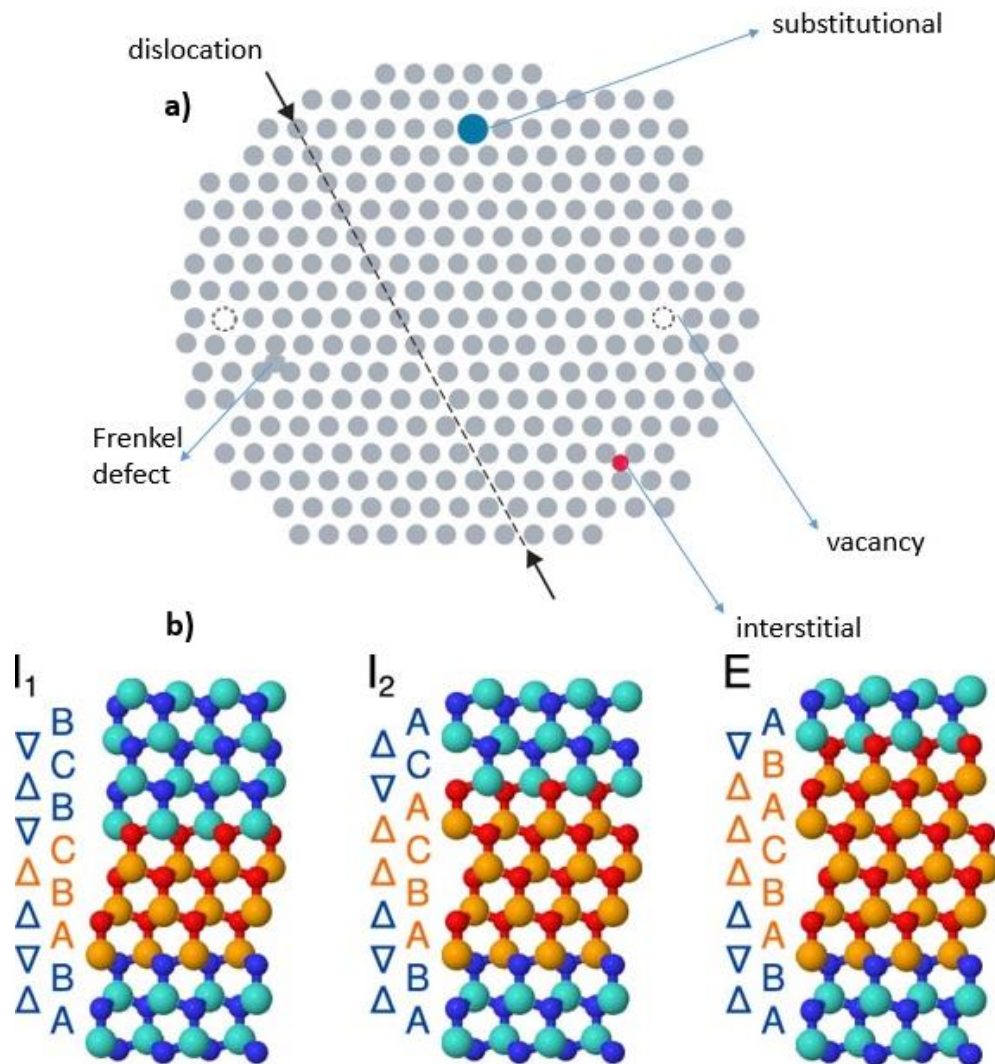


Figure 3 – a) illustration of the different types of defects: vacancies and composition defects (substitutional and interstitial) are classified as point defects, while dislocations are line defects and consist of uncoordinated planes

of atoms. b) illustrates the formation of a stacking fault, where full planes switch positions inside the lattice. Adapted from [58], [59].

To better understand Figure 3b, one must take into consideration the differences between wurtzite and zinc-blende structures, a cubic structure which represents another possibility for the crystallization of GaN, as shown in Figure 4.

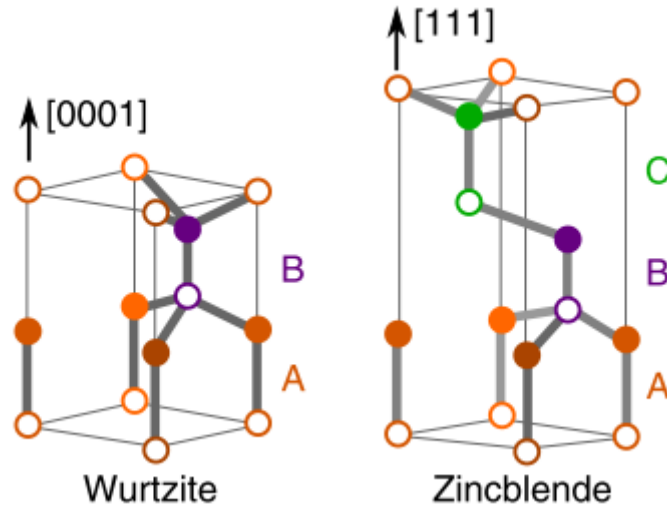


Figure 4 - Primitive wurtzite unit cell and non-primitive zinc-blend unit cell. Open circles stand for cations, while filled circles represent anions. Adapted from [59].

Along the stacking directions marked in Figure 4, cation and anion form pairs and are always located on the same lateral position inside the structure, hence the “A”, “B” and “C” terminology to represent the stacking order. For wurtzite-GaN, stacking faults will consist in the insertion of zinc-blend sequences inside its matrix (in orange in Figure 3) [59], which would normally present an ABABABAB... sequence. In Figure 3b, I_1 and I_2 indicate intrinsic stacking faults – the change happens, for example, from AB to BC or AC and replicates inside the structure – while E stands for extrinsic stacking fault, where, in this case, an extrinsic C layer is inserted in the middle of the normal sequence [59]. The arrows indicate, if pointing up, an $A \rightarrow B$, $B \rightarrow C$ or $C \rightarrow A$ succession, and vice-versa if pointing down [59]. Stacking faults are typically observed in ion-implanted c-GaN, and most of them consist of type I_1 [28].

2.3.2 Strain

The study of strain in GaN and related materials has been going on since the end of last century, as ion bombardment has been shown to induce strain and expand GaN lattice parameters [12], [27], [60]–[63]. This study is usually performed with the X-Ray Diffraction technique, which allows, among a big range of possibilities, the determination of the lattice parameters of the material, providing information on the perpendicular induced strain [19].

In the past years, several groups have been developed models to describe the evolution of strain profiles inside crystalline lattices [62], [64]–[66], which have then turned into simulation codes [62], [63], [67], [68]. This is justified by the recent proposal for the strain to be one of the driving forces of defect transformation [11], [29]. Figure 5 illustrates the dependence of the concentration of dislocations (extended defects which may be created by the accumulation of point defects) and the accumulated strain on Ar-ion fluence for implantation of c-plane GaN [29].

Regarding the comparison of strain between a-plane and c-plane orientations, Catarino *et al.* [31] showed an expansion of the *a* parameter when implanting a-GaN and the *c* parameter when implanting c-GaN, thus, an expansion of the perpendicular parameter – with respect to the surface, for each planar orientation – following implantation damage. Recently, a mechanism to explain the development of strain in irradiated materials was proposed, taking into account the transformation of clusters of point defects into extended defects which will, first, induce elastic strain, and second, merge into a net of dislocation lines and allow a strain relaxation [69].

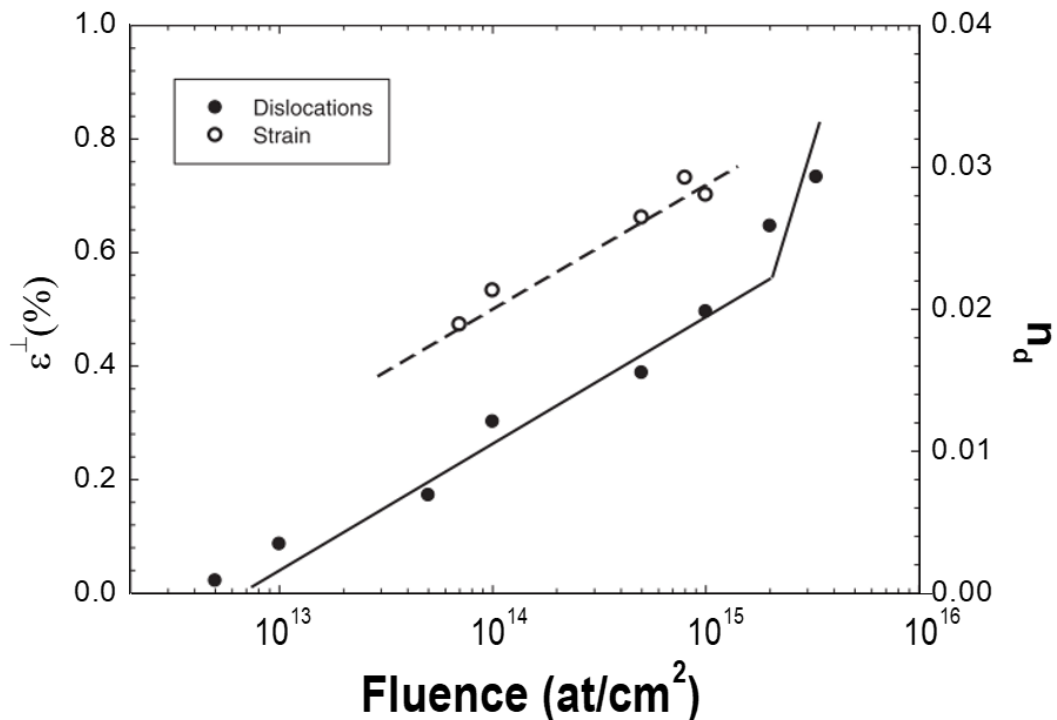


Figure 5 - The accumulation of strain taken from XRD (left x-axis) and the maximum value of dislocation concentration profiles taken from RBS/C (right x-axis) for 320 keV Ar-implanted GaN for fluences ranging from 5×10^{12} atoms/cm² to 3×10^{15} atoms/cm². Taken from Tuross [29].

2.3.3 Previous work

The most recent work of our group [30] presented an overview of the differences between the implantation effects in GaN thin films grown along different crystallographic directions. 300 keV Argon ions at 15 K with fluences ranging between 2×10^{12} and 4×10^{16} atoms/cm² were implanted in a-, c- and m-plane surface oriented epitaxial GaN layers. Similar fluence values have been implanted at 300

K for the elaboration of this Master's thesis, as it has been observed that thermal effects on damage formation mechanisms in GaN appear to be of small importance [14], [29].

It is possible to identify three steps of damage build-up in Figure 6, which correlates the Relative Defect Level (RDL) taken from RBS/C analysis with the implanted fluence. This behavior has been studied previously [11], [14], [29], [52], [70]. These steps are intercalated by two regimes (II and IV) where the RDL either saturates or its increase is residual. For the first and second steps (regimes I and III), the increase of RDL occurs quite steeply, while the last regime (V), indicates a saturation and the point where nanocrystallisation occurs, firstly for c-GaN, secondly for m-GaN and, at last, for a-GaN.

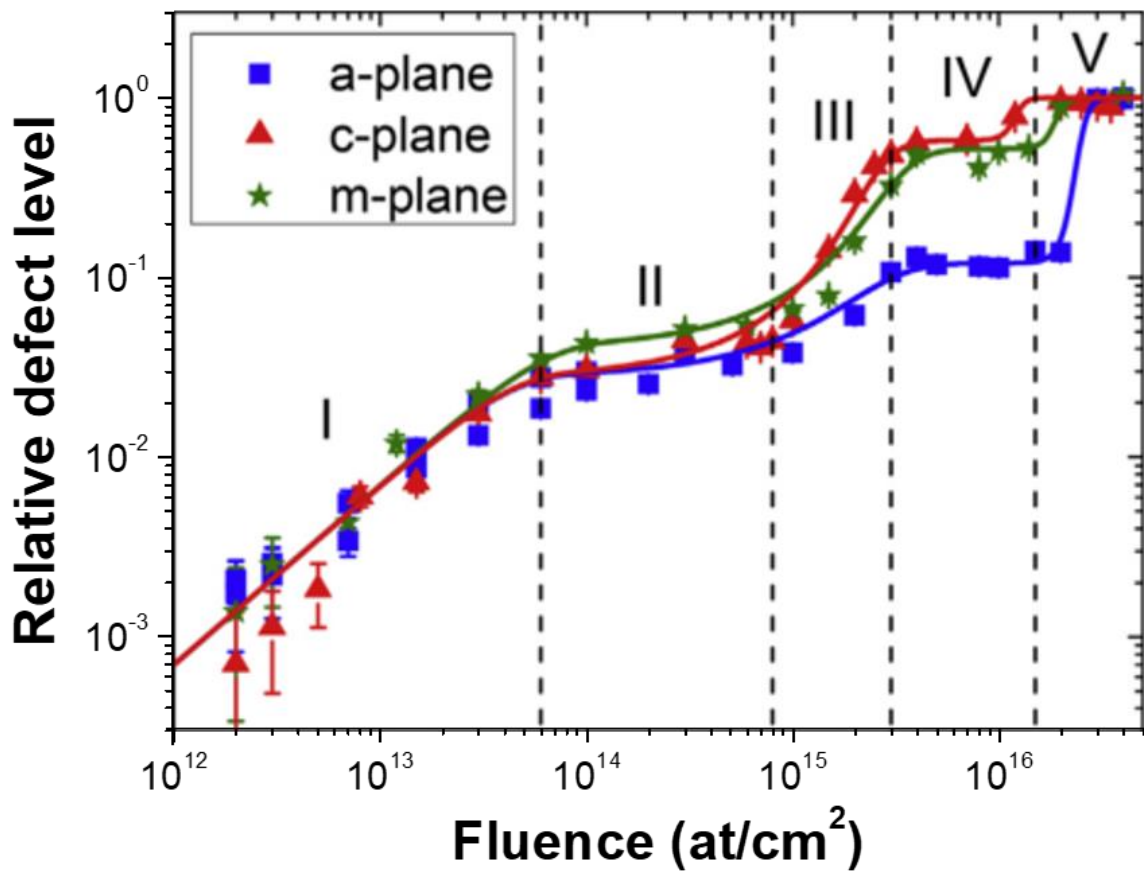


Figure 6 – The experimental relative defect level as a function of the implanted fluence for a-plane, c-plane and m-plane GaN (symbols) is compared to the simulated Hecking's model curves (represented by straight lines). Taken from Lorenz et al. [30]. These values correspond to percentages, where 1 is equal to 100%.

These steps can be well described using the defect formation and recombination model proposed by Hecking *et al.* [70], [71] and shown in Figure 6. This model proposes a continuous amorphous layer being stimulated by previously amorphized volumes. It can be described by two equations, taken from [30], [71], one for point defect formation and another for nanocrystallisation/amorphization. GaN was seen to nanocrystallise at the surface at room temperature [13], [28] and low temperature [30].

$$\left\{ \begin{array}{l} \frac{dn_{pd}}{d\phi} = P_{pd} e^{-R_{pd}^2 \phi^2} (1 - n_a) + C_{pd} n_{pd}^{1.2} \left[1 - \frac{n_{pd}}{n^*(1 - n_a)} \right] - \frac{dn_a}{d\phi} \frac{n_{pd}}{1 - n_a}, \\ \frac{dn_a}{d\phi} = (P_a + G_a n_a)(1 - n_a). \end{array} \right. \quad (1)$$

$$\left. \begin{array}{l} \end{array} \right\} \quad (2)$$

Equations 1 and 2 represent the fluence dependence of the formation of radiation damage, which is given by the relative concentration of point defects n_{pd} (sole or clustered) and amorphous/nanocrystallised regions (represented by n_a or, analogously, n_{nc}) [30], [71]. P_{pd} is the cross-section for point defect formation, R_{pd} represents the cross-section for point defect recombination and C_{pd} stands for the cross-section for the formation of defect clusters – with a saturation concentration of n^* . P_a describes the primary creation of amorphous nuclei, G_a is a measure of the “stimulated amorphisation” phenomenon (and both have the dimensions of cross-sections) while, finally, Φ stands for the implanted fluence [30], [71].

Regarding XRD, it has been recently shown that it loses sensitivity for c-GaN at high implantation fluences by our group. Faye *et al.* [61], following a 200 keV Argon implantation at room temperature (RT), showed a first strain saturation at around 0.5%, occurring for fluences ranging from 1×10^{15} at/cm² to 2×10^{16} at/cm², which was suggested to occur due to the formation of a layer of stacking faults previously observed for Eu-implantation [12]. It was also noted that for fluences ranging from 2×10^{15} at/cm² to 2×10^{16} at/cm² the shape of the diffractograms did not change any further, interpreted as an indication of a second strain saturation at around 1.8% not just on a specific implanted region but throughout the whole implanted material [61]. Furthermore, we detected that strain saturation occurred at a lower fluence in comparison to the RDL saturation threshold, thus indicating an insensitivity of the XRD technique at high fluences. It was suggested a change in the microstructure to explain this strain saturation [61].

This behavior has also been previously observed by Lacroix *et al.* [12], following a 300 keV Eu implantation in c-GaN. Figure 7 shows the evolution of the perpendicular strain as a function of the implanted fluence. It is possible to identify that the values for the first and second saturations are approximately the same in both articles.

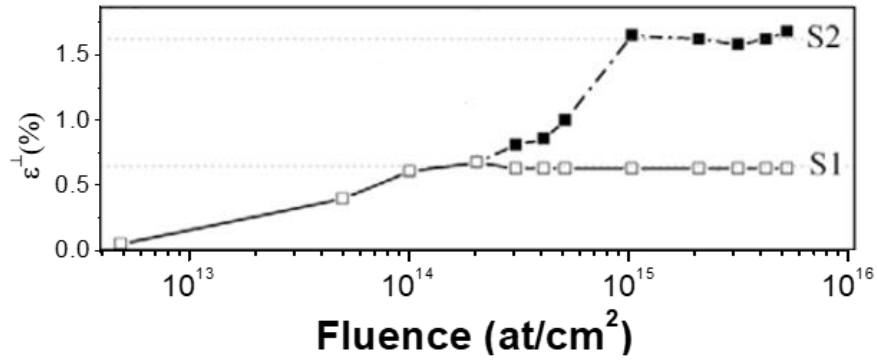


Figure 7 - Normal (perpendicular) strain, in percentage, versus the implanted Eu fluence. S1 and S2 represent, respectively, the same first and second saturations reported in [61]. Taken from [12].

Both a-, c- and m-planes showed bimodal damage profiles with two peaks, one surface peak corresponding to the accumulation of migrating point defects and a broader one at deeper regions as reported previously [23], [72]. Lorenz *et al.* [30] have shown that a-plane Ar-implanted GaN is the planar orientation less affected by radiation damage in the fluence region from 10^{15} to 3×10^{16} at/cm², whose higher resistance had been seen for Eu-implantation previously [31]. Different microstructures created following the implantation damage processes have been described in both articles as the cause of these results. Liliental-Weber *et al.* have also previously observed that the defects formed during the growth of GaN thin films on sapphire substrates present differences when considering polar or non-polar orientations [42].

Chapter 3 Experimental Techniques

3.1 Sample growth and ion implantation

3.1.1 Sample growth

Our wafers were kindly provided by Prof. Scholz, Institute of Optoelectronics, University of Ulm, and grown via MOVPE – Metal Organic Vapor Phase Epitaxy. This technique was developed in 1968 [73]. In MOVPE, precursor elements – in our case, ammonia (NH_3), trimethylgallium (TMGa) and trimethylaluminum (TMAI), the latter one originating AlN – are transported by a carrier gas (in this case, Pd-diffused H_2) to the substrate, where these precursors will take part in several chemical reactions at the surface. This technique is widely used to produce LEDs, FETs, photovoltaic cells and a more detailed explanation is provided by Waser in his book [74].

Both a-plane and c-plane GaN samples had sapphire (Al_2O_3) starting substrates [75], respectively, r-oriented and c-oriented. Regarding c-plane samples, the film is about $2.75\ \mu\text{m}$ thick and, to compensate the lattice mismatch and the large thermal coefficient of wurtzite GaN to Al_2O_3 , the initial growth step before the deposition of GaN was a thin AlN nucleation layer [44]. This was found not to be enough and was followed by a SiN layer at around $500\ \text{nm}$ of GaN, which has been shown to reduce the dislocation density and reduce the defects [45].

For a-plane samples, almost two times thicker ($5.2\ \mu\text{m}$), an initial high-temperature AlN layer is deposited via MOVPE, followed by $5.2\ \mu\text{m}$ of GaN [76]. Its growth was interrupted twice to deposit two SiN layers, proved to have the same defect reduction as for c-GaN [43], at the nominal positions of $0.3\ \mu\text{m}$ and $1.0\ \mu\text{m}$. Figure 8 shows a schematic of the samples.

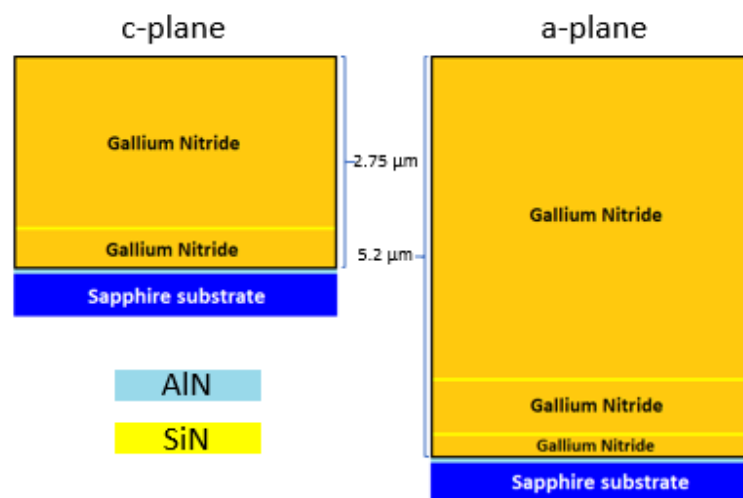


Figure 8 - Schematic of the samples grown in both planar directions, c and a. The relation between the substrate and the film thicknesses is not at scale.

3.1.2 Ion implantation

Argon was implanted at room temperature, with an energy of 300 keV and a 7° incident angle between the beam and the sample normal – which is a typical value used to minimize channeling effects. It is possible to simulate its profile with Monte Carlo simulations by using the code SRIM – the Stopping and Range of Ions in Matter [77], by using the displacement energies referred on the previous chapter as input alongside with the composition of the layer (gallium and nitrogen with 1:1 ratio) and its density, 6.15 g.cm^{-1} as well as and the threshold displacement energy for the two constituents. The current density of the implantation beam ranged from $0.1 \mu\text{A/cm}^2$ (lowest fluence) to $1.7 \mu\text{A/cm}^2$ (highest fluence).

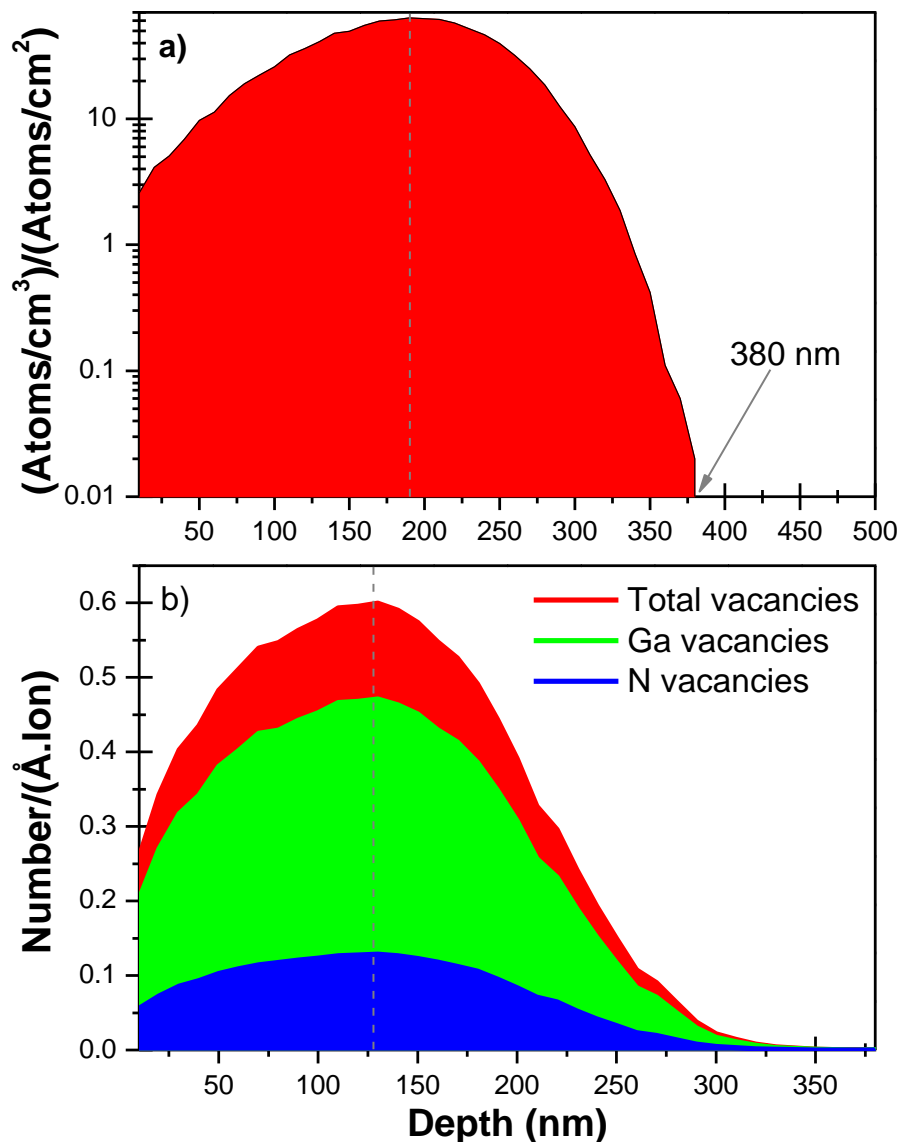


Figure 9 - SRIM a) Ar ion profile and b) total, Ga and N vacancies profiles. By multiplying the curve in a) by the fluence, one can obtain the concentration profile of the implanted Argon atoms. Y-axis scale presented logarithmically so that it can be easier understood the 380 nm maximum range. In b), the number of vacancies is given per Angstrom and per ion.

After providing the input, we are now able to analyze the results of the simulations. Figure 9 illustrates both the ion distribution and the vacancy profiles. An arrow indicates the maximum range at 380 nm, a value that is crucial to understand the results presented in this work. The maximum of the concentration of Ar occurs at a depth of 190 nm, while the higher number of vacancies is predicted to occur at around 130 nm depth.

The implantation of Argon in GaN was performed at the LATR, Campus Tecnológico e Nuclear. The chosen implanted fluences were, for seven samples grown on each planar orientation, 5×10^{12} at/cm², 5×10^{13} at/cm², 2×10^{13} at/cm², 5×10^{14} at/cm², 1×10^{15} at/cm², 2×10^{15} at/cm² and 8×10^{15} at/cm². These values present uncertainties between 7% (highest fluence, beam current of 15 μ A) and 9% (lowest fluence, beam current of 8 μ A).

These values correspond to, considering the different regimes shown in the damage build-up curves presented in section 2.3.3 from the work of Lorenz *et al.* [30] at 15 K, to the regimes I (5×10^{12} – 5×10^{13} at/cm²), II (2×10^{14} – 5×10^{14} at/cm²), III (1×10^{15} – 2×10^{15} at/cm²) and IV (8×10^{15} at/cm²). There has, however, been reported by Wendler *et al.* [14] and Turos [29] a higher fluence threshold for the transition between regimes at room temperature (RT), meaning that our chosen values will correspond to just three regimes at RT. The reason for not having implanted fluences higher than 8×10^{15} at/cm² is due to the XRD low-sensitivity for higher fluences, shown by Faye *et al.* [61] and explained on the same section aforementioned.

3.1.3 Experimental equipment

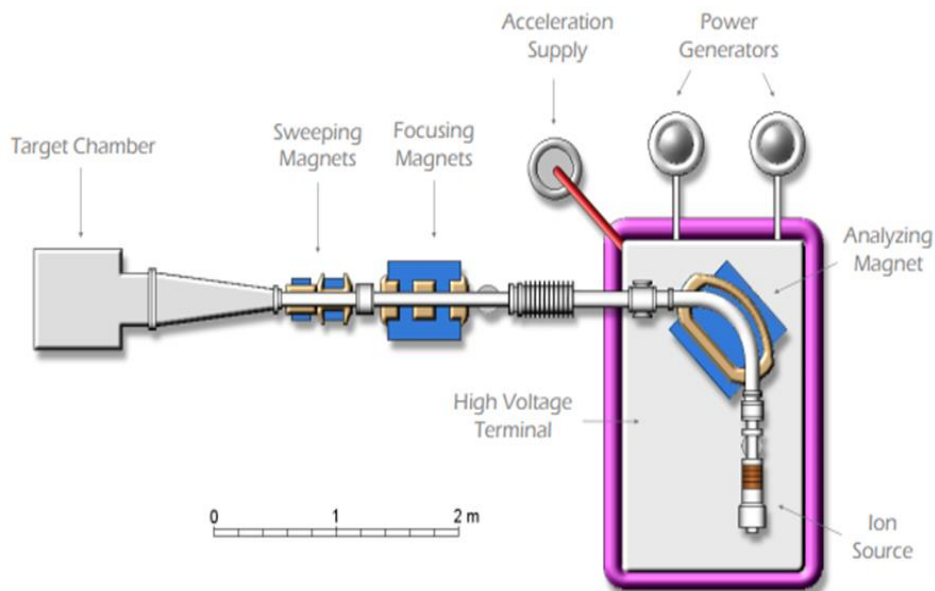


Figure 10 - Danfysik 1090 schematics. This High Current Ion Implanter model (HCII) is equipped with a CHORDIS 920 ion source. Courtesy of Jorge Rocha, LATR, CTN.

Figure 10 presents the schematics of the High Current Ion Implanter manufactured by Danfysik [78] and installed at LATR, CTN [79] in 1992. It presents the following main features:

- Model: Danfysik 1090;
- Ion source: CHORDIS 920 Sputter and Oven Versions;
- Maximum energy for singly ionized beams: 210 keV (obtained following a maximum acceleration voltage of 160 kV for post-acceleration after 50 kV for extraction);
- Beam current: up to 10 mA;
- Target temperature: -150 °C to 600 °C;
- Implantation area: up to 40×40 cm²;
- Magnetic beam focusing and sweeping.

A plasma is generated inside the ion source, powered by the power generators. A gas is created inside the ion source and then, via thermionic emission, four heated filaments at +100 A will then emit increasingly accelerated electrons to collide with the gas. The pressure inside the source never exceeds 10⁻³-10⁻⁴ Pa. A 30 kV extraction voltage (usual value, as it can go up to 50 kV) is generated and the ions are accelerated towards the double-focusing 90° analyzing magnet (with a mass resolution of 250), which is responsible for controlling the isotope purity and preliminarily focusing of the beam. Then, the accelerator supply will generate a 160 kV voltage, which will make the beam reach the three Focusing Magnets and, before entering the Target Chamber, the Sweeping Magnets which are responsible for the scanning process throughout the whole area of implantation (1600 cm² maximum). The samples enter the target chamber, which has a rotational 2-axis target to be possible to implant at 7°. The highest-pressure level reached during the whole process in the target chamber is 10⁻⁴ Pa.

3.2 Rutherford Backscattering Spectrometry/Channeling (RBS/C)

3.2.1 Basic principles

To study the concentration of defects in both a-plane and c-plane GaN samples and determine the implantation defect profile with depth, the RBS/C technique plays an important role [16].

This technique is based on Geiger and Marsden's experiment in 1909, who observed the backscattering of alpha particles when these collided with the nuclei of gold atoms – the very same reason why Rutherford would suggest a new atomic model two years later. Combining with ion channeling, it allows us to determine the implantation defect profile (with 10-30 nm depth resolution). RBS is used to study superficial layers of solid materials. When a monoenergetic He⁺ ions beam enters a solid, part of these ions is backscattered already at the surface. Most of these ions penetrate the material and lose energy by electronic excitation, due to a large amount of the collisions with the electrons of the sample.

This is a non-destructive technique, meaning that the ejection of atoms during the process is residual. The sample composition is obtained following the analysis of the particles scattered by more than 90° (with respect to the incidence direction). The ratio of incidence and backscattering (at the sample surface) energies is called *kinematic factor*, k , and is given by the following expression, where E_0 stands for the incident ion kinetic energy and E_1 represents its energy after being backscattered (being M_1 the mass of the projectile and M_2 the target ion mass).

$$k = \frac{E_1}{E_0} = \left[\frac{\cos\theta + \sqrt{\left(\frac{M_2}{M_1}\right)^2 - \sin^2\theta}}{1 + \frac{M_2}{M_1}} \right]^2. \quad (3)$$

Equation 3 [17] can be derived by considering the collision between the He^+ ions and the target as elastic. Starting with the conservation of energy formula,

$$E_0 = E_1 + E_2 \Leftrightarrow \frac{1}{2}M_1v_0^2 = \frac{1}{2}M_1v_1^2 + \frac{1}{2}M_2v_2^2, \quad (4)$$

and by considering the conservation of the momentum, both parallel and perpendicular to the direction of the incident He^+ ion,

$$\begin{cases} M_1v_0 = M_1v_1\cos\theta + M_2v_2\cos\beta \\ 0 = M_1v_1\sin\theta - M_2v_2\sin\beta \end{cases} \quad (5)$$

$$(6)$$

The angles from Equations 5 and 6 are defined in Figure 11. By relating Equations 4, 5 and 6 – where v_0 and v_1 are, respectively, the velocities of the incident ion before and after being backscattered –, v_2 being the velocity of the target atom after the collision, θ the backscattering angle and β is the angle between the directions of the incoming beam and the recoiled target atom, and defining the kinematic factor as the quotient between the incident and backscattering energies, one gets Equation (3). These quantities are illustrated in Figure 11.

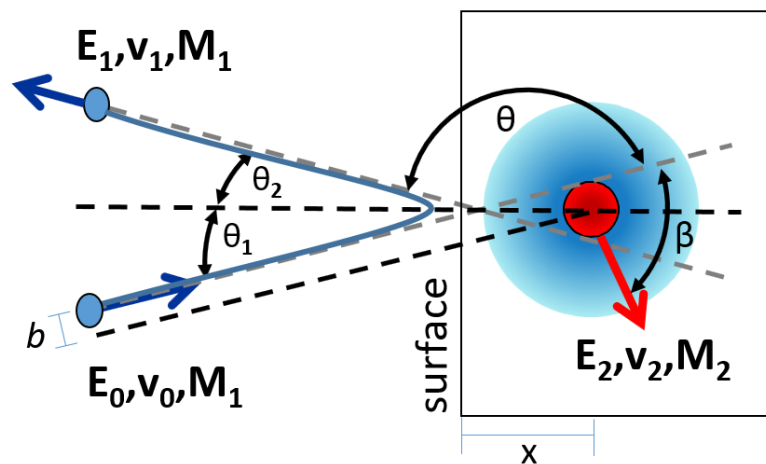


Figure 11 – Schematic of an elastic collision of an ion with a nucleus at the surface. The impact parameter (b) represents the deviation between the central axis of the nucleus and the trajectory of He^+ ; the smaller it gets, the bigger the backscattering angle is.

It is common to perform backscattering analysis using 1-3 MeV ${}^4\text{He}$ ions for some reasons: the availability of accelerators to produce beams with these energies, the bigger knowledge on the energy loss of ${}^4\text{He}$ in comparison with other ions and the fact that the backscattering cross-section $\sigma(\theta)$ for the incidence of ${}^4\text{He}$ on elements more massive than Be can be given by Rutherford's expression for centre of mass coordinates [17]:

$$\frac{d\sigma(\theta)}{d\Omega} = \left(\frac{Z_1 Z_2 \alpha \hbar c}{4E} \right)^2 \frac{1}{\sin^4(\theta/2)}, \quad (7)$$

where Z_1 is the atomic number of the incident ion (and E its energy), Z_2 is the one of the target ion and θ is the backscattering angle. α stands for the fine structure constant ($\approx 1/137$, dimensionless) and Ω is the backscattering solid angle (from the detector).

Figure 12 shows the variation of the kinematic factor of N, Ar, and Ga as a function of the backscattering angle, following Equation 3.

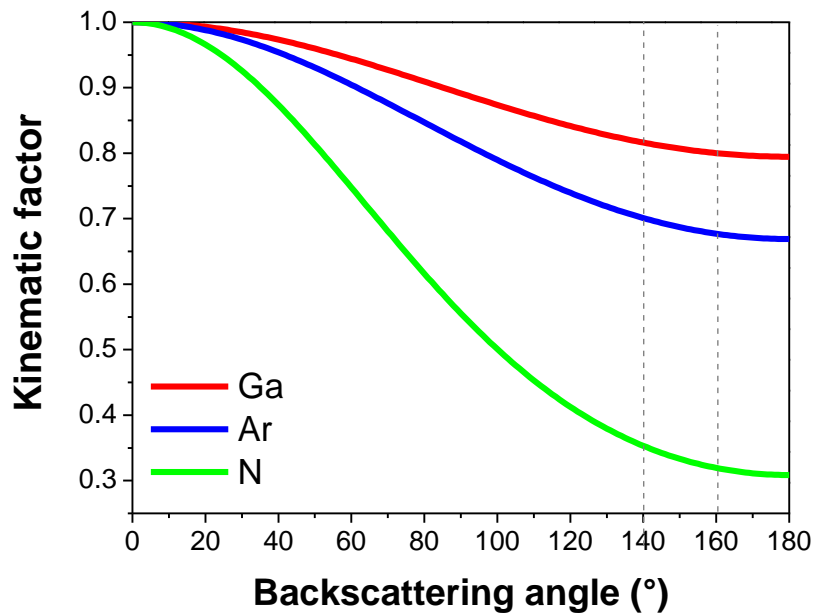


Figure 12 – The kinematic factor of N, Ar, and Ga, for a collision with a He^+ ion, as a function of the backscattering angle.

It is clear that the higher the backscattering angle, the bigger the differences between the kinematic factors of the analyzed elements. As we intend to distinguish with the maximum accuracy possible to the location of the different elements in our RBS/C spectra, this is the reason why our three detectors are located at -140° , -165° and 165° , with respect to the incident beam.

Finally, the RBS/C technique allows the possibility to have a depth resolution. Figure 13 presents Helium electronic and nuclear stopping powers in GaN.

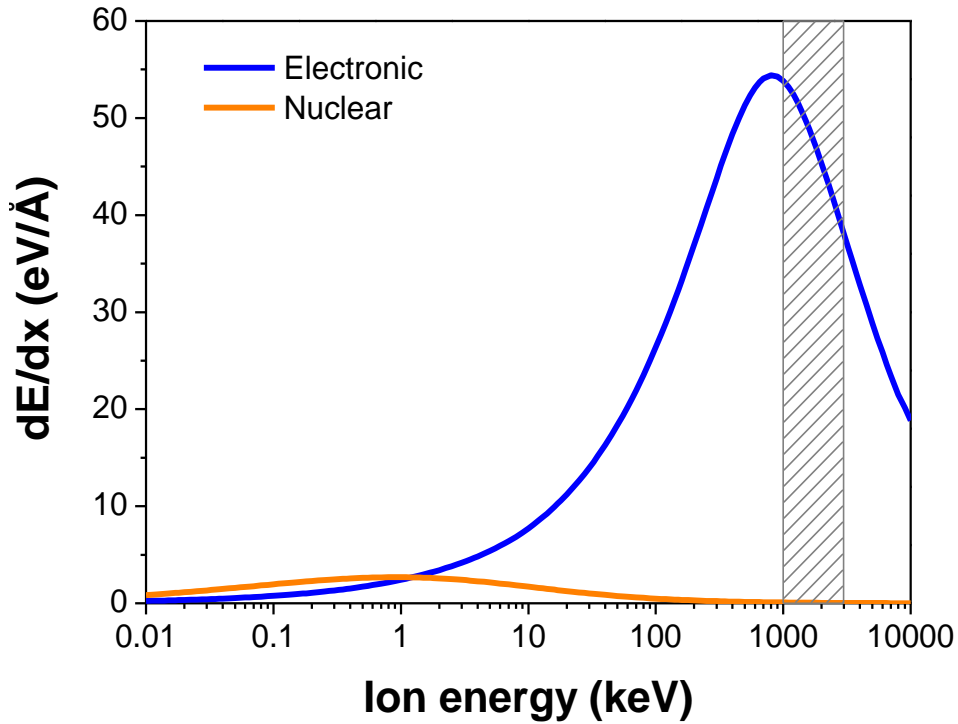


Figure 13 - SRIM calculation of the stopping power of helium in GaN. The grey dashed line represents the values of incident energy for which RBS/C is typically performed.

The range of an energetic ion inside a solid can be determined by the rate of energy loss due to excitations and ionization (stopping power), dE/dx , along with its path [10]:

$$R \equiv \int_{E_0}^0 \frac{1}{dE/dx} dE, \quad (8)$$

where dE/dx is, theoretically, the sum of both nuclear and electronic energy-loss rates and E_0 is the incident energy of the ion. However, as we can see in Figure 13, our typical values of E_0 when performing an RBS/C analysis present insignificant values for the nuclear stopping power and therefore we can consider only the electronic one. The decrease of the latter for He ions with energies above 1 MeV is the reason why elemental peak widths are thinner for higher incident energies than this threshold in a backscattering spectrum [17].

It is possible to define another quantity, the stopping cross-section ϵ , a measure of the energy loss of the ion when crossing a certain material. The relation between these two quantities is given by Equation 9, where N stands for the atomic density (usually given in atoms per cubic centimeter) [17]:

$$\frac{dE}{dx} = N\epsilon. \quad (9)$$

Values of energy-loss rates and ion stopping cross-sections are available in several books [17], [80] or can be calculated with SRIM [77].

The possibility of having a depth resolution performing backscattering is only possible by relating the scattered particle energy to the depth where it occurred. This is possible by defining a

quantity, ΔE , which represents the difference of the energy of two particles, one scattered at the surface and another at a given depth x :

$$\Delta E = [S]x, \quad (10)$$

because we are not interested in the total distance traveled by the ion, R , but its projection normal to the surface (x). The quantity $[S]$ is the energy loss factor, defined as [17]:

$$[S] = N\varepsilon = \left(\frac{k}{\cos(\theta_1)} \frac{dE}{dx} \Big|_{in} + \frac{1}{\cos(\theta_2)} \frac{dE}{dx} \Big|_{out} \right), \quad (11)$$

where the stopping powers stand for the ones for the He ion on its inward and outward paths [17]. For scattering at a given depth, the loss of energy phenomenon has to be considered. As a conclusion, it is possible to find out the depth at which the collision happened if we experimentally determine the energy difference.

3.2.2 Ion channeling

RBS is the most used ion beam technique, being one of its major advantages the possibility of combining it with channeling and allowing the study of defects as well as the lattice site location of dopants inside crystalline structures [81]. If the incident beam is aligned with a major crystal direction of the single crystal, it is guided through small angle interactions and via the electrical potential (Coulomb) created by the atoms' nuclei which align to create the channels. This channeling is crucially dependent on the incident angle, which must be smaller than some critical angle (ψ on Figure 14).

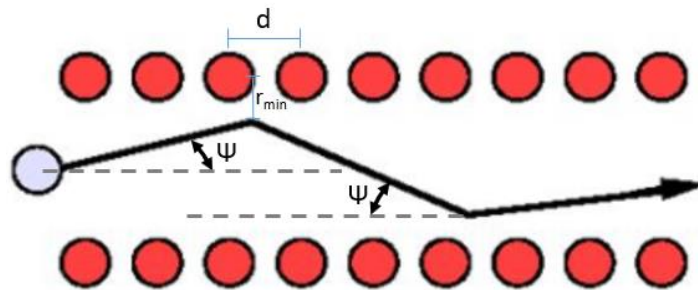


Figure 14 - Trajectory of the channeling of a particle.

We can define the minimum yield for a hypothetical perfect crystal as [82]:

$$\chi_{min} = \frac{\pi r_{min}^2}{nd}, \quad (12)$$

where the numerator indicates the impact area around the atomic line and the denominator are calculated by multiplying the atomic density n by the distance between the atoms d , giving the fraction corresponding to the superficial area of the atomic line – if a particle hits one of these lines, it will be backscattered.

Channeling effects will result in large changes in the backscattering yield, given the fact that the orientation of the target changes according to the incident beam – as the beam no longer sees the crystal as a random ensemble of atoms. The role of guided component of the beam is to detect atoms (either nitrogen, argon or gallium ones) that were displaced from substitutional lattice locations by more than 0.1-0.2 Å [16].

When this effect is taken into account to the measurements, the yield in the aligned spectrum increases due to channeled ions backscattered after hitting displaced atoms and due to the dechanneling of other ions (that could not remain being channeled due to an eventual high amount of defects) from all the atoms inside the crystal. It is often assumed that the displaced atoms are randomly located, which is very useful when analyzing crystals containing amorphous sections. While this approach may not always be valid, and among other assumptions that do not always hold – such as considering the radiation damage irrelevant for the lattice location of either impurity or host atoms – , channeling is nevertheless a powerful technique in order to provide a quick and simple analysis of the crystalline quality of a material.

3.2.3 Experimental equipment

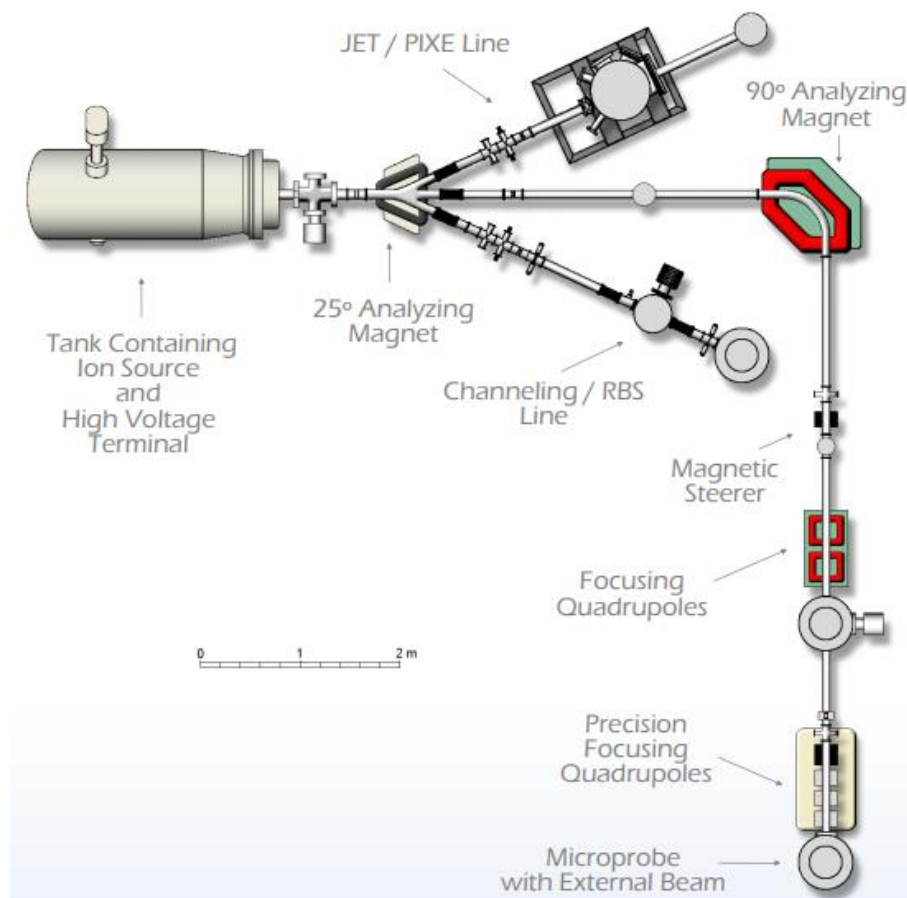


Figure 15 - Van de Graaff accelerator schematics. Courtesy of Jorge Rocha, LATR, CTN.

The Van de Graaff accelerator presented in Figure 15 together with the currently installed beamlines is an NA-2500 type-A model, fabricated by *High Voltage Engineering Europe*. It presents the following main features:

- Model: High Voltage Engineering NA-2500;
- Ion source: RF SO-173, 125 MHz 140 W Oscillator;
- Max. terminal voltage: 2500 kV;
- Beam current: superior to 100 μA H^+ and He^+ ;
- Tank insulating gas: 50% SF_6 + 50% N_2 ;
- Operation: manual with automation option.

The accelerator is located inside the tank, which contains an equal proportion of nitrogen and sulfur hexafluoride to keep the interior pressure constant and avoid electric discharges with the terminal. The pressure inside the lines must register values around 10^{-6} mbar, in order to suppress as much as air particles as possible – this avoids the collision and dispersion of the He^+ ions with them and increases the lifetime of the operational duration of the beam.

The High Voltage Terminal creates a potential that will be used to accelerate the He^+ ions, produced by the ion source. This RF (Radio Frequency) SO-173 model is a short bottle with a 600 hours lifetime (under operating conditions) and a fertile source for plenty of gaseous ions. It contains a gas, which is ionized by an RF oscillator coupled to the bottle.

Then, the confined plasma is positioned by a permanent magnetic field (located symmetrically around the bottle), which produces an axial magnetic field. By controlling the source gas pressure and the oscillator loading, one can optimize the source output. The generated beam can follow one of the three lines presented in Figure 15: JET/PIXE, RBS/C (the one used for this project) and Microprobe.

The RBS/C chamber has to be kept at pressure values of 10^{-5} - 10^{-6} mbar, which is made possible by the usage of a turbomolecular pump. The chamber has two photodiode detectors, installed in 2011 [83] and located at $\pm 165^\circ$ with respect to the incident beam, and another one, at 140° which was the one used for our spectral analysis. Before entering the chamber, the beam goes through two different collimators which aim to focus the beam and limit its dispersion at a maximum of 0.1%.

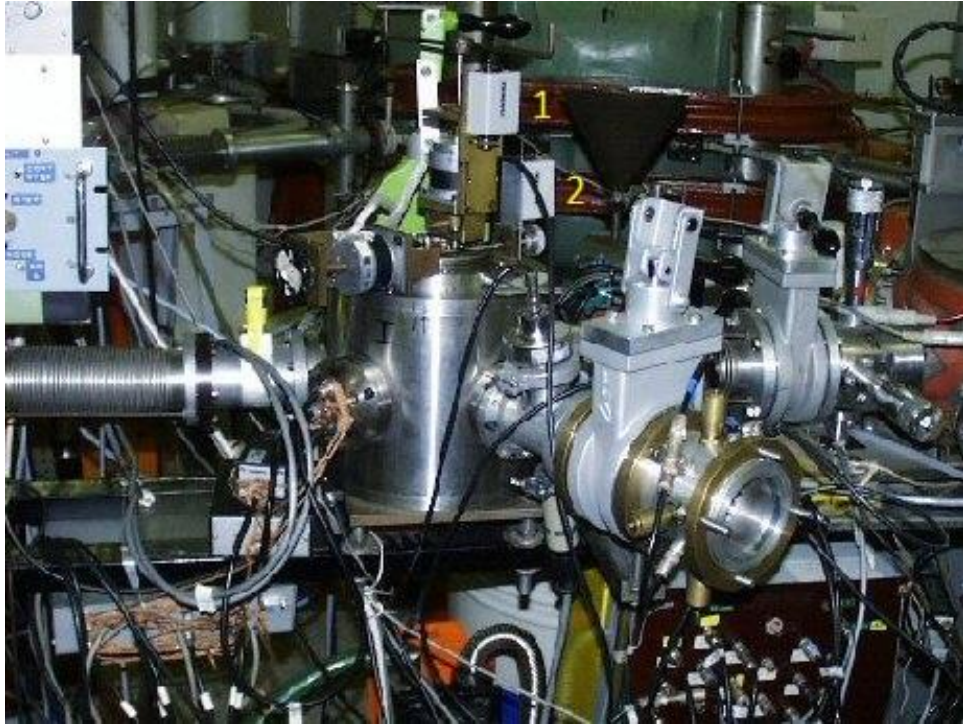


Figure 16 – RBS experimental chamber at CTN. Counters 1 and 2 are controlled by computer and linked to the data acquisition system.

Figure 16 shows the RBS chamber at CTN, where the numbers stand for the counters. The goniometer used allows steps as small as 0.04° for Φ (counter 1) and 0.02° for θ (counter 2). Among other functions, a software called GonioMotors, developed by Doctor Rui Silva, is used to control the motion of the motors, which includes a) the movement of these to the desired angular coordinates, b) the “reset” of the positions so that the analysed sample can be changed and c) the accumulation of a spectrum by continuously rotating Φ for the whole accumulation period and avoid any kind of channeling (the random spectra) [84].

3.2.4 Data analysis

- **Calibration**

As the experimental spectra give the backscattering counts as a function of channels, the correspondence between channels and energy has been achieved via the utilization of a calibration sample made, in our case, of erbium, germanium, silicon, and oxygen – showing very well defined steps in the spectrum marking the signal corresponding to the sample surface for every element, as we can see in Figure 17.

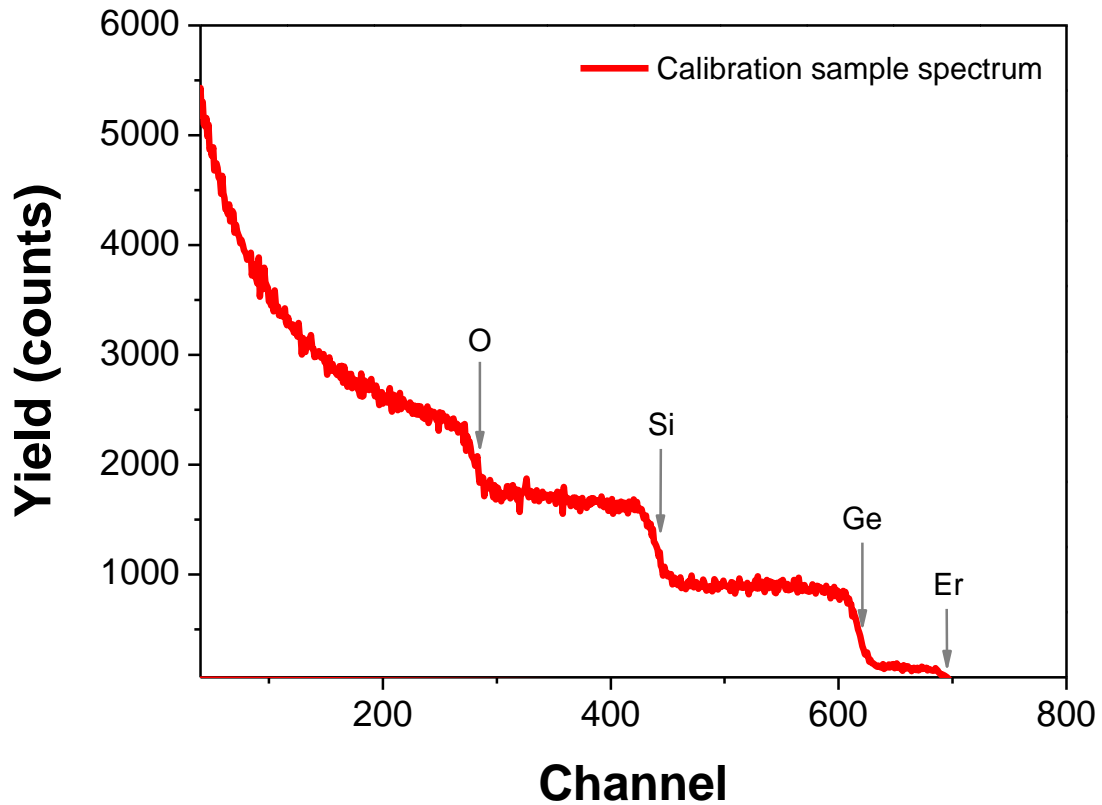


Figure 17 - Calibration sample (ErGeSiO) RBS spectrum. The arrows indicate the position of the surface channels for each element.

Given the fact that the kinematic factor only depends on the scattering/detector angle and the masses of the elements (Equation 3), one can then determine which values of energy should correspond to the four channel positions presented on the figure, thus defining a calibration curve.

Element	Atomic mass (u)	Kinematic factor	Energy (MeV)	Channel
Er	167.26	0.92	1.84	690
Ge	72.64	0.82	1.65	619
Si	28.09	0.60	1.20	440
O	15.99	0.40	0.81	279
He	4.00			

Table 2 - Kinematic factor values for erbium, germanium, silicon, and oxygen. This calculation allows us to determine the relationship between energy and channels.

The calibration curve is shown in Figure 18, where the four calibration points from Table 2 were fitted with a linear curve using the software Origin, version 7.5. The uncertainties are of 0.026 keV/channel for m and 14 keV for b , which results in around 14 keV for channel 0 and 23 keV for channel 700. The value of uncertainty of the energy of the beam is around 1 keV.

$$E \text{ (keV)} = 2.492 \left(\frac{\text{keV}}{\text{channel}} \right) \times \text{channel} + 111 \text{ (keV)}. \quad (13)$$

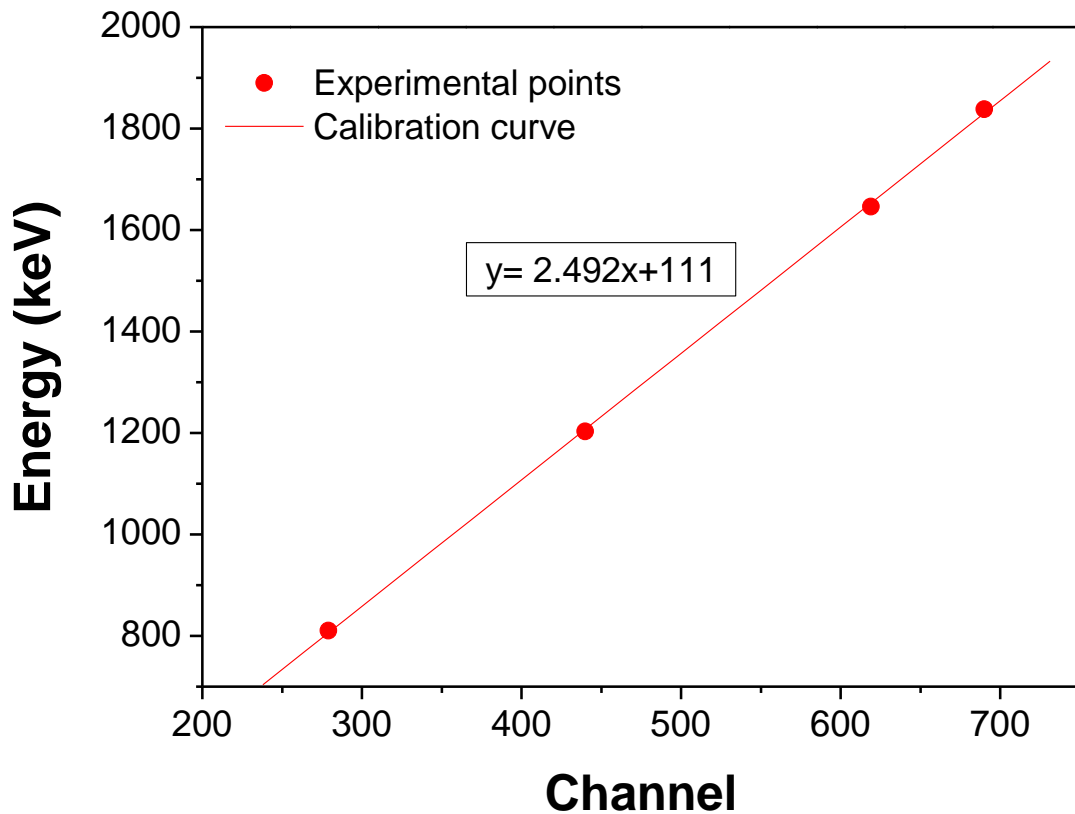


Figure 18 - Linear fit of the four experimental points gives the calibration curve.

- **Spectra acquisition**

To perform our analysis, the energy of the He⁺ ion beam is of 2000 keV and the detector angle is of 140°. RBS was performed under the same conditions for both a-GaN and c-GaN samples, being the incident angle for the random spectrum of 5°. For the acquisition of the random spectra, and in order to achieve a non-channeling situation, the samples were also rotated around their normal for ten steps of 5° each while the acquisition process was being performed.

The aligned spectra were obtained with an incident angle of approximately 0°, a value for which the backscattering was observed to be the smallest. As we first optimize the channeling of the beam through the crystalline structure, the higher the value of the backscattering yield – the more ions the beam finds that will make it be backscattered and detected -, the more damaged the implanted sample.

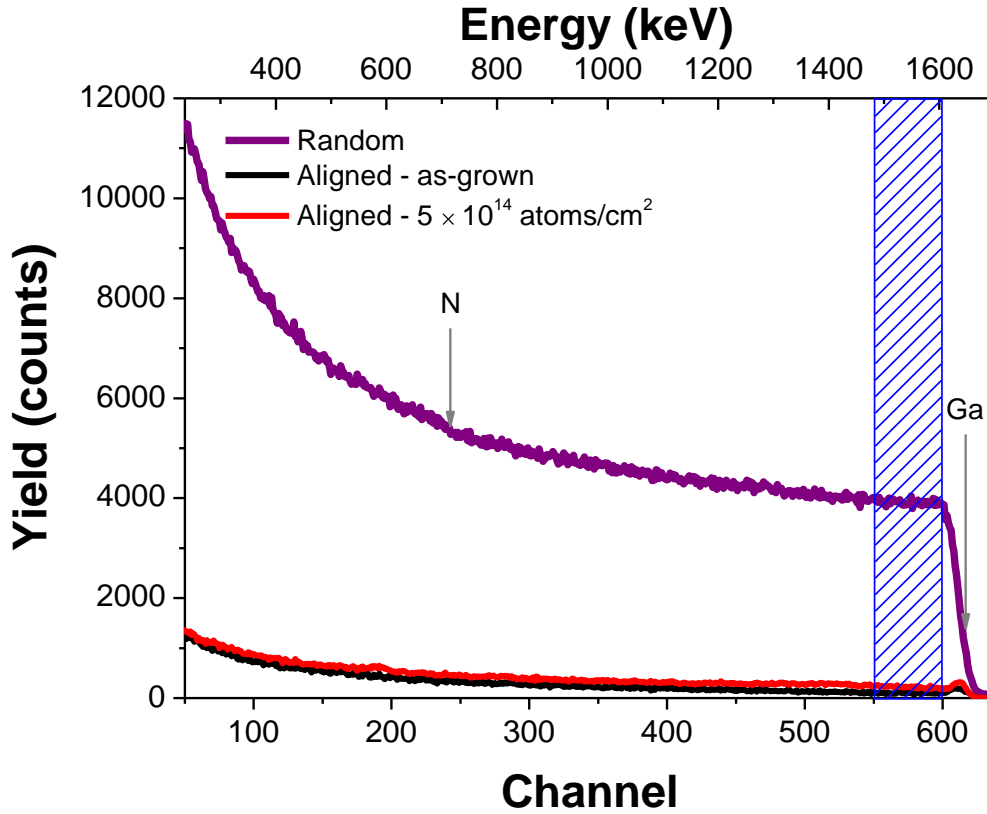


Figure 19 - RBS spectra for an implanted and non-implanted c-GaN samples, where the aligned spectra follow the direction (0001). These spectra were shifted and normalized by using MSpectra, a Matlab code developed by Doctor Sérgio Magalhães. A minimum yield of 2.6% for as-grown sample and 5.6% for the implanted one was calculated.

In Figure 19, three spectra are shown: one random one (following an arbitrary direction) and two aligned (channeled) ones, one for the as-grown sample and another for an implanted sample. The arrows indicate the position of the signal for both nitrogen and gallium barriers corresponding to the surface of the sample, which can be calculated by multiplying the incident energy of 2 MeV by the kinematic factor for each element, presented in Equation 3.

The minimum yield is an important parameter when characterizing the defects' profile of a material; the better the channeling effect, the fewer ions will be backscattered (a crystal follows a repetitive and well-defined order), which means the fewer counts will be detected in the aligned spectrum. Equation 12 is the formula only for a perfect, ideal crystal, however, every real crystal has defects.

Therefore, χ_{min} for a real crystal can be measured by RBS/C and its value is determined by Equation 14, where A stands for the area of the RBS/C spectrum for a given measurement in a defined region/window of interest. Typical values for nitrides range between 1% and 5% (the smaller the yield, the better the crystal quality), calculated by defining a window in our RBS spectra to calculate the areas:

$$\chi_{min} = \frac{A_{aligned}}{A_{random}}. \quad (14)$$

- **DECO**

As mentioned previously, the ion channeling technique is very useful to characterize the defect profile inside a crystalline structure. After measuring the random and aligned spectra of both implanted and as-grown samples, the difference in minimum yield for each channel (whose relation to depth has been shown previously) can be calculated. It is then necessary to quantify the dechanneling effect of the beam on defects. Dechanneling happens when the concentration of defects inside the sample is too high for the beam to keep on being channeled inside the lattice. This results in, for example, an ion changing direction (thus losing the channeling effect) not due to direct backscattering but because the angle with respect to the atomic rows can suddenly become higher than the critical channeling angle.

So as to extract the damage profile from the RBS/C spectra, it is essential to determine the variation of the minimum yield (from Equation 14) as a function of the depth. In Equation 15, Y stands for the yield, in every channel, from each spectrum (implanted or as-grown, aligned or random):

$$\Delta\chi_{min} = \frac{Y_{align}^{impl} - Y_{align}^{as-grown}}{Y_{random}}. \quad (15)$$

The relative damage level (RDL), which correlates the relative concentration of displaced lattice atoms versus depth, was then determined by using the DECO code, which implements a two-beam model [85]–[87] in order to account for the dechanneling background. One of the beams on this model interacts with all the target atoms randomly, and the other one “follows” the channeling and so it can only interact with eventually displaced lattice atoms. DECO calculates the transition rates of particles from the aligned to the random beam by taking into account randomly displaced atoms.

3.3 X-Ray Diffraction (XRD)

Given the fact that it is sensitive to small variations of the lattice parameters, the XRD technique is a very efficient technique to measure the strain caused by implantation defects inside the crystalline structure. An overview of its basic principles, experimental equipment and simulation software used at LATR, CTN is presented. For a complete description of the X-Ray Diffraction technique, P. F. Fewster’s book from 2003 is a very good option [18], while the review from Moram and Vickers presents its main applications in studying nitrides [19].

3.3.1 Discovery of the x-rays

The discovery of the x-rays is usually attributed to Wilhelm Röntgen, the first Nobel Prize in Physics winner of the XX century for the, quoting the Nobel Committee, “discovery of the remarkable rays subsequently named after him”. In the end, the original x-rays name, given to the fact that Röntgen was not able to find out if this new radiation was constituted by waves or particles, is the most used one (although “Röntgen radiation” exists in many languages as well).

It could, however, be mentioned that this discovery and subsequently the Nobel Prize could have been awarded to Nikola Tesla instead [88]. Starting in March of 1896, Tesla was the author of a series of scientific papers on x-rays in *Electrical Review*, New York. He had been independently doing research on the topic since 1894 and it is thought to have captured an x-ray image few weeks before Röntgen's statement of the discovery in late December of 1895.

The reasons why Tesla never claimed credit for being the first to identify this new radiation are not only because the discoveries were made too close in time, but also since most of his research was lost in a fire that burnt down his laboratory in New York in March of 1895. Not only Tesla continued his own experiments with x-ray imaging after hearing of Röntgen's discovery, but also both scientists mutually congratulated and respected each other's work. Figure 20 shows a letter from Edison to Tesla regarding his x-ray investigation.

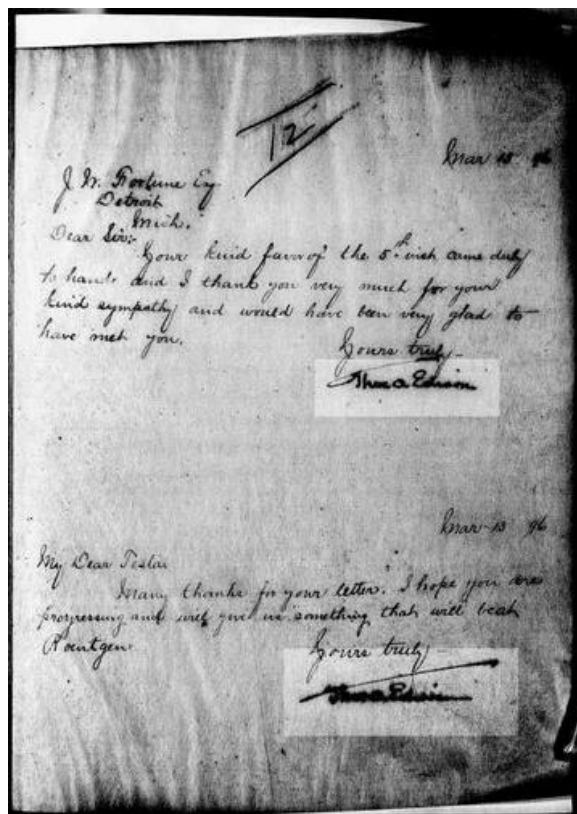


Figure 20 - Thomas Edison and Nikola Tesla correspondence from the 1890s. Edison wrote to Tesla in 1896: "My dear Tesla, Many thanks for your letter. I hope you are progressing and will give us something that will beat Röntgen".

3.3.2 Laue and Bragg's contribution

Max von Laue's 1912 proposal to study X-Ray Diffraction in crystalline solids gave him the next Nobel Prize in Physics related to this radiation, two years later. Laue irradiated a small monocrystalline material with x-rays and concluded about their (wave) nature, which had not been possible to demonstrate previously with the available technology. The biggest importance of this discovery is that it showed the wide range of applications of x-rays in the study of crystals.

1915's Nobel Prize in Physics was also attributed to x-ray-related research, this time to the father (William Henry) and son (William Laurence) Bragg. The outcome of their work was not only an X-ray crystalline diffraction theory [89] but also the first x-ray spectroscopy.

If each atomic plane behaves like a reflecting surface, Bragg realized that, although the scattering process is very complex, the reflection of x-rays can be mathematically treated like any other reflection – in the sense that the reflected angle is equal to the incident angle. As we can see from Figure 21, wave 1 and wave 2 have different paths inside the material. It is this phase difference that is responsible either for a constructive or destructive interference which depends, by looking at the figure, on the wavelength of the x-rays λ , on the incident angle θ and on the distance between atomic plans, d .

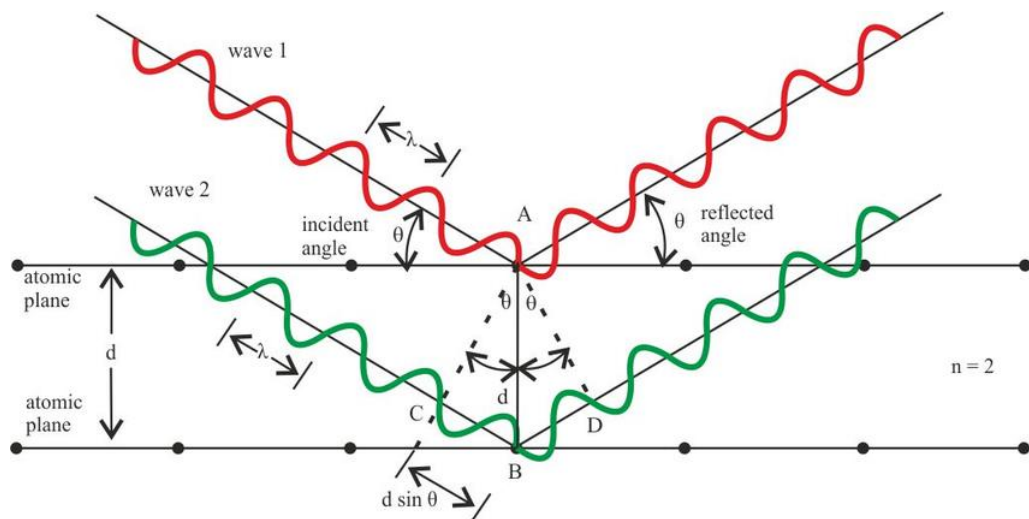


Figure 21 - Electromagnetic waves being scattered in crystallographic planes (schematic). Adapted from [90].

If the extra distance that wave 2 travels is equal to a multiple of the wavelength, we, therefore, have a constructive interference (points A and D on Figure 21 are in phase).

Bragg's Law (or condition) comes as:

$$n\lambda = 2d\sin(\theta), \quad (16)$$

where d stands for the distance between atomic planes, θ is the incident angle and λ is the wavelength of the x-rays. The position of the diffracted beam is described by the angle 2θ with respect to the incident beam. It is possible to define the distance d as a function of Miller indices h, k, l , becoming d_{hkl} .

3.3.3 Experimental equipment



Figure 22 - Photo of Bruker D8 Discover diffractometer.

Figure 22 presents the Bruker D8 Discover High-Resolution X-Ray diffractometer, installed at LATR, CTN. It presents the following main features:

- Model: Bruker D8 Discover;
- Configurations: horizontal or vertical goniometer, $\theta/2\theta$ or θ/θ geometry;
- Measuring circle diameter: between 500 and 1080 mm (depending on setup);
- Angular range: 360° (without accessories);
- Maximum usable angular range: $-110^\circ < 2\theta < 168^\circ$ (depending on accessories);
- Angle positioning: stepper motors with optical encoders;
- Smallest addressable increment: 0.0001° ;
- Maximum angle speed: $20^\circ/\text{s}$
- Maximum power consumption: 6.5 kVA (without controllers for optional equipment).

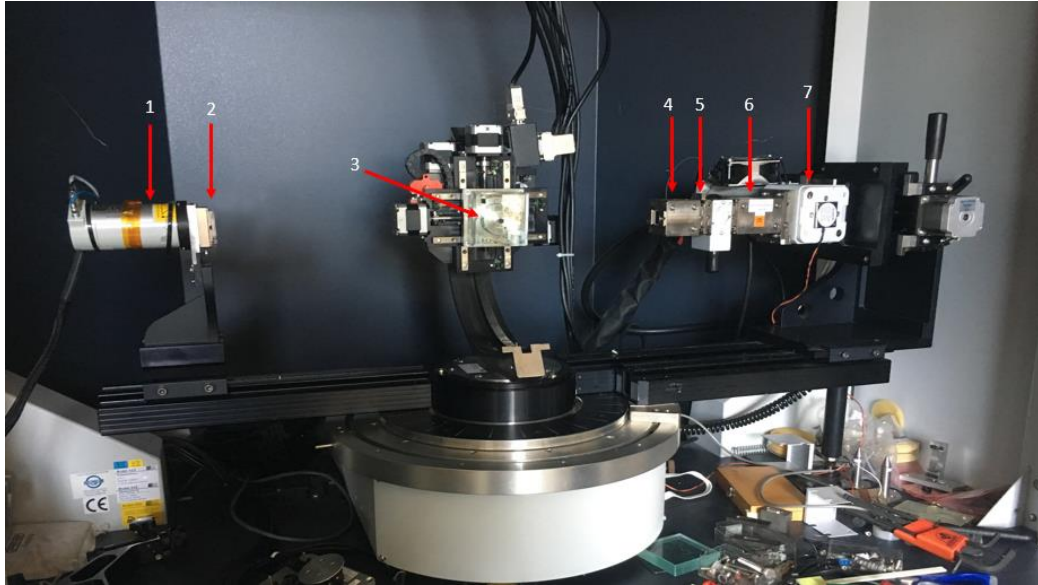


Figure 23 - Bruker D8 Discover photograph of the main components used for this work. 1 – scintillation detector, 2 – place of the 0.1 mm width slit, 3 – 6-axes goniometer, 4 – two-crystal Germanium (220) monochromator to control the vertical divergence of the beam and select only the $K_{\alpha 1}$ emission line, 5 – 0.2 mm width slit, 6 – Göbel mirror, for the focusing process of the beam and to make it parallel, and 7 – X-Ray Cu source.

Figure 23 presents a photograph of the main components of the diffractometer. The 6-axes goniometer presents three angular axes (ϕ , ω , χ , used for the scanning process) and three linear axes (x , y , z , to control and put in position the sample holder) The 2θ axis is represented by the movement of the detector.

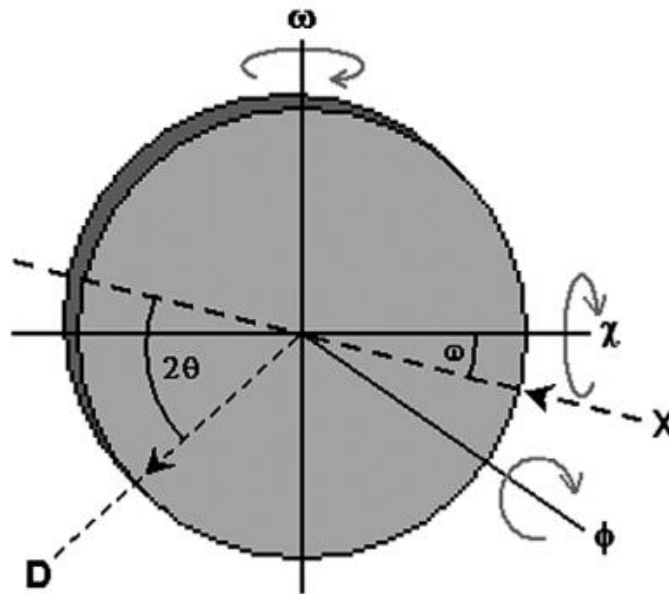


Figure 24 - Sample reference frame, illustrating the axes of rotation from the goniometer. ω refers to the incident angle, which was presented as θ in Figure 21. 2θ stands for the angle between incident and diffracted beams. D refers to the detector and X indicates the direction of the X-Rays. Adapted from [19].

Figure 24 shows the angular plus the detector axes mentioned above.

3.3.4 Scan types

According to the axes from Figure 24 and the equipment shown in Figure 23, it is possible to perform several scan types [19]:

- **Detector scan (2θ):** by keeping both the sample holder and the source in the same position for the whole duration of the scan, it is only the detector that moves. The 0.1 mm width slit is used in front of the detector only for scans that include the movement of this axis, to better define the centroid of the diffraction peak.
- **Rocking curve (ω):** the detector is now immobile and the sample spins around the ω axis, by keeping all the other axes motionless. The name comes from the fact that it implies “rocking” the sample holder about the ω -axis. It is the best choice to detect broadening caused by defects as it scans the diffraction spot following an arc, however, this broadening caused both by the experimental procedure and the crystal defects affects its application to determine lattice parameters.
- **Φ scan:** both the source and the detector stand still and the sample spins around its own normal.
- **2θ - ω scan:** both the detector and the sample spin following, respectively, the 2θ and ω axis with an angular ratio of 2:1. The 0.1 mm width slit is used. This is the required scan for lattice parameter determination, as the constant motion of both axes aims to recurrently optimize Bragg’s condition at each point, providing a better resolution.

Below, Figure 25 presents a schematic representation of one symmetric reflection.

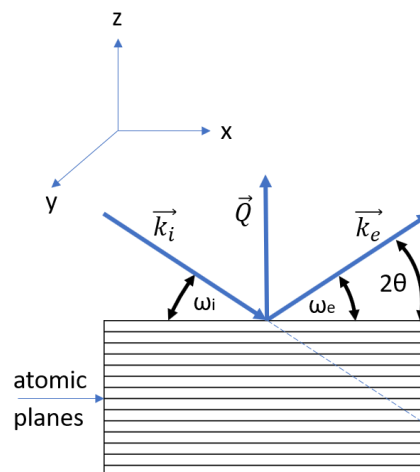


Figure 25 - Schematic representation of one symmetric reflection, where the atomic planes are parallel to the sample surface. The angles ω_i and ω_e are, respectively, the incident and the exit angles, while \vec{k}_i and \vec{k}_e are the incident wavevector and the exit wavevector. The measured planes are always perpendicular to the wave transfer vector $\vec{Q} = \vec{k}_e - \vec{k}_i$.

The XRD geometry considered for our measurements were symmetric reflections, represented by Figure 25, where we are measuring atomic planes parallel to the surface.

An example of the diffractograms of our samples are presented in Figure 26 for the symmetric reflections (0002), for c-GaN, where $\omega_i = \omega_e = \frac{2\theta}{2}$. By measuring symmetric reflections, we are sensitive to only one lattice parameter at a time, c for c-GaN and a for a-GaN; this is, therefore, a good geometry to determine the variation of this quantity.

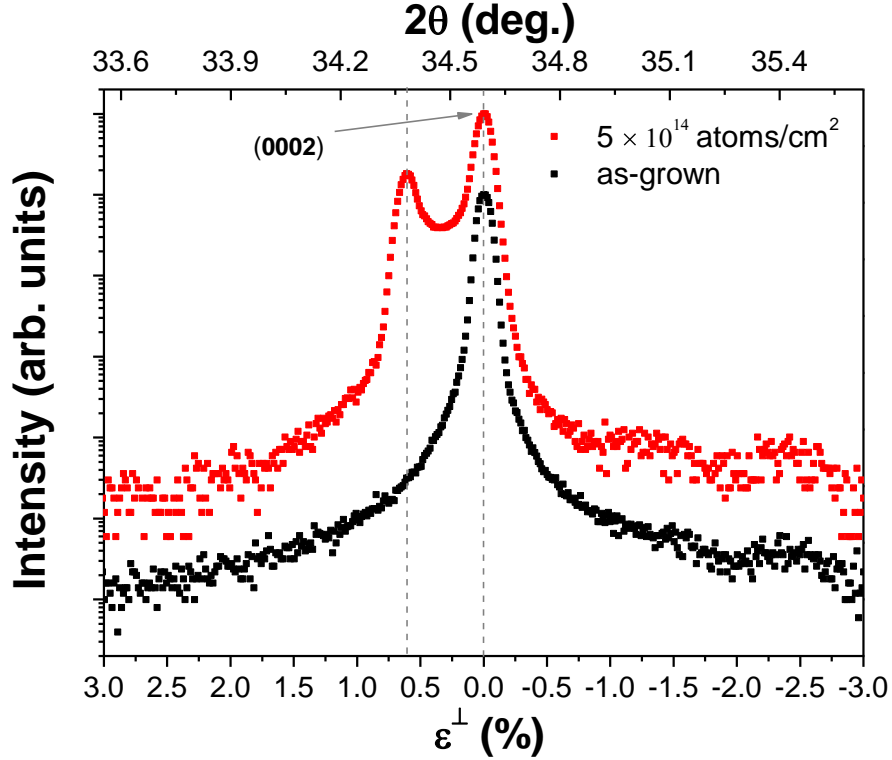


Figure 26 - XRD 2θ - ω scans around the (0002) symmetric reflection for an implanted fluence of 5×10^{14} atoms/cm² sample and as-grown sample for c-GaN. The main Bragg peak corresponds to the diffraction from the deep, unimplanted GaN volume, while the lower peak at lower angle reveals the expansion of the lattice parameter in the implanted volume. The intensity is presented in arbitrary units and as a function of both the perpendicular strain and the 2θ angle. The diffractograms were vertically translated to achieve a better visualization of their differences.

Figure 26 presents the diffractograms of two c-GaN samples, one non-implanted and one implanted. By comparing both diffractograms, it is possible to identify the expansion of the lattice parameter inside the sample due to the formation of a second, lower-intensity peak: the implanted atoms created many defects that have strained the material within its internal structure and in opposition to RBS/C, the XRD technique allows us to “see” deeper inside the sample. XRD is the best technique to measure the strain caused by implantation defects inside the crystalline structure.

The two X-axes are intrinsically connected given the relation between 2θ and the perpendicular strain to the substrate, ε^\perp , which can be defined as:

$$\varepsilon^\perp \equiv \frac{\Delta x}{x_0} = \frac{x - x_0}{x_0}, \quad (17)$$

where x_0 represents the lattice parameter of the as-grown sample (a- or c-GaN) and x stands for the expanded lattice parameter, whose expansion is determined by the 2θ angle. By recovering Equation 16 and substituting d as a function of the Miller indices h, k, l , where a, b and c are lattice parameters [19], comes:

$$\left\{ \begin{array}{l} n\lambda = 2d_{hkl}\sin\left(\frac{2\theta}{2}\right) \\ \frac{1}{d_{hkl}^2} = \left[\frac{4}{3}(h^2 + k^2 + hk) + l^2 \left(\frac{a}{c}\right)^2 \right] \frac{1}{a^2} \end{array} \right. \quad (18)$$

$$\left. \right\} \quad (19)$$

We need to calculate the strain for one lattice parameter at a time. By combining Equations 18 and 19, defining $n=1$ due to the periodicity of the $\sin(\theta)$ function, and substituting the Miller indices by the values of the used symmetric reflections – (002) for c-GaN and (110) for a-GaN –, comes:

$$\left\{ \begin{array}{l} n\lambda = 2\frac{c}{2}\sin\left(\frac{2\theta}{2}\right) \Leftrightarrow c = \frac{\lambda}{\sin(2\theta/2)} \\ n\lambda = 2\frac{a}{2}\sin\left(\frac{2\theta}{2}\right) \Leftrightarrow a = \frac{\lambda}{\sin(2\theta/2)} \end{array} \right. \quad (20)$$

$$\left. \right\} \quad (21)$$

Substituting Equations 20 and 21 in Equation 17 gives the final formula for the perpendicular strain as a function of the angle:

$$\varepsilon^\perp = \frac{\sin(2\theta_0/2) - \sin(2\theta/2)}{\sin(2\theta/2)}, \quad (22)$$

where θ_0 is represented by the grey dashed line in Figure 26 for each planar orientation. Its values are in accordance with the ones calculated following the lattice parameters reported in the previous literature on the subject [33], [37], and can be calculated by solving Equations 17 and 18 with respect to θ_0 . The wavelength of the x-ray source is $\lambda=1.54056 \text{ \AA}$ and, by setting $n=1$:

$$\left\{ \begin{array}{l} \lambda = 2\frac{c}{2}\sin\left(\frac{2\theta_{0c}}{2}\right) \Leftrightarrow 2\theta_{0c} = 2 \times \sin^{-1} \frac{1.54}{5.19} \simeq 34.57^\circ \\ \lambda = 2\frac{a}{2}\sin\left(\frac{2\theta_{0a}}{2}\right) \Leftrightarrow 2\theta_{0a} = 2 \times \sin^{-1} \frac{1.54}{3.19} \simeq 57.77^\circ \end{array} \right. \quad (23)$$

$$\left. \right\} \quad (24)$$

For the material whose 2θ angle is centered for the previously showed values ($\theta=\theta_0$), then $\varepsilon^\perp=0$, i.e., this layer is relaxed. The same calculations can be performed for the implanted volume, corresponding to the peak centered around 34.38° (Figure 26). The strain calculated using the equations above and the values of our samples is found to be about 0.6%. Although useful to define the strain of the implanted (and virgin) volume, the previous method does not provide any information regarding the evolution of strain as a function of depth. Moreover, there is no information with respect to the intensity of the diffracted beam. Simulations of the 2θ - ω scans according to the dynamical theory of x-ray diffraction provide further information on the profile of strain as a function of depth, by recursive calculations of the intensity of the diffracted beam of any strain profile [91]. According to this theory, the intensity depends on three parameters:

- Physical properties: unit cell volume, atomic scattering factors, structure factor for a specific reflection, crystal thickness, lattice parameters and the classical electron radius (geometrical);
- Experimental parameters: the polarization factor and the direction cosine of the incident and diffracted beams with respect to the sample normal;
- Instrumental properties: the shape of the incident beam (usually called “instrumental function”) and the source wavelength used.

Following Bartels *et al.* [91], the structure factor for a given reflection (F_{hkl}) can be changed in order to accommodate the lattice damage caused by ion implantation. The transformed structure factor, (F'_{hkl}), is therefore rearranged to:

$$F'_{hkl} = F_{hkl} e^{-\alpha \times \varepsilon^{\perp 2}(z)}, \quad (25)$$

in which α is a fitting parameter and $\varepsilon^{\perp}(z)$ is the strain at a certain depth, defined by the layered depth strain profile. Hereafter, $e^{-\alpha \times \varepsilon^{\perp 2}(z)}$ is defined as the static Debye-Waller (DW) factor, which has been used as a way to quantify the lattice damage after the approach used by Speriosu [92], where a value of 1 indicates a “perfect” and 0 an amorphous crystal, respectively.

3.3.5 Data simulation software

The XRD diffractograms were simulated with RaDMaX – Radiation Damage in Materials analysed with X-ray diffraction –, an open-source code developed in Limoges, France, used to determine strain and damage depth profiles in implanted crystalline materials [67].

RaDMaX is a software which was developed to study implantation induced strain and extract strain and damage profiles. It allows fitting experimental 2θ - ω XRD data, combining fitting algorithms and providing as input perpendicular strain and static DW factor. The latter parameter considers the attenuation of diffracted x-ray intensity due to the static displacements of the original atoms of the crystalline structure, caused by the creation of point defects after implantation [93]. The framework of this process follows the solution proposed by Bartels *et al.* [91] to the Takagi-Taupin equations.

RaDMaX models the strain and DW factor profiles by defining a fixed number of basic functions on its interface, which will be given as input by the user. It has, however, the disadvantage of not being mathematically possible to define two consecutive layers with the same deformation, which is a problem when trying to better define the peak attributed to the region of defects when simulating nitrides.

Regarding the fitting algorithms, there is the option to choose between a general one (GSA – Generalized Simulated Annealing, a slow convergence method based on the Tsallis statistics [94]), when one is yet to have an idea on the wanted profiles, and a conventional least-squares algorithm,

based on the Levenberg-Marquardt [95], [96] algorithm and to be used when there are only some minor adjustments left for the strain and DW profiles to deliver a satisfactory output – which has the disadvantage of being ineffective when one is yet to have a certain level of certainty regarding the solution to the fitting.

RaDMaX was, initially, compared to MROX – Multiple Reflection Optimization package for X-ray diffraction –, a code developed by Doctor Sérgio Magalhães which, in opposition to RaDMaX, allows not only defining two consecutive layers with the same deformation and different thicknesses to different layers but also simulating the effect of residual $K_{\alpha 2}$ radiation in our diffractograms and the presence of layers of other materials in the film [62], [63]. Experimental fittings from both codes are presented in Figure 27.

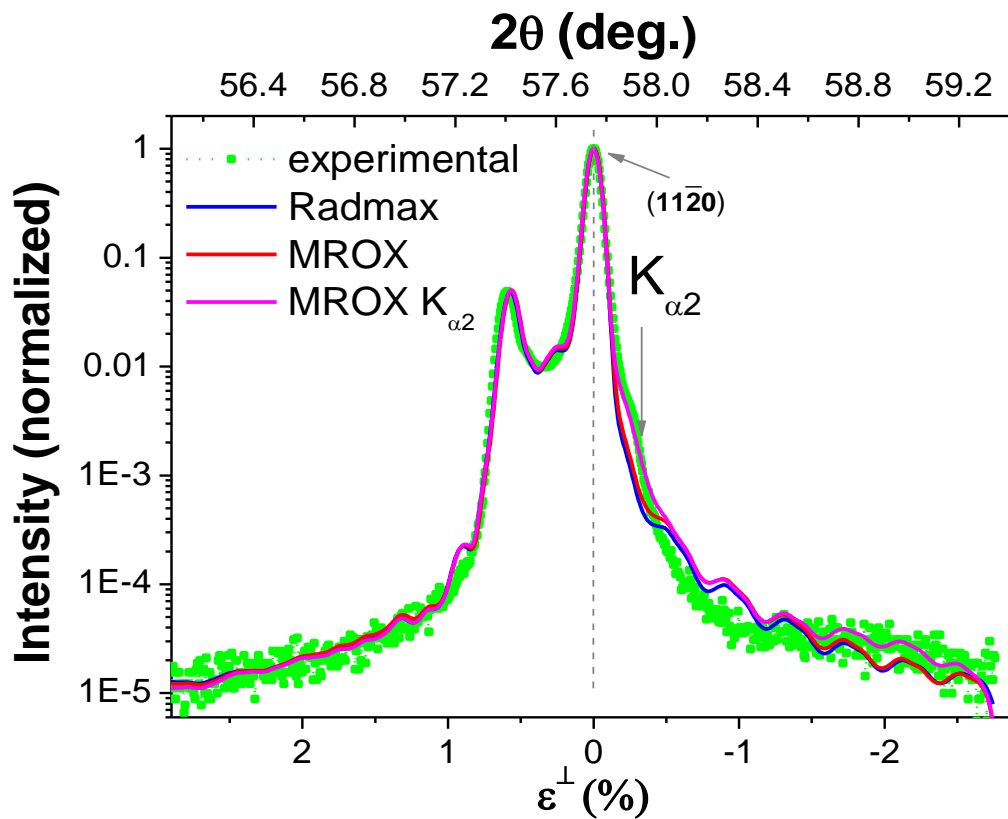


Figure 27 - Comparison of a RaDMaX fit with two MROX fits, one of them including the effect of the $K_{\alpha 2}$ line. While the fitting for the same conditions for both codes is roughly the same, MROX gives a better solution when considering the $K_{\alpha 2}$ effect. The implanted fluence is of 5×10^{13} atoms/cm² for a-plane GaN.

Figure 27 presents a comparison between RaDMaX and MROX for the same implanted fluence for a-GaN, where MROX was simulated with and without taking into consideration the $K_{\alpha 2}$ line effect.

By recovering Equation 21, it is possible to calculate the theoretical location of the $K_{\alpha 2}$ line. Being $\lambda_{K_{\alpha 2}}=1.54439$ Å and $a=3.189$ Å [37], and defining $n=1$, comes:

$$\lambda = 2 \frac{a}{2} \sin(\theta) \Leftrightarrow \theta = \sin^{-1} \frac{1.54439}{3.18900} \simeq 28.97^\circ, \quad (26)$$

which gives a 2θ value of approximately 57.94° , agreeing both with the MROX fit and the experimental data.

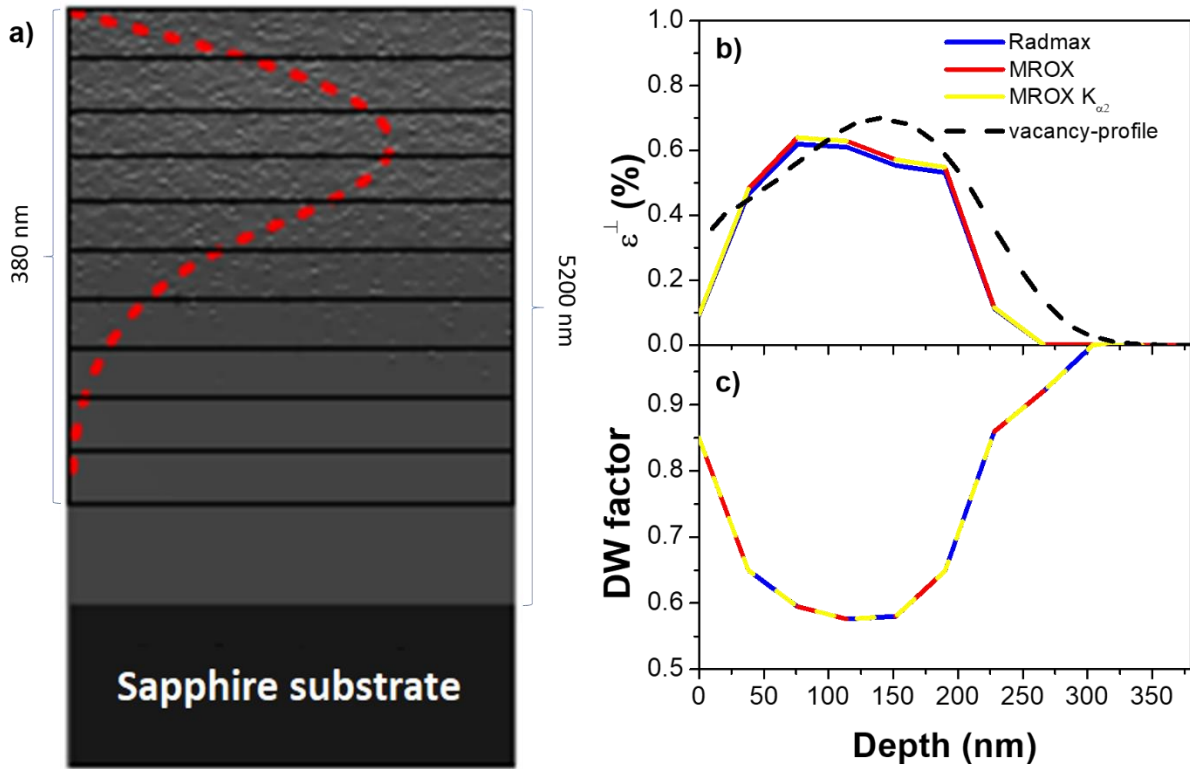


Figure 28 – a) schematic of the simulation of the damage inside the sample fitted in Figure 27, with its b) strain and c) DW factor profiles. Ten layers with the same thickness were defined, with a pre-defined Gaussian-like shape for strain profile (in red) and its “mirror” for DW. The damage depth is 380 nm, from SRIM. The relation between thickness values of damaged and undamaged regions and substrate in a) is not at scale.

Figure 28a presents a schematic of the definition of the layers inside the sample simulated in Figure 27, for both RaDMaX and MROX codes (to be able to compare both codes on the same conditions): ten consecutive layers with the same thickness and different strain and DW values were defined.

Figure 28b and Figure 28c present, respectively, the strain and DW factor profiles, where it is possible to see that MROX delivers roughly the very same strain and DW profiles from RaDMaX, for the same conditions, and when considering the $K_{\alpha 2}$ line effect.

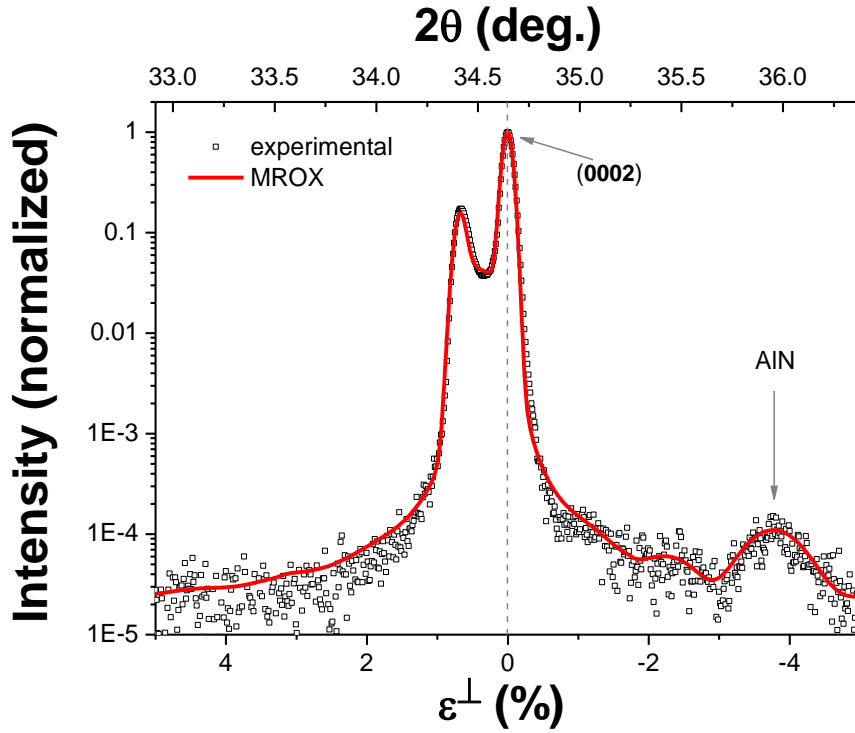


Figure 29 - Simulation of an implanted fluence of 1×10^{15} atoms/cm² for c-plane implanted GaN with MROX, which has the possibility of simulating the deep AIN layer inside the sample and indicated by the grey, dashed arrow.

As mentioned previously, MROX allows the simulation of layers of different materials inside the sample, which is the case for our samples as shown in Figure 8. A c-GaN implanted sample was, therefore, simulated taking this effect into account as shown in Figure 29. We can see the clear formation of a peak at around $2\theta=36^\circ$ corresponding to the AIN buffer layer, where the bottom x-axis strain scale should no longer be considered (as it is defined for the expansion of the c parameter of GaN).

Regarding the location of the peak due to the AIN layer, we can take Equation 20, using $\lambda_{K\alpha 1}=1.54056 \text{ \AA}$ (the main line from the X-Ray source) and AIN lattice constant $c=4.9795 \text{ \AA}$ [37]. Defining $n=1$ comes:

$$\lambda = 2 \frac{c}{2} \sin(\theta) \Leftrightarrow \theta = \sin^{-1} \frac{1.54056}{4.97950} \simeq 18.02^\circ, \quad (27)$$

which means we should expect its peak to appear in the diffractogram at $2\theta=36.04^\circ$, agreeing both with the MROX fit and the experimental data.

As a conclusion, MROX not only gives the same solution as RaDMaX for the same conditions, but its versatility allows the possibility of simulating effects that were seen to appear in our diffractograms. However, factors such as the temporal limitation for the elaboration of this work and the simplicity of the usage of RaDMaX were considered and ultimately led to the choice of this software for the presentation of the simulated results of the XRD measurements performed for this work.

Chapter 4 Results

4.1 Rutherford Backscattering/Channeling (RBS/C)

Figure 30a presents the RBS/C aligned spectra of the c-GaN samples implanted to different fluences as well as a typical random spectrum. The as-grown sample exhibits a very good crystal quality with a minimum yield of 2.6%, which corresponds to usual values measured for state-of-the-art epitaxial GaN films [97]. After implantation the backscattering yield in the aligned spectra increases, as expected due to the formation of implantation defects. This is most clear for the sample implanted to the highest fluence of 8×10^{15} atoms/cm². To evaluate better the effect of implantation with the lower fluence Figure 30b shows the aligned spectra for these samples with more detail.

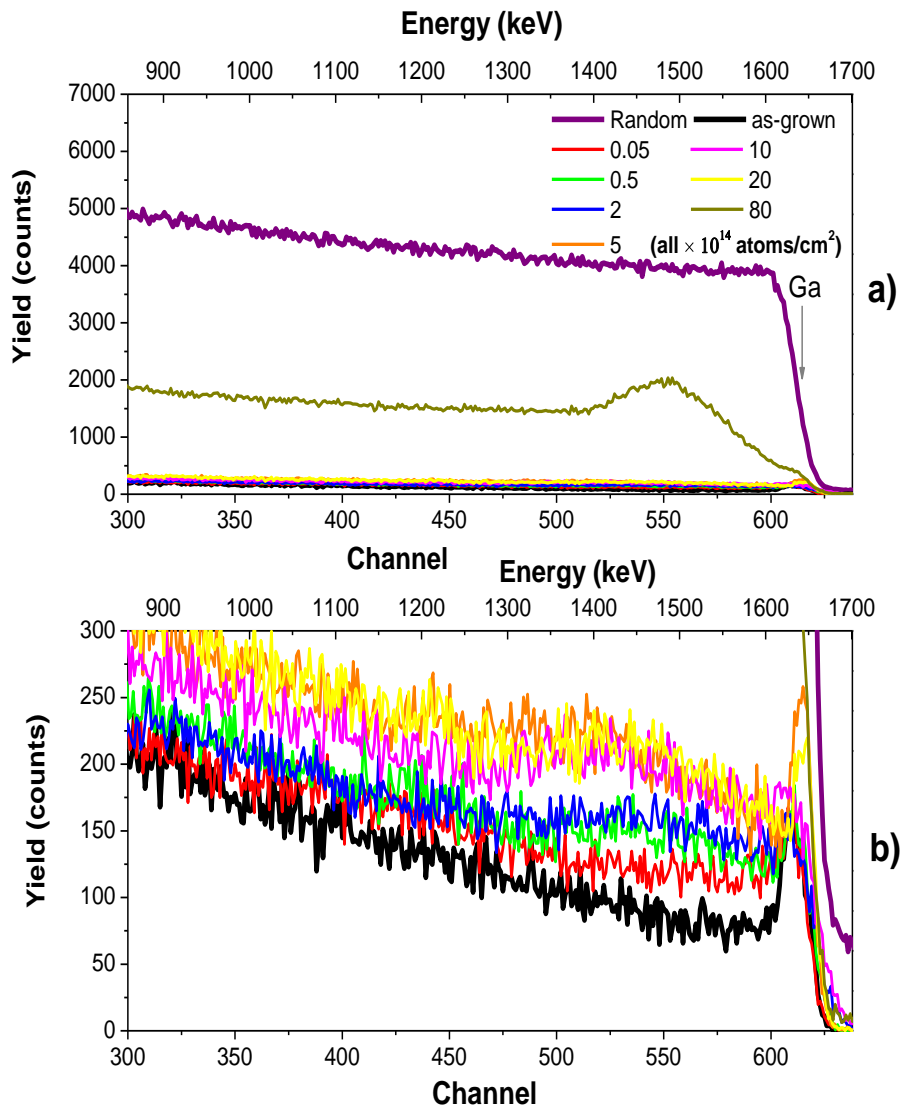


Figure 30 - c-GaN RBS/C spectra, aligned along the $\langle 0001 \rangle$ axis, for different implantation fluences, including as-grown aligned spectrum and random spectrum for the highest implanted fluence – the random spectrum here presented could have been of any of the other samples as it does not depend on the fluence values.

Although for the lowest fluences the RBS/C technique is reaching its sensitivity limit, in the scale presented in b) an increase of the yield as the fluence increases is clearly observed. However, the increase of the backscattering yield is not linear with the fluence. For example for the three highest fluences shown in Figure 30b a saturation of the damage level is seen.

Results for a-GaN are shown in Figure 31, where the as-grown sample also presents a very good crystal quality with a minimum yield of 2%. It is possible to detect some differences between the two crystalline orientations and identify three different stages, which were not as clear for c-plane orientation: the first one corresponds to fluences below 5×10^{14} atoms/cm² where the backscattering yield increases with increasing fluence.

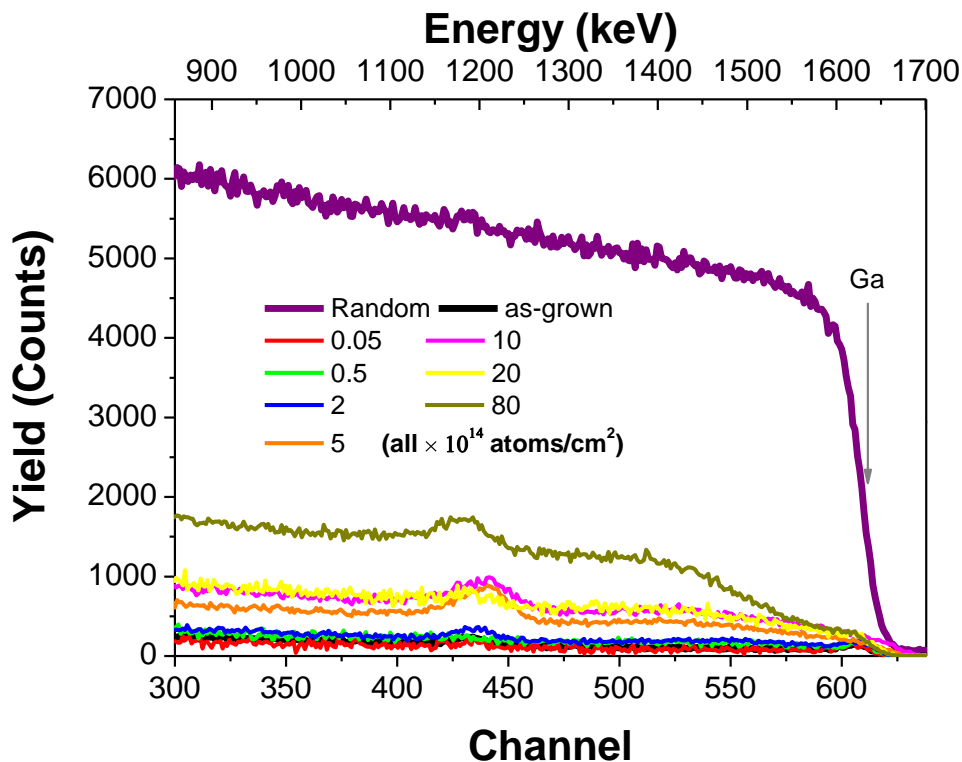


Figure 31 - a-GaN RBS spectra, aligned along the $\langle 11\bar{2}0 \rangle$ axis, for different implantation fluences, including as-grown aligned spectrum and random spectrum for the highest implanted fluence – the random spectrum here presented could have been of any of the other samples as it does not depend on the fluence values. It is possible to identify a peak occurring between the channels 420 and 450, which was attributed to an instrumental malfunction due to temporal limitations that prevented a further analysis to take place.

The next stage concerns the fluences between 5×10^{14} and 2×10^{15} atoms/cm², in this fluence range the backscattering yield remains constant indicating a saturation of damage level, in this case even more distinguishable from the first three fluences than for c-GaN. The third and final stage concerns the highest implanted fluence where a strong increase of backscattering yield is observed for both materials. In general, it is possible to detect that both planar orientations show a bimodal damage distribution with a pronounced surface peak due to the interaction of the ion beam with the surface (the more damaged the surface, the higher the peak) and a broader one spreading through deeper regions in the crystal as the channeling ions are backscattered due to interaction with defects [17], [23]. The surface peak for GaN may also indicate the formation of a nanocrystalline surface layer due to defect migration towards the surface, observed by several authors [13], [23].

The aligned RBS/C spectra present a high backscattering yield even for unimplanted regions (below channel ~460), which are due to the dechanneling of the He⁺ beam in the preceding region and suggest the existence of extended defects – following the transformation of already existing point defects [30].

4.1.1 Calculation of Relative Defect Level

To extract and quantify the defect profiles, the relative defect level (RDL) as a function of depth was extracted as described in Chapter 3, which allows a more quantitative analysis of the results. Figure 32 presents three different stages of damage accumulation and their profiles, where the RDL corresponds to the fraction of displaced atoms.

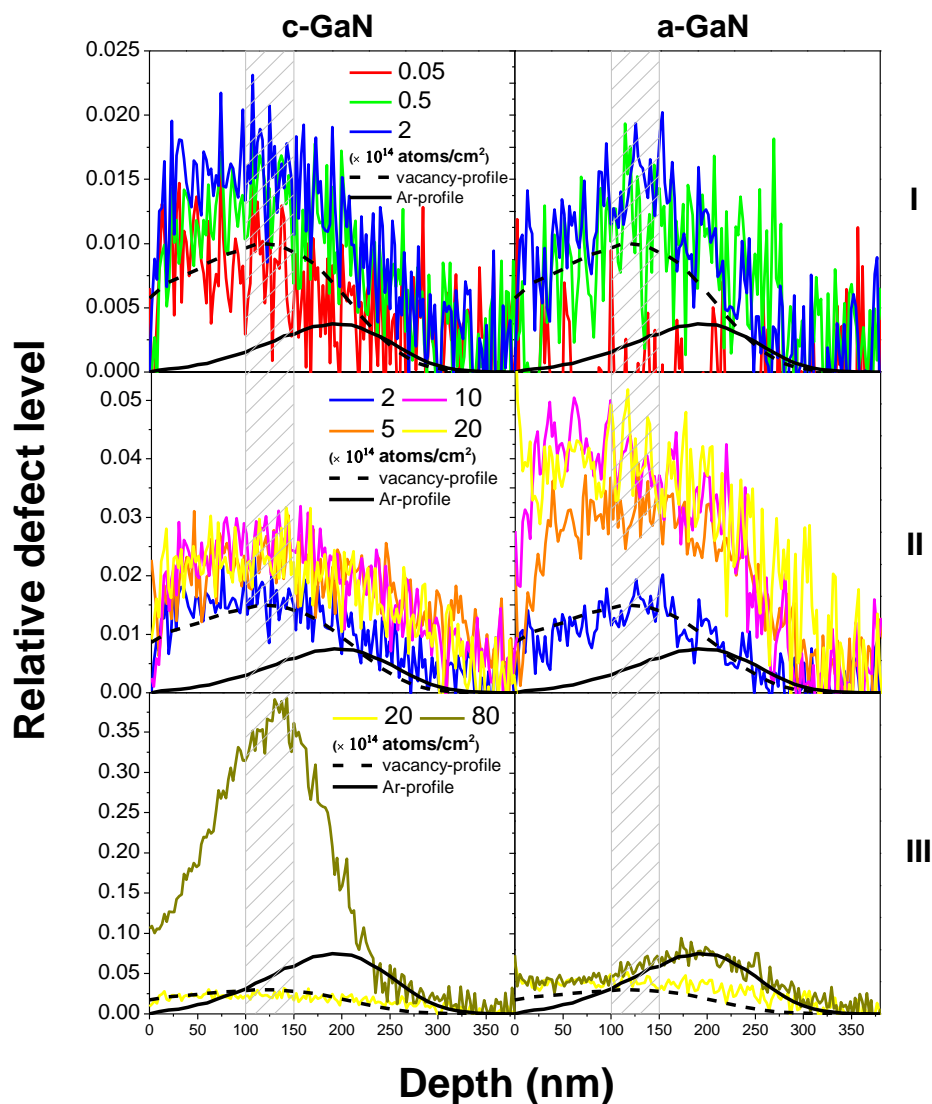


Figure 32 - Relative defect level profiles derived from the RBS/C spectra using a two-beam model for both planar orientations. Numbers on the right side of each row indicate the three different damage build-up stages. The distributions of argon and vacancies simulated using the code SRIM are included for comparison, with arbitrary units. The area between 100 and 150 nm is highlighted as it corresponds to the depth window used to plot the damage build-up (Figure 33).

The first row shows an increase of the defect level with fluence; its shape corresponds well to SRIM simulations for vacancy profiles, for both planar orientations. It is then possible to identify a saturation of the defect level for both planar orientations on the second row, regime II (although at a slightly higher RDL is observed for a-GaN). On the third row, the shape of the profile clearly deviates from SRIM simulations for both materials, an occurrence which has been reported previously [98], [99]. For c-GaN, the damage in the region of 0-100 nm is much lower than expected, assuming that we are expecting a profile with the shape of the dashed, black SRIM profile – suggesting a recombination of defects, as reported previously [14], [29], proposed to occur at higher temperatures by Wendler *et al.* For a-GaN, the depth of maximum damage changes considerably and it is found at the depth of maximum Ar-concentration.

For fluences below 8×10^{15} at/cm², none presents an RDL higher than 0.035 for the c-plane orientation, while it occurs for a-plane oriented samples (even if not very significantly). It is difficult to identify substantial differences between planar orientations for the fluences of the first stage, and both present almost the same relative defect level for all the three second stage fluences – even if for a-GaN their values are slightly higher than the ones for c-GaN.

Figure 33 represents the average RDL in a depth window from 100 nm to 150 nm (indicated in Figure 32 as the highlighted gray area) as a function of the fluence. This region corresponds to the value where the SRIM vacancy-profile reaches its maximum. The error bar is the uncertainty associated with the calculation of the difference in the minimum yield (for the 100-150 nm window), $\Delta\chi_{\min}$, between the implanted and as-grown sample, by recovering Equation 15.

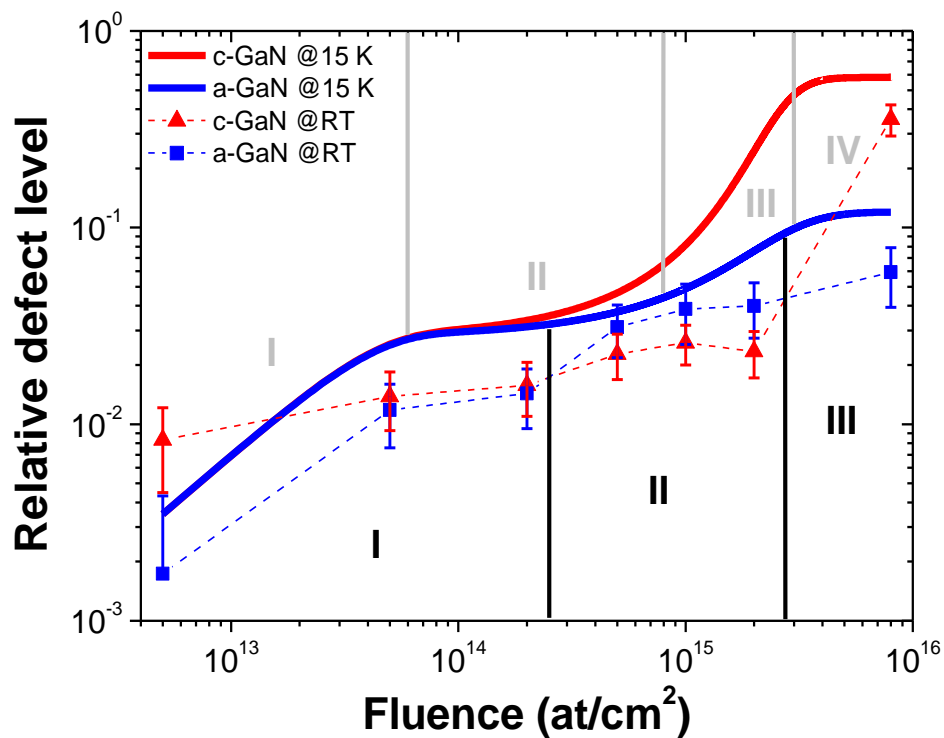


Figure 33 - Damage build-up curves. Simulated curves using Hecking's model at 15 K [30], [71] are shown for comparison with measured points (symbols and dashed lines) for both a-GaN and c-GaN.

By considering the error in the yield, ΔY , to be of 10% – mainly due to the uncertainty in measuring the total charge used for each spectrum, which was estimated as the average difference between the random spectra extracted for each sample (while the statistic error is much lower in this case) –, the error propagation for this case comes as:

$$\Delta\Delta\chi_{min} = \sqrt{\left(\frac{\partial\Delta\chi_{min}}{\partial Y_{align}^{impl}} \Delta Y_{align}^{impl}\right)^2 + \left(\frac{\partial\Delta\chi_{min}}{\partial Y_{align}^{as-grown}} \Delta Y_{align}^{as-grown}\right)^2 + \left(\frac{\partial\Delta\chi_{min}}{\partial Y_{random}} \Delta Y_{random}\right)^2} = \sqrt{\left(\frac{\Delta Y_{align}^{impl}}{Y_{random}}\right)^2 + \left(-\frac{\Delta Y_{align}^{as-grown}}{Y_{random}}\right)^2 + \left(-\frac{\Delta Y_{align}^{impl} - \Delta Y_{align}^{as-grown}}{Y_{random}^2} \Delta Y_{random}\right)^2} \quad (28)$$

This calculation delivered an uncertainty bigger than 100% for the sample implanted to a fluence of 5×10^{12} atoms/cm² for a-GaN, which is the reason why the error bar is represented only for the positive direction (as negative values cannot be represented in a logarithmic scale).

Figure 33 also shows the damage accumulation curve obtained in [30] by fitting the experimental data using the Hecking model of implantation damage build-up [71]. The Hecking model presents five stages for the damage accumulation process, as described in Chapter 2; however, the Hecking model data shown in Figure 33 corresponds to implantation and measurements done at 15 K [30] and was included only for comparison. Therefore, while our fluence range corresponds to four stages at 15 K and taking into consideration the associated error, our measured points seem to correspond to only the first three regimes, as it has been shown for c-GaN by Pagowska *et al.* [11]: for low fluences (from 5×10^{12} to 2×10^{14} at/cm²), the RDL slowly increases with the fluence (first regime). On the second regime (from 5×10^{14} to 2×10^{15} at/cm²), the RDL saturates, while the third regime (for the 8×10^{15} at/cm² fluence) indicates a steep increase of the RDL for c-GaN and a much smaller variation for a-GaN. The higher radiation resistance for this regime for a-GaN has been reported previously both for Ar-implantation (at 15 K) [30] and for Eu-implantation (at room temperature) [31].

4.2 High-Resolution X-Ray Diffraction (XRD)

To study the induced strain in both planar orientations, XRD analysis was performed for all implanted fluences, measuring 2θ - ω scans of symmetric reflections. In terms of Miller-Bravais indexes (*hki*) the symmetric reflection measured for c-GaN is the 0002 and for a-GaN is the $11\bar{2}0$. Figure 34 presents the 2θ - ω scans for both crystal orientations.

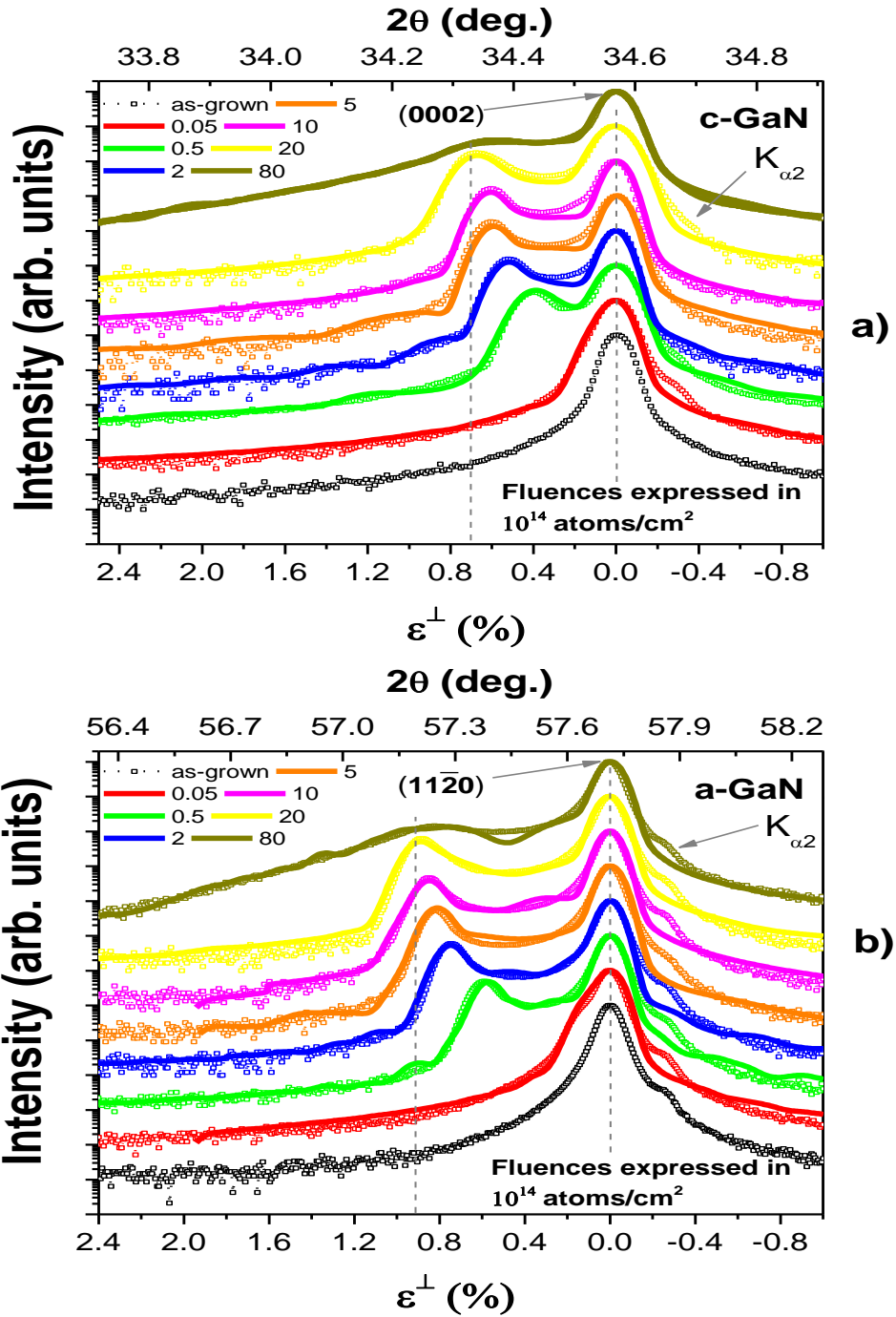


Figure 34 - XRD diffractograms (symbols) around the (0002) reflection for c-GaN (a) and the (11 $\bar{2}$ 0) reflection for a-GaN (b), implanted to different fluences. For the lower x-axis, the 2θ angle was converted to perpendicular strain. The low-intensity peaks at the high angle side of the main peak (more evident for a-GaN) are attributed to instrumental artifacts due to an incomplete filtering of the $K_{\alpha 2}$ Cu X-Ray line by the monochromator. Fluences are expressed in 10^{14} atoms/cm 2 . Lines indicate RaDMaX fits and as it is easier to distinguish lines from dots, the legend is given in function of the lines. The diffractograms were vertically translated to achieve a better visualization of their differences.

Figure 34 shows that, after implantation, a peak attributed to the implanted volume is formed for lower 2θ angles (higher c and a lattice parameters for c-GaN and a-GaN, respectively) with respect to the main Bragg peak. For both planar orientations, from fluences of 5×10^{13} at/cm 2 up to 2×10^{15} at/cm 2 , the implanted volume peaks are well-defined and suggest that homogeneously strained layers are formed. By increasing the fluence, it is possible to identify an increased perpendicular lattice

strain, given by a shift on the implanted volume peak to lower 2θ angles. For the highest fluence (8×10^{15} at/cm²), the position of its implanted volume peak does not change compared to the previous fluence (at around $\varepsilon^{\perp} = 0.65\%$ and $\varepsilon^{\perp} = 0.9\%$ for c-GaN and a-GaN, respectively) and the implanted volume peak broadens strongly. The bad definition of the peak for this fluence is given to the fact that the sample is already strongly damaged. The same pattern was already observed for c-GaN implanted with Ar at 200 keV where strain saturation occurs for higher fluences [61]. In fact, at these high fluences, the XRD technique becomes insensitive to further defect formation which is why the fluences in the present thesis were restricted to the low fluence regimes.

Figure 35a shows the relative strain values, for the location of the damage peak on the diffractograms for each fluence from 5×10^{13} at/cm² to 2×10^{15} at/cm², while Figure 35b presents the intensity ratio between the damage peak and the virgin/as-grown peak, for the same range of fluences. Figure 35b aims to show no more than a direct relation between both intensities (thus not considering the background effect and only the value of intensity for both peaks).

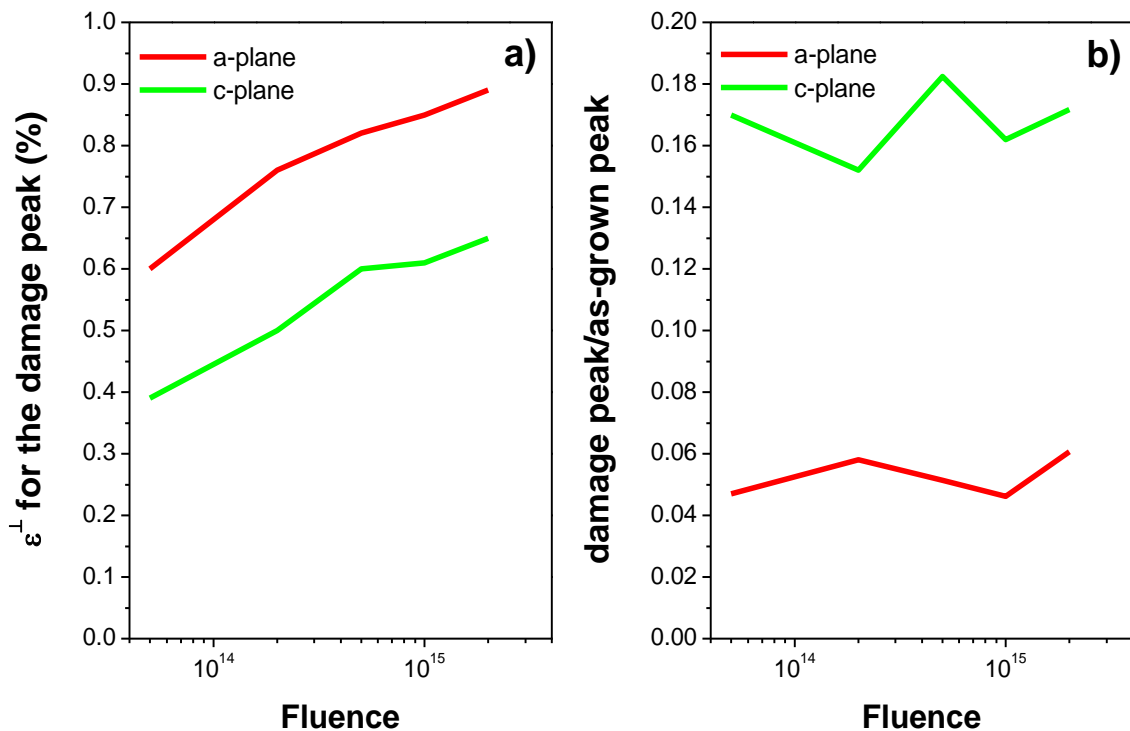


Figure 35 - Comparison between both planar orientations. a) indicates the value of strain for the damage peak per fluence, while b) indicates the relative "height" of the peak, calculated as the quotient between the intensity of the peak attributed to the implanted volume and the one of the main Bragg peak. Fluences range from 5×10^{13} at/cm² to 2×10^{15} at/cm².

It is possible to conclude that not only the value of strain for the damage peak is higher for a-GaN than for c-GaN, but also its relative "height" is lower. The lower intensity ones come from the fact that the total thickness of a-GaN samples is almost twice as much one of c-GaN samples. Therefore, if the damage thickness would be approximately the same for both planar orientations, then the relative intensity of the implanted volume peak with respect to the main Bragg peak will have to be lower for a-GaN (the bigger the damage depth, the higher the peak attributed to the implanted volume). These relations are not possible to obtain for the lowest fluence, as there are not enough implanted atoms to

create a visible damage peak on the diffractogram, while for 8×10^{15} at/cm² it is due to the high level of crystalline damage which decreases the diffraction intensity from the implanted layer (Figure 34).

4.2.1 RaDMaX simulations

- Main fits

The diffractograms were then simulated with RaDMaX software to accomplish a better understanding of the strain and the crystalline quality of the material (given by the static Debye-Waller, DW, factor). These fittings were obtained by adjusting the strain and DW factor input values. Implantation defects are known to induce strain, leading to the dilatation of the lattice parameters of c-GaN [12], [23], [28], [100]. Figure 36 presents the strain profiles taken from RaDMaX simulations (fits to the experimental data are showed in Figure 34).

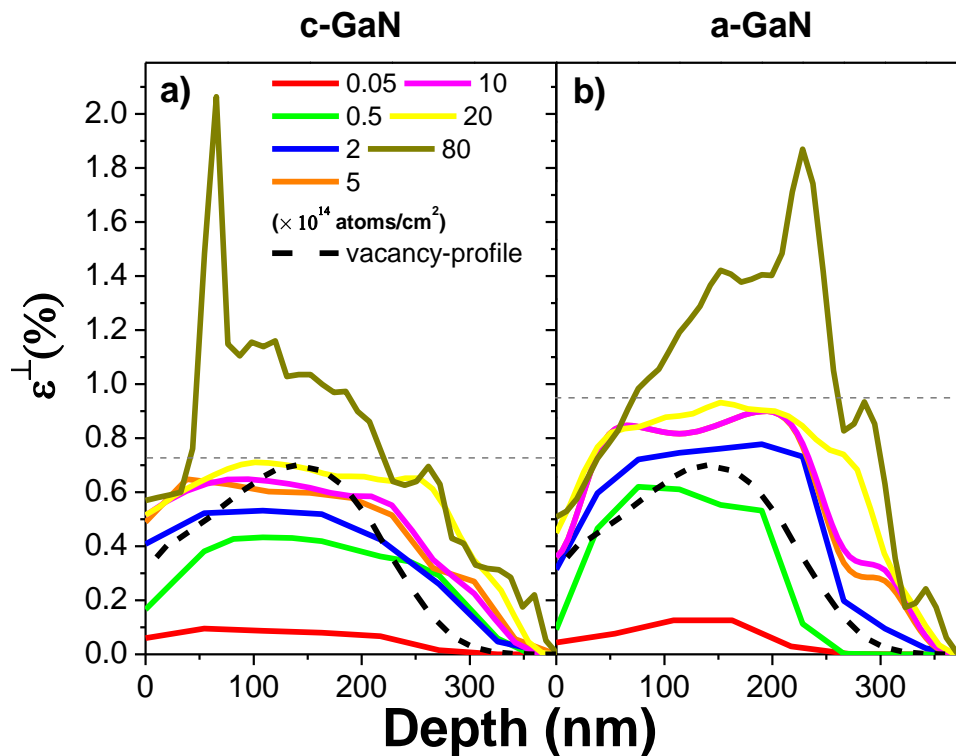


Figure 36 - Strain profiles derived using the RaDMaX code for a) c-GaN and b) a-GaN as a function of depth. The range of 380 nm for the depth axis corresponds to the maximum argon atom range obtained from SRIM simulations. The SRIM vacancy-profile is included for comparison with arbitrary units.

It is clear for both planar orientations that the strain increases with the fluence; in fact, putting aside the highest fluence profile (8×10^{15} at/cm²), the maximum strain value reached for both planar orientations, illustrated by the grey, horizontal, dashed line ($\sim 0.7\%$ for c-GaN and $\sim 0.95\%$ for a-GaN) is very similar to the strain value for the implanted volume peak of the second highest fluence (2×10^{15} at/cm²).

There is a wide depth region with almost constant strain, which agrees with the fact that the diffractograms show a well-defined second, lower angle peak. A good fit is achieved when using profiles similar to the SRIM vacancy-profile for low fluences (up until 1×10^{15} at/cm²), while the transition of the strain profiles from 1×10^{15} to 2×10^{15} at/cm² may indicate a development of the strain around 270 nm, for both planar orientations.

As it was possible to observe already in Figure 35a, the maximum strain is higher for every fluence up until 2×10^{15} at/cm² for a-GaN than for c-GaN. It has, however, been previously reported that direct comparison between induced strain caused by implantation defects for different planar orientations may not be trivial. Debelle *et al.* [66], [101] pointed out that a two-step model, firstly proposed by Rao *et al.* [102], needs to be taken into account when studying the induced strain following ion implantation in single crystals. This is a model that considers the elastic reaction of the substrate (the unirradiated layer) to the strain arising on the implanted layer [66], [101]. The radiation-induced defects in the latter will originate a lattice volume change, which for GaN occurs only perpendicularly to the surface (for a-GaN, the expansion happens along the a-direction, and analogously for c-GaN along the c-direction) [31]. On reference [101], the authors suggest a possible variation of this substrate reaction for elastically anisotropic crystals, which is the case for a-GaN [47]. The experiments deliver the total strain directly (due to implantation and due to the substrate reaction). Although it is not possible, at this moment, to say if the higher strain measured in a-GaN is due to higher defect levels, different defect type or simply due to the substrate reaction, the total strain is higher and may influence defect migration in a different way than in c-GaN.

Figure 37 presents the DW factor profiles corresponding to the RaDMaX fits from Figure 34 and the strain profiles shown in Figure 36.

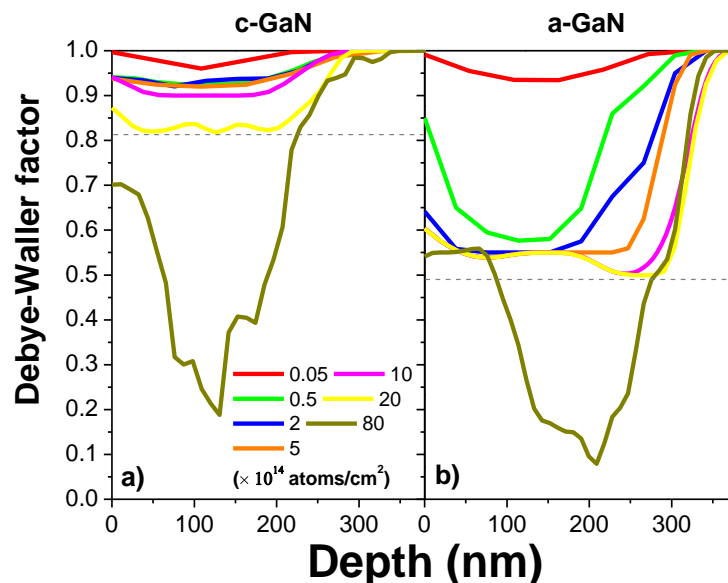


Figure 37 - DW factor profiles derived using the RaDMaX code for a) c-GaN and b) a-GaN as a function of depth, corresponding to the strain profiles presented in Figure 36. The range of 380 nm for the depth axis corresponds to the maximum argon atoms range obtained from SRIM simulations.

The variation of the DW factor (Figure 37), although not entirely a “mirror image”, supports the conclusions taken from the strain profiles presented in Figure 36: starting from the lowest fluence, there seems to be a decrease of the crystalline quality as the fluence rises, while the almost constant strain region is now equivalent to an almost constant DW factor value region. Results for 8×10^{15} at/cm² have a very high level of uncertainty given the fact XRD is no longer sensitive to such a high level of damage. This fluence shows the highest strain level in the experimental fits, but its low DW factor shows that the diffraction intensity is very low, thus the high uncertainty associated.

- Alternative fits

Further tests with the RaDMaX program showed that it is possible to fit the experimental data well by using quite different strain and DW profiles. Figure 38 presents examples of such different strain profiles for the a-GaN samples implanted with fluences ranging from 5×10^{13} at/cm² to 2×10^{15} at/cm², where a region with negative strain (indicating a contraction of the lattice parameter *a*) was considered to better fit the diffractograms at higher angles with respect to the main Bragg peak (Figure 39). This model is, however, questionable since the pronounced shoulder to the right side of the main Bragg peak is already present in the as-grown sample.

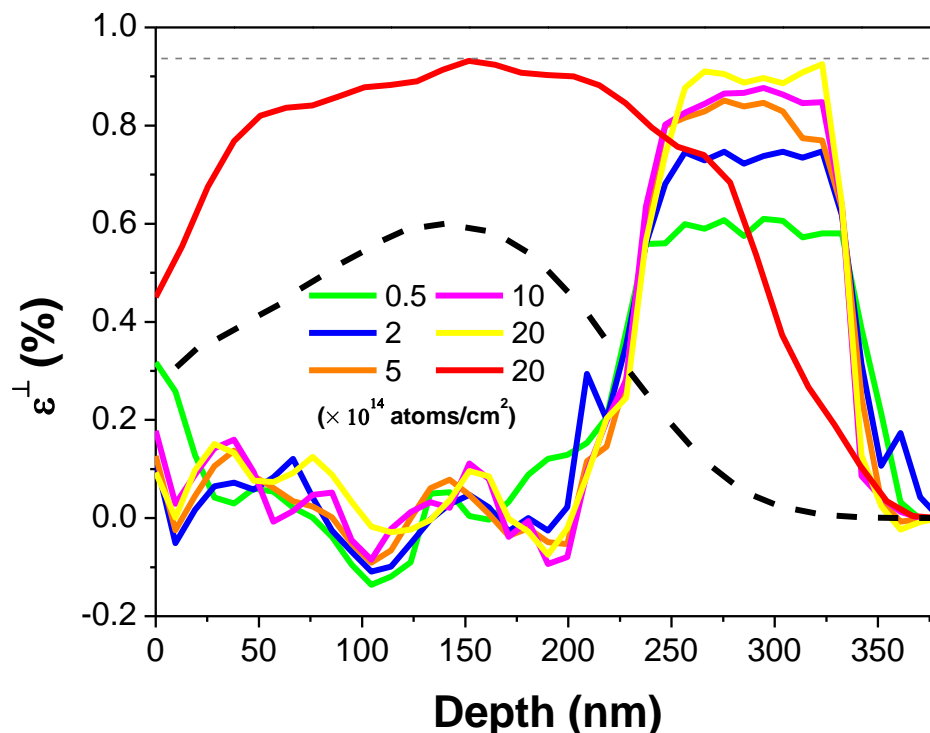


Figure 38 - Alternative strain profiles derived using the RaDMaX code for the fitting of the diffractograms of five a-GaN samples as a function of depth. The range of 380 nm for the depth axis corresponds to the maximum range of the argon atoms obtained from SRIM simulations. The SRIM vacancy-profile is included with arbitrary units. The red profile has been taken from Figure 36b for comparison.

Important similarities to note in both strain profiles from Figure 36b and Figure 38 are the increase of the strain with the fluence and the wide region where strain is approximately constant. In addition, the maximum strain value reached for all fluences is not only roughly the same for both strain

profiles but also in accordance with the experimental data. A crucial difference is, however, the considerable difference in the shape of the profiles in comparison with SRIM simulations, suggesting the bigger unlikelihood of this solution in comparison with the one presented in Figure 36 to describe the induced strain inside the analyzed samples.

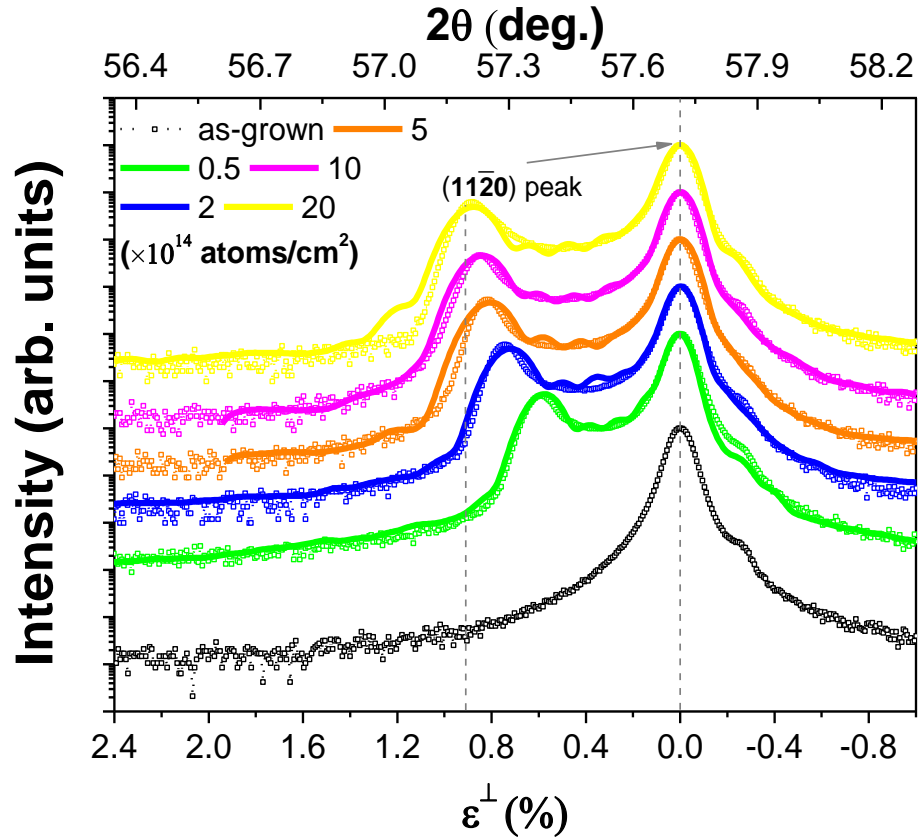


Figure 39 - Alternative RaDMaX fits to the diffractograms for a-GaN samples implanted with fluences ranging from 5×10^{13} at/cm² to 2×10^{15} at/cm², following the strain profiles presented in Figure 38.

The negative strain was considered due to the existence, shown in Figure 40 on the gray window, of a region in the diffractograms of the implanted samples where it is possible to identify differences with respect to the as-grown sample – suggesting the development of strain in this area. Its depth region was considered from suggestions taken from TEM analysis, pointing to the existence of vacancy-type defects close the surface [103] in AlN thick films. This has not, however, been observed for GaN so far. Furthermore, no clear dependence of the negative strain on the fluence was observed and the profile suggesting close to zero strain in most of the implanted volume does seem likely. Nevertheless, these tests showed how critical the fit results depend on the fitting model. On the other hand, they also show that the maximum strain values extracted from the fits are similar for different fitting models.

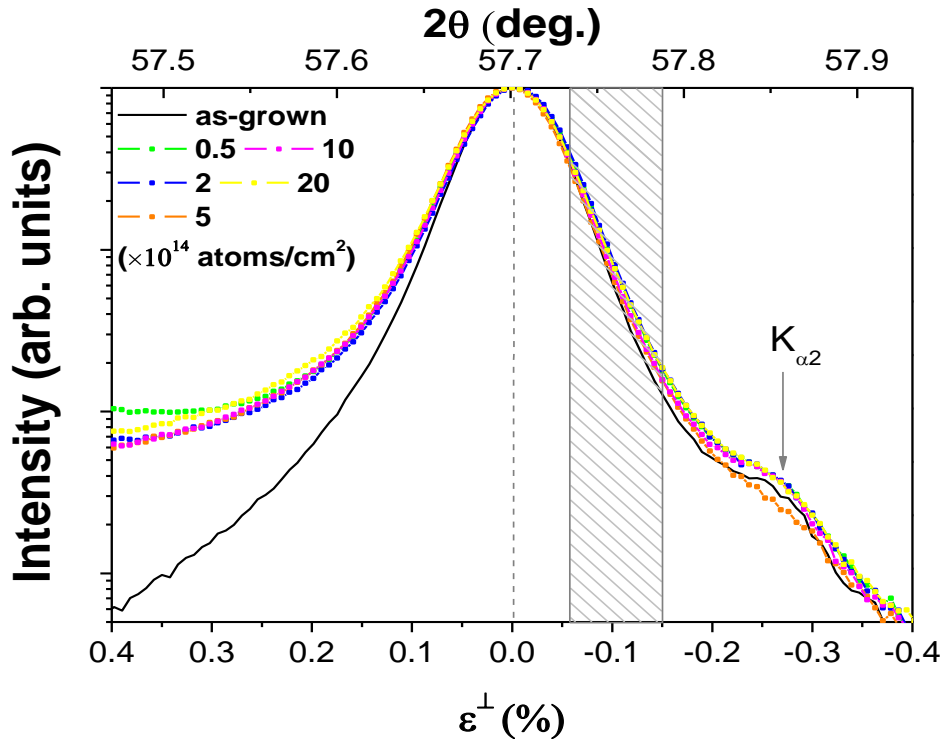


Figure 40 - Comparison of the experimental data with as-grown sample diffractograms for a-GaN. The grey window indicates the range where the negative strain values from all fluences showed in Figure 38 falls.

It is now time to see how do the alternative DW factor profiles, shown in Figure 41, evolve, corresponding to the a-GaN RaDMaX fits in Figure 39 and strain profiles from Figure 38.

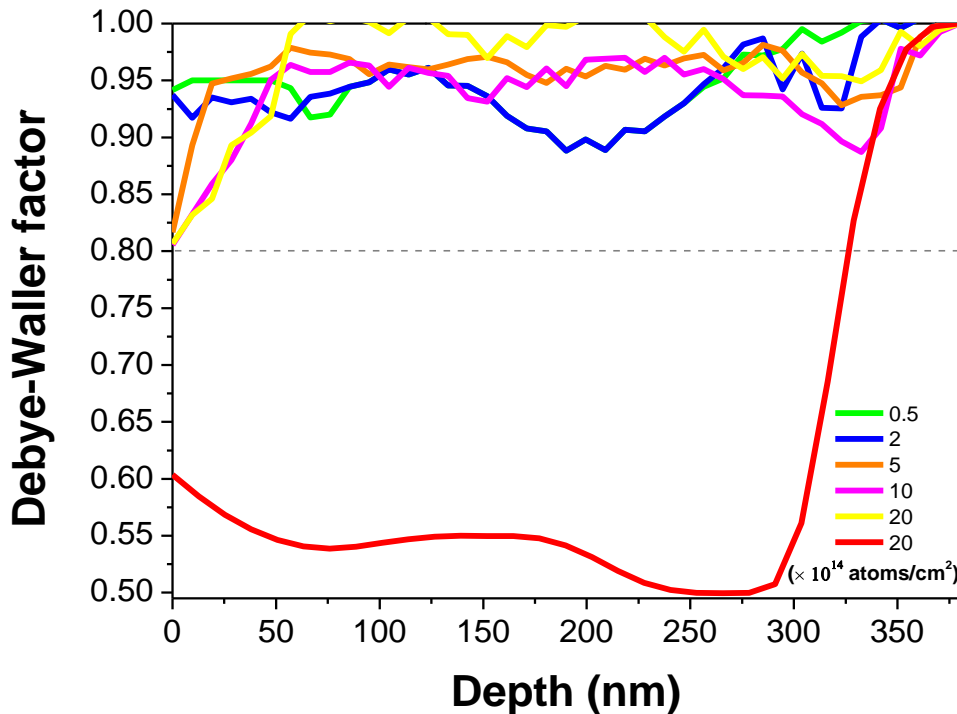


Figure 41 - Alternative DW Factor profiles for the fitting of the diffractograms of five a-GaN samples as a function of depth. The range of 380 nm for the depth axis corresponds to the maximum range Argon atoms reach from SRIM simulations. The red profile has been taken from Figure 37b for comparison.

While these profiles are more in accordance with the DW factor profiles presented for c-plane GaN samples showed in Figure 37a, their DW factor values do not constantly decrease as the fluence rises and they are significantly different from the profiles presented in Figure 37b – for example, for the fluence 2×10^{15} at/cm² as shown in Figure 41. These differences between DW factor values make it impossible to accurately compare c-plane and a-plane DW factor profiles.

4.1 Discussion

The use of complementary RBS/C and XRD techniques made it possible to compare them both, hoping to have a better understanding of the experimental results acquired. While RBS/C is more sensitive to the direct detection of displaced atoms inside the crystalline structure, XRD is sensitive to the distance in-between atomic planes; if there is still diffraction in the presence of defects, hence the complementarity of these techniques.

Figure 42 gives an overview of the main parameters extracted from both techniques, which allows a qualitative comparison of these. It shows the RDL and perpendicular strain as a function of the fluence for both materials orientations. As it has been shown that RaDMaX can accept more than one solution for the same experimental data, the choice for the strain profile here presented was made by taking into consideration the strain profiles which are coherent with SRIM simulations (the ones from Figure 36).

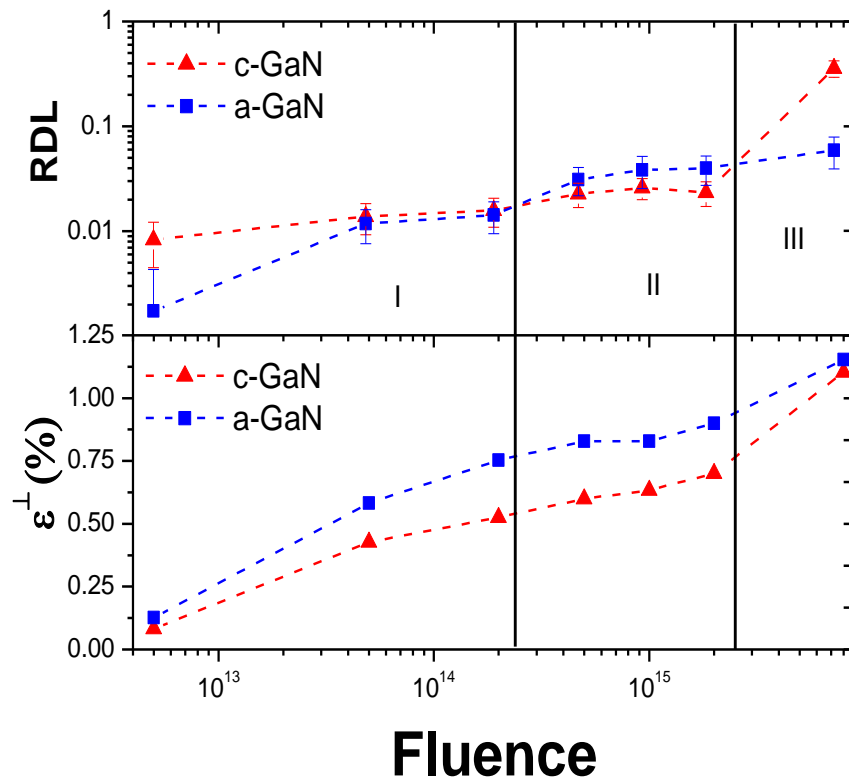


Figure 42 - RDL (relative defect level) and strain values for the depth window and regimes presented in Figure 32 as a function of the fluence.

Even though the RDL for our measurements is below the Hecking curves values at 15 K (Figure 33), our curves seem to follow the shapes of the curves at low temperature. These results are in accordance with the ones presented by Wendler *et al.* [14] and Turos [29]. They have compared damage build-up curves for Ar-implanted c-GaN at different temperatures and presented smaller and shifted values towards higher fluences at room temperature in comparison to implantation at 15 K, indicating not only a recombination of defects at room temperature but also that the transition between regimes occurs at a higher fluence. Both the strain and the relative defect level have been observed to increase with the ion fluence [27].

By relating the three regimes defined in Figure 32 and Figure 33 to their strain profiles, it is possible to observe a similar development for both planar orientations on the first two regimes: a first one where the increase of the strain is relatively linear as the implanted fluence rises, followed by a second one where the increase is smaller (corresponding to a saturation of the RDL).

For the third and last regime of fluence, there is a noticeably higher increase of RDL value observed for c-GaN implanted with 8×10^{15} at/cm² than for a-GaN implanted with the same fluence. In the meantime, the strain value for this fluence is nearly the same for both planar orientations. Given the fact that a-GaN presents a bigger strain value for the 2×10^{15} at/cm² fluence than c-GaN, its variation was bigger for c-GaN than for a-GaN in qualitative agreement with the RBS/C results. TEM images have shown a development of stacking faults and dislocation loops for the transition between these regimes II and III [11], [13], [29], which are different for different planar orientations [30]. The suggested hypothesis is that defect transformation occurs in the transition between regimes II and III, influencing drastically channeling through c-plane orientation but considerably less through a-plane orientation. The lower RDL for a-GaN can be a result of a more efficient transformation of point defects to extended defects, possibly enhanced by the higher strain values. However, the different types of defects created in a-GaN and c-GaN may have a different signature in the RBS/C spectrum, where direct backscattering is lower for a-GaN in comparison to c-GaN as it was also seen by Mackova *et al.* [99], [104]. They too have observed a lower damage accumulation level in the bulk of a-GaN after Kr and Gd implantation [99].

Figure 33 showed differences on the RDL values taken from RBS/C analysis for a-GaN and c-GaN for an implanted fluence of 8×10^{15} at/cm². Nevertheless, our XRD data shows similar behavior between the different planar orientations and thus it is not possible to conclude by itself that a-GaN is more resistant to implantation damage than c-GaN for the regime III, which has been previously reported as a consequence of a possible creation of different defect microstructures, following stronger dynamic annealing processes [30], [31].

Chapter 5 Conclusions

The main goal of this dissertation was to investigate the strain caused by ion implantation of 300 keV Argon ions in gallium nitride, for two planar orientations (a-plane and c-plane) and compare the strain evolution with the number of displaced atoms. Fourteen samples, seven for a-GaN and seven for c-GaN, were implanted in the same conditions at room temperature (RT), following a 7° angle with the surface normal and with fluences ranging from 5×10^{12} atoms/cm² to 8×10^{15} atoms/cm². Two analysis techniques were used, Rutherford Backscattering Spectrometry in the Channeling mode (RBS/C) and X-Ray Diffraction (XRD).

RBS/C results showed that the minimum yield calculated for as-grown samples of both planar orientations is in accordance with the typical state-of-art values for GaN films. After implantation, both planar orientations present slightly smaller values of Relative Defect Level (RDL) in comparison with corresponding Ar-ion fluences for low-temperature (LT) implantation at 15 K (Figure 33). Three damage build-up stages have been identified: a first where it is possible to identify an almost linear dependence of the RDL with the fluence, a second where a saturation of RDL occurs, and a third where a new steep increase occurs, which is considerably higher for c-GaN than for a-GaN. The damage build-up stages are very similar to those observed for LT implantation [30], however, the transition between damage build-up regimes occurs at slightly higher fluences for RT implantation than in the case of LT. This is attributed to a recombination of defects during the implantation (dynamic annealing) happening more efficiently at room temperature. The transition between the different stages occurs at approximately the same fluences for c-GaN and a-GaN. In fact, for the lower fluences no significant differences have been observed between c-plane and a-plane GaN, however, the latter is shown to register a considerably lower RDL at a fluence of 8×10^{15} atoms/cm², when entering the third regime of damage build-up. Similar results have been observed for LT implantation and were attributed to differences on the created defect microstructures following implantation where TEM analysis revealed the formation of mainly stacking faults for c-GaN and dislocation loops for a-GaN [30].

After implantation, XRD diffractograms show an expansion of the *c* lattice parameter in the implanted layer for c-GaN while for a-GaN the expansion happened for the *a* parameter – hence a perpendicular strain is observed in both cases and increases with increasing fluence. RaDMaX simulations were used for the fitting of the experimental data, however, it was shown that no unique solution for the strain and DW factor profiles can be found. The fitting model presented in this thesis follows the profile obtained from SRIM simulations. Another model considering a negative deformation close to the surface on five a-plane implanted samples was considered less viable. Despite the ambiguities in the fitting models, it was demonstrated that the maximum strain could be readily extracted from the simulations. This maximum strain was seen to be higher for a-GaN than for c-GaN in the entire analyzed fluence region. Furthermore, the three regimes defined for the RBS/C data are well resolved in the XRD analysis where strain is seen to increase with different rates for the three

fluence regimes. Indeed, XRD is very sensitive to the strain incorporated by implantation effects for low fluences while RBS/S suffers from low statistics for the lowest fluences.

A qualitative interpretation and comparison of the results given by both techniques and literature data allow one to speculate, that the induced strain caused by implantation may indeed be the driving force for defect transformation as proposed by Turos [29] and Wendler *et al.* for c-GaN [14]. First, it was shown that the defect accumulation follows a similar mechanism at 15 K and RT both for c-GaN and a-GaN. Since at 15 K thermal effects are minimized it is fair to assume that temperature is not the main driving force leading to the transformation of point defects and their clusters to stacking faults (in c-GaN) and dislocation loops (in a-GaN) [30]. Since in the present study implantation was performed at RT, the delay to higher fluences of this transformation can be explained by enhanced dynamic annealing. Like this, the critical defect density/critical strain at which defect transformation occurs is only reached for higher fluences. One indication that strain rather than defect density is responsible for this transformation is the fact that dynamic annealing is stronger in a-GaN (leading to lower RDL and lower strain increase for the highest fluence) which has higher strain levels for the previous fluences. Assuming that the same kind of defects are produced for the lower fluences in both materials and knowing that the implantation was performed at the same temperature, it is fair to assume that the different defect structures observed in [30] are caused by the different strain states in the two materials, in particular, the anisotropic strain expected in a-GaN [47].

Properties that depend on individual behaviors of single particles will be affected by point defects (and by others), for example, the electron mobility – thus, the electrical conductivity. Regarding properties that depend on collective behaviors and a long-range order, these will be less affected by point defects and more by the dilatation phenomenon (which preserves the order but may introduce anisotropy).

The ultimate proof to confirm that strain as the driving force of damage accumulation was not possible to deliver within the restricted time frame of this thesis. Possible future work to contribute to clarifying the validity of this hypothesis include the study of damage and strain build-up following implantation at different temperatures. This would provide the possibility to study whether the transition between damage build-up regimes takes place, for different implantation temperatures, at the same strain value. To avoid the transformation of point defects to thermally stable extended defects, the fluences should be chosen to stay below the critical fluence corresponding to the third regime of damage accumulation described above. If higher fluences are necessary for the targeted application, methods for strain relaxation should be developed that avoid the transformation to stacking faults and dislocation loops.

Practical applications of this study include the development of electronics based on GaN, which is among the most popular wide band gap materials currently under research.

References

- [1] W. C. Johnson, J. B. Parson, and M. C. Crew, "Nitrogen Compounds of Gallium. III," *J. Phys. Chem.*, vol. 36, no. 10, pp. 2651–2654, 1932.
- [2] S. Nakamura and S. F. Chichibu, *Introduction to Nitride Semiconductor Blue Lasers and Light Emitting Diodes*. Boca Raton, FL: CRC Press, 2000.
- [3] "The Official Web Site of the Nobel Prize," *Physics category*. [Online]. Available: https://www.nobelprize.org/nobel_prizes/physics/laureates/2014/. [Accessed: 27-Mar-2018].
- [4] F. A. Ponce and D. P. Bour, "Nitride based semiconductors for blue and green light-emitting devices," *Nature*, vol. 386, pp. 351–359, 1997.
- [5] T. Mimura, "The early History of the High Electron Mobility Transistor (HEMT)," *IEEE Trans. Microw. Theory Tech.*, vol. 50, no. 3, pp. 780–782, 2002.
- [6] A. Lidow, J. Strydom, M. de Rooij, and D. Reusch, *GaN Transistors for Efficient Power Conversion*, 2nd Editio. Hoboken, NJ: Wiley, 2014.
- [7] H. Amano, N. Sawaki, I. Akasaki, and Y. Toyoda, "Metalorganic vapor phase epitaxial growth of a high quality GaN film using an AlN buffer layer," *Appl. Phys. Lett.*, vol. 48, no. 5, pp. 353–355, 1986.
- [8] A. Lidow, "GaN transistors - Giving new life to Moore's Law," *Proc. Int. Symp. Power Semicond. Devices ICs*, vol. 2015–June, pp. 1–6, 2015.
- [9] G. E. Moore, "Craming more components onto integrated circuits," *Electronics*, vol. 38, no. 8, pp. 114–117, 1965.
- [10] M. A. Nastasi and J. W. Mayer, *Ion Implantation and Synthesis of Materials*. Berlin Heidelberg: Springer, 2006.
- [11] K. Pągowska, R. Ratajczak, A. Stonert, A. Turos, L. Nowicki, N. Sathish, P. Jóźwik, and A. Muecklich, "RBS/channeling and TEM study of damage buildup in ion bombarded GaN," *Acta Phys. Pol. A*, vol. 120, no. 1, pp. 153–155, 2011.
- [12] B. Lacroix, S. Leclerc, A. Declémy, K. Lorenz, E. Alves, and P. Ruterana, "Mechanisms of damage formation in Eu-implanted GaN probed by X-ray diffraction," *J. Appl. Phys.*, vol. 112, no. 7, 2011.
- [13] P. Ruterana, B. Lacroix, and K. Lorenz, "A mechanism for damage formation in GaN during rare earth ion implantation at medium range energy and room temperature," *J. Appl. Phys.*, vol. 109, no. 1, 2011.

- [14] E. Wendler, W. Wesch, A. Y. Azarov, N. Catarino, A. Redondo-Cubero, E. Alves, and K. Lorenz, "Comparison of low-and room-temperature damage formation in Ar ion implanted GaN and ZnO," *Nucl. Instruments Methods Phys. Res. Sect. B Beam Interact. with Mater. Atoms*, vol. 307, pp. 394–398, 2013.
- [15] A. Turos, P. Jozwik, L. Nowicki, and N. Sathish, "Ion channeling study of defects in compound crystals using Monte Carlo simulations," *Nucl. Instruments Methods Phys. Res. Sect. B Beam Interact. with Mater. Atoms*, vol. 332, pp. 50–55, 2014.
- [16] W.-K. Chu, J. W. Mayer, and M.-A. Nicolet, *Backscattering Spectrometry*. Orlando: Academic Press, 1978.
- [17] M. A. Nastasi and J. R. Tesmer, *Handbook of Modern Ion Beam Materials Analysis*. Pittsburgh: Materials Research Society, 1995.
- [18] P. F. Fewster, *X-Ray Scattering from Semiconductors*. Imperial College Press, 2003.
- [19] M. A. Moram and M. E. Vickers, "X-ray diffraction of III-nitrides," *Reports Prog. Phys.*, vol. 72, no. 3, 2009.
- [20] J. I. Pankove and J. A. Hutchby, "Photoluminescence of Zn-implanted GaN," *Appl. Phys. Lett.*, vol. 24, no. 6, pp. 281–283, 1974.
- [21] H. H. Tan, J. S. Williams, J. Zou, D. J. H. Cockayne, S. J. Pearton, J. C. Zolper, and R. A. Stall, "Annealing of ion implanted gallium nitride," *Appl. Phys. Lett.*, vol. 72, no. 10, pp. 1190–1192, 1998.
- [22] E. V Kalinina, A. S. Zubrilov, A. M. Strel'chuk, V. A. Solov'ev, and V. A. Dmitriev, "Electrical and optical properties of Mg ion implanted GaN p-n junctions," in *HITEN 99. Third European Conference on High Temperature Electronics*, 1999, pp. 91–94.
- [23] S. O. Kucheyev, J. S. Williams, and S. J. Pearton, "Ion implantation into GaN," *Mater. Sci. Eng. R Reports*, vol. 33, no. 2–3, pp. 51–107, 2001.
- [24] A. Vantomme, S. M. Hogg, M. F. Wu, B. Pipeleers, M. Swart, S. Goodman, D. Auret, K. lakoubovskii, G. J. Adriaenssens, K. Jacobs, and I. Moerman, "Suppression of rare-earth implantation-induced damage in GaN," *Nucl. Instruments Methods Phys. Res. Sect. B Beam Interact. with Mater. Atoms*, vol. 175–177, pp. 148–153, 2001.
- [25] J. Nord, K. Nordlund, J. Keinonen, and K. Albe, "Molecular dynamics study of defect formation in GaN cascades," *Nucl. Instruments Methods Phys. Res. Sect. B Beam Interact. with Mater. Atoms*, vol. 202, pp. 93–99, 2003.
- [26] S. O. Kucheyev, J. S. Williams, J. Zou, and C. Jagadish, "Dynamic annealing in III-nitrides under ion bombardment," *J. Appl. Phys.*, vol. 95, no. 6, pp. 3048–3054, 2003.

- [27] B. Pipeleers, S. M. Hogg, and A. Vantomme, "Defect accumulation during channeled erbium implantation into GaN," *J. Appl. Phys.*, vol. 98, no. 12, 2005.
- [28] F. Gloux, T. Wojtowicz, P. Ruterana, K. Lorenz, and E. Alves, "Transmission electron microscopy investigation of the structural damage formed in GaN by medium range energy rare earth ion implantation," *J. Appl. Phys.*, vol. 100, no. 7, 2006.
- [29] A. Turos, "On the mechanism of damage build-up in GaN," *Radiat. Eff. Defects Solids*, vol. 168, no. 6, pp. 431–441, 2013.
- [30] K. Lorenz, E. Wendler, A. Redondo-Cubero, N. Catarino, M. P. Chauvat, S. Schwaiger, F. Scholz, E. Alves, and P. Ruterana, "Implantation damage formation in a-, c- and m-plane GaN," *Acta Mater.*, vol. 123, pp. 177–187, 2017.
- [31] N. Catarino, E. Nogales, N. Franco, V. Darakchieva, S. M. C. Miranda, B. Méndez, E. Alves, J. G. Marques, and K. Lorenz, "Enhanced dynamic annealing and optical activation of Eu implanted a-plane GaN," *Epl*, vol. 97, no. 6, 2012.
- [32] T. Paskova, *Nitrides with Nonpolar Surfaces*. Weinheim: Wiley-VCH, 2008.
- [33] Y. Taniyasu and M. Kasu, "Improved emission efficiency of 210-nm deep-ultraviolet aluminum nitride light-emitting diode," *NTT Tech. Rev.*, vol. 8, no. 8, 2010.
- [34] B. Gil, *Physics of Wurtzite Nitrides and Oxides*. Cham: Springer, 2014.
- [35] M. Grundmann, *The Physics of Semiconductors: An Introduction Including Nanophysics and Applications*, 2nd ed. Berlin: Springer-Verlag Berlin and Heidelberg GmbH & Co. KG, 2010.
- [36] T. Detchprohm, K. Hiramatsu, K. Itoh, and I. Akasaki, "Relaxation Process of the Thermal Strain in the GaN/Alpha-Al₂O₃ Heterostructure and Determination of the Intrinsic Lattice-Constants of GaN Free From the Strain," *Japanese J. Appl. Phys. Part 2-Letters*, vol. 31, pp. L1454–L1456, 1992.
- [37] H. Morkoç, *Handbook of Nitride Semiconductors and Devices, Volume 1: Materials Properties, Physics and Growth*. Wiley-VCH, 2008.
- [38] M. Leszczynski, H. Teisseyre, T. Suski, I. Grzegory, M. Bockowski, J. Jun, S. Porowski, K. Pakula, J. M. Baranowski, C. T. Foxon, and T. S. Cheng, "Lattice parameters of gallium nitride," *Appl. Phys. Lett.*, vol. 69, no. 1, pp. 73–75, 1996.
- [39] H. P. Maruska and J. J. Tietjen, "The preparation and properties of vapor-deposited single-crystal-line GaN," *Appl. Phys. Lett.*, vol. 15, no. 10, pp. 327–329, 1969.
- [40] D. Kotchetkov, J. Zou, A. A. Balandin, D. I. Florescu, and F. H. Pollak, "Effect of dislocations on thermal conductivity of GaN layers," *Appl. Phys. Lett.*, vol. 79, no. 26, pp. 4316–4318, 2001.

- [41] J. Zou, D. Kotchetkov, A. A. Balandin, D. I. Florescu, and F. H. Pollak, "Thermal conductivity of GaN films: Effects of impurities and dislocations," *J. Appl. Phys.*, vol. 92, no. 5, pp. 2534–2539, 2002.
- [42] J. Jasinski, D. N. Zakharov, and L. Berkeley, "GaN grown in polar and non-polar directions," *Opto-Electronics Rev.*, vol. 12, no. 4, pp. 339–346, 2004.
- [43] A. Chakraborty, K. C. Kim, F. Wu, J. S. Speck, S. P. DenBaars, and U. K. Mishra, "Defect reduction in nonpolar a-plane GaN films using in situ SiN_x nanomask," *Appl. Phys. Lett.*, vol. 89, no. 4, 2006.
- [44] J. Hertkorn, P. Brückner, S. B. Thapa, T. Wunderer, F. Scholz, M. Feneberg, K. Thonke, R. Sauer, M. Beer, and J. Zweck, "Optimization of nucleation and buffer layer growth for improved GaN quality," *J. Cryst. Growth*, vol. 308, no. 1, pp. 30–36, 2007.
- [45] J. Hertkorn, F. Lipski, P. Brückner, T. Wunderer, S. B. Thapa, F. Scholz, A. Chuvilin, U. Kaiser, M. Beer, and J. Zweck, "Process optimization for the effective reduction of threading dislocations in MOVPE grown GaN using in situ deposited SiN_x masks," *J. Cryst. Growth*, vol. 310, no. 23, pp. 4867–4870, 2008.
- [46] F. Bernardini and V. Fiorentini, "Macroscopic polarization and band offsets at nitride heterojunctions," *Phys. Rev. B - Condens. Matter Mater. Phys.*, vol. 57, no. 16, pp. R9427–R9430, 1998.
- [47] T. Paskova, V. Darakchieva, P. P. Paskov, J. Birch, E. Valcheva, P. O. A. Persson, B. Arnaudov, S. Tungasmita, and B. Monemar, "Properties of nonpolar a-plane GaN films grown by HVPE with AlN buffers," *J. Cryst. Growth*, vol. 281, no. 1, pp. 55–61, 2005.
- [48] P. Waltereit, O. Brandt, A. Trampert, H. T. Grahn, J. Monniger, M. Ramsteiner, M. Relche, and K. H. Ploog, "Nitride semiconductors free of electrostatic fields for efficient white light-emitting diodes," *Nature*, vol. 406, no. 6798, pp. 865–868, 2000.
- [49] S. J. Pearton, *Optoelectronic Properties of Semiconductors and Superlattices - GaN and Related Materials II*. Amsterdam: Gordon and Breech Science Publishers, 2000.
- [50] J. Chen, "Radiation Response and Reliability of AlGaIn/GaN HEMTS," M.Sc. thesis, Vanderbilt University, 2013.
- [51] Ioffe Institute - St. Petersburg, "GaN - Gallium Nitride." [Online]. Available: <http://www.ioffe.ru/SVA/NSM/Semicond/GaN>. [Accessed: 03-Apr-2018].
- [52] E. Wendler, A. Kamarou, E. Alves, K. Gärtner, and W. Wesch, "Three-step amorphisation process in ion-implanted GaN at 15 K," *Nucl. Instruments Methods Phys. Res. Sect. B Beam Interact. with Mater. Atoms*, vol. 206, pp. 1028–1032, 2003.

- [53] E. Alves, E. Rita, U. Wahl, J. G. Correia, T. Monteiro, J. Soares, and C. Boemare, "Lattice site location and optical activity of Er implanted ZnO," *Nucl. Instruments Methods Phys. Res. Sect. B Beam Interact. with Mater. Atoms*, vol. 206, pp. 1047–1051, 2003.
- [54] S. O. Kucheyev, J. S. Williams, and C. Jagadish, "Ion-beam-defect processes in group-III nitrides and ZnO," *Vacuum*, vol. 73, no. 1, pp. 93–104, 2003.
- [55] Z. Y. Gao, X. W. Xue, J. J. Li, X. Wang, Y. H. Xing, B. F. Cui, and D. S. Zou, "Understanding of surface pit formation mechanism of GaN grown in MOCVD based on local thermodynamic equilibrium assumption," *Chinese Phys. B*, vol. 25, no. 6, 2016.
- [56] I. G. Batyrev, W. L. Sarney, T. S. Zheleva, C. Nguyen, B. M. Rice, and K. A. Jones, "Dislocations and stacking faults in hexagonal GaN," *Phys. Status Solidi Appl. Mater. Sci.*, vol. 208, no. 7, pp. 1566–1568, 2011.
- [57] T. Wójtowicz, F. Gloux, P. Ruterana, K. Lorenz, and E. Alves, "TEM investigation of Tm implanted GaN, the influence of high temperature annealing," *Opt. Mater. (Amst)*, vol. 28, no. 6–7, pp. 738–741, 2006.
- [58] "Stacking Fault Energy." [Online]. Available: <http://en.stonkcash.com/stacking-fault-energy/>. [Accessed: 28-Mar-2018].
- [59] J. Lähnemann, U. Jahn, O. Brandt, T. Flissikowski, P. Dogan, and H. T. Grahn, "Luminescence associated with stacking faults in GaN," *J. Phys. D. Appl. Phys.*, vol. 47, no. 42, 2014.
- [60] C. Liu, B. Mensching, K. Volz, and B. Rauschenbach, "Lattice expansion of Ca and Ar ion implanted GaN," *Appl. Phys. Lett.*, vol. 71, no. 16, pp. 2313–2315, 1997.
- [61] D. N. Faye, E. Wendler, M. Felizardo, S. Magalhães, E. Alves, F. Brunner, M. Weyers, and K. Lorenz, "Mechanisms of Implantation Damage Formation in $\text{Al}_x\text{Ga}_{1-x}\text{N}$ Compounds," *J. Phys. Chem. C*, vol. 120, no. 13, pp. 7277–7283, 2016.
- [62] S. Magalhães, M. Fialho, M. Peres, K. Lorenz, and E. Alves, "Quantitative x-ray diffraction analysis of bimodal damage distributions in Tm implanted $\text{Al}_{0.15}\text{Ga}_{0.85}\text{N}$," *J. Phys. D. Appl. Phys.*, vol. 49, no. 13, p. 135308, 2016.
- [63] M. Fialho, S. Magalhães, M. P. Chauvat, P. Ruterana, K. Lorenz, and E. Alves, "Impact of implantation geometry and fluence on structural properties of $\text{Al}_x\text{Ga}_{1-x}\text{N}$ implanted with thulium," *J. Appl. Phys.*, vol. 120, no. 16, p. 165703, 2016.
- [64] S. Pereira, M. R. Correia, E. Pereira, K. P. O'Donnell, E. Alves, A. D. Sequeira, N. Franco, I. M. Watson, and C. J. Deatcher, "Strain and composition distributions in wurtzite InGaN/GaN layers extracted from x-ray reciprocal space mapping," *Appl. Phys. Lett.*, vol. 80, no. 21, pp. 3913–3915, 2002.

- [65] A. Boulle, R. Guinebretière, and A. Dauger, “Phenomenological analysis of heterogeneous strain fields in epitaxial thin films using x-ray scattering,” *J. Phys. D. Appl. Phys.*, vol. 38, no. 21, pp. 3907–3920, 2005.
- [66] A. Debelle and A. Declémy, “XRD investigation of the strain/stress state of ion-irradiated crystals,” *Nucl. Instruments Methods Phys. Res. Sect. B Beam Interact. with Mater. Atoms*, vol. 268, no. 9, pp. 1460–1465, 2010.
- [67] M. Souilah, A. Boulle, and A. Debelle, “RaDMaX: A graphical program for the determination of strain and damage profiles in irradiated crystals,” *J. Appl. Crystallogr.*, vol. 49, pp. 311–316, 2016.
- [68] A. Turos, P. Jóźwik, M. Wójcik, J. Gaca, R. Ratajczak, and A. Stonert, “Mechanism of damage buildup in ion bombarded ZnO,” *Acta Mater.*, vol. 134, pp. 249–256, 2017.
- [69] A. Debelle, J.-P. Crocombette, A. Boulle, A. Chartier, T. Jourdan, S. Pellegrino, D. Bachiller-Perea, D. Carpentier, J. Channagiri, T.-H. Nguyen, F. Garrido, and L. Thomé, “Lattice strain in irradiated materials unveils a prevalent defect evolution mechanism,” *Phys. Rev. Mater.*, vol. 2, no. 1, p. 13604, 2018.
- [70] E. Wendler, “Mechanisms of damage formation in semiconductors,” *Nucl. Instruments Methods Phys. Res. Sect. B Beam Interact. with Mater. Atoms*, vol. 267, no. 16, pp. 2680–2689, 2009.
- [71] N. Hecking, K. F. Heidemann, and E. Te Kaat, “Model of temperature dependent defect interaction and amorphization in crystalline silicon during ion irradiation,” *Nucl. Inst. Methods Phys. Res. B*, vol. 15, no. 1–6, pp. 760–764, 1986.
- [72] K. Lorenz, U. Wahl, E. Alves, T. Wojtowicz, P. Ruterana, S. Ruffenach, and O. Briot, “Amorphisation of GaN during processing with rare earth ion beams,” *Superlattices Microstruct.*, vol. 36, no. 4–6, pp. 737–745, 2004.
- [73] H. M. Manasevit, “Single-crystal gallium arsenide on insulating substrates,” *Appl. Phys. Lett.*, vol. 12, no. 4, pp. 156–159, 1968.
- [74] R. Waser, *Nanoelectronics and Information Technology - Advanced Electronic Materials and Novel Devices*. Weinheim: Wiley-VCH GmbH & Co. KgaA, 2003.
- [75] F. Scholz, P. Brückner, F. Habel, M. Peter, and K. Köhler, “Improved GaN layer morphology by hydride vapor phase epitaxy on misoriented Al₂O₃wafers,” *Appl. Phys. Lett.*, vol. 87, no. 18, pp. 1–3, 2005.
- [76] S. Schwaiger, F. Lipski, T. Wunderer, and F. Scholz, “Influence of slight misorientations of r-plane sapphire substrates on the growth of nonpolar a-plane GaN layers via HVPE,” *Phys. Status Solidi C*, vol. 7, no. 7–8, pp. 2069–2072, 2010.
- [77] J. F. Ziegler, M. D. Ziegler, and J. P. Biersack, “SRIM - The Stopping and Range of Ions in Matter,” *Nucl. Instr. Meth. B*, vol. 268, pp. 1818–1823, 2010.

- [78] B. R. Nielsen, P. Abrahamsen, and S. Eriksen, "A universal high-current implanter for surface modification of materials," *Mater. Sci. Eng. A*, vol. 116, no. C, pp. 193–196, 1989.
- [79] L. M. Redondo, J. Rocha, and J. C. Soares, "A low-cost, accurate and non-intercepting continuous method for beam current measurements in a high-current ion implanter," *Nucl. Instruments Methods Phys. Res. Sect. B Beam Interact. with Mater. Atoms*, vol. 265, no. 2, pp. 576–580, 2007.
- [80] J. F. Ziegler, *The Stopping and Range of Ions in Solids*. Pergamon Press, 1985.
- [81] N. P. Barradas and E. Alves, "Advanced characterization of nanomaterials with ion beams," *Res. Signpost*, vol. 37/661, no. 2, 2008.
- [82] G. Schatz and A. Weidinger, *Nuclear Condensed Matter Physics: Nuclear Methods and Applications*. Chichester: Wiley, 1996.
- [83] N. Catarino, "Caracterização de danos e activação óptica de európio implantado em nitreto de gálio polar e não-polar," M.Sc. thesis, Faculdade de Ciências da Universidade de Lisboa, 2011.
- [84] R. M. C. Silva, "Estudo por RBS e canalização iónica de ligas de Mg, Al e Fe formadas por implantação iónica," Ph.D. thesis, Universidade de Lisboa, 1993.
- [85] E. Bøgh, "Defect studies in crystals by means of channeling," *Can. J. Phys.*, vol. 46, no. 6, pp. 653–662, 1968.
- [86] G. Götz and K. Gärtner, *High energy ion beam analysis of solids*. Berlin: Akademie-Verlag, 1988.
- [87] E. Wendler, W. Wesch, and G. Götz, "Radiation damage and optical properties of Ar⁺-implanted GaP," *J. Appl. Phys.*, vol. 70, no. 1, pp. 144–149, 1991.
- [88] M. Hrabak, R. S. Padovan, M. Kralik, D. Ozretic, and K. Potocki, "Nikola Tesla and the Discovery of X-rays," *RadioGraphics*, vol. 28, no. 4, pp. 1189–1192, 2008.
- [89] W. L. Bragg, "The Diffraction of Short Electromagnetic Waves by a Crystal," *Proc. Cambridge Phil. Soc.*, vol. 17, pp. 43–57, 1913.
- [90] N. Waeselmann, "Structural transformations in complex perovskite-type relaxor and relaxor-based ferroelectrics at high pressures and temperatures," Ph.D. thesis, Universität Hamburg, 2012.
- [91] W. J. Bartels, J. Hornstra, and D. J. W. Lobeek, "X-ray diffraction of multilayers and superlattices," *Acta Crystallogr. Sect. A*, vol. 42, no. 6, pp. 539–545, 1986.
- [92] V. S. Speriosu, "Kinematical X-ray diffraction in nonuniform crystalline films: Strain and damage distributions in ion-implanted garnets," *J. Appl. Phys.*, vol. 52, pp. 6094–6103, 1981.

- [93] H. Behr, H. Metzger, and J. Peisl, "The Debye-Waller factor due to static displacement around hydrogen in niobium," *J. Less-Common Met.*, vol. 88, no. 1, pp. 159–164, 1982.
- [94] C. Tsallis and D. A. Stariolo, "Generalized simulated annealing," *Phys. A Stat. Mech. its Appl.*, vol. 233, no. 1–2, pp. 395–406, 1996.
- [95] K. Levenberg, "A Method for the Solution of Certain Non-Linear Problems in Least," *Q. Appl. Math.*, vol. 2, no. 278, pp. 164–168, 1944.
- [96] D. Marquardt, "An Algorithm for Least-Squares Estimation of Nonlinear Parameters," *SIAM J. Appl. Math.*, vol. 11, no. 2, pp. 431–441, 1963.
- [97] E. T. Yu and M. O. Manasreh, *III-V Nitride Semiconductors: Applications and Devices*. New York: Taylor & Francis, 2003.
- [98] Y. Zhang, I. T. Bae, K. Sun, C. Wang, M. Ishimaru, Z. Zhu, W. Jiang, and W. J. Weber, "Damage profile and ion distribution of slow heavy ions in compounds," *J. Appl. Phys.*, vol. 105, no. 10, 2009.
- [99] A. Macková, P. Malinský, A. Jágerová, Z. Sofer, K. Klímová, D. Sedmidubský, M. Mikulics, R. Böttger, and S. Akhmaliev, "Damage accumulation and structural modification in c-plane and a-plane GaN implanted with 400 keV Kr and Gd ions," *Surf. Coatings Technol.*, no. January, pp. 0–1, 2018.
- [100] Y. Zhang, M. Ishimaru, J. Jagielski, W. Zhang, Z. Zhu, L. V. Saraf, W. Jiang, L. Thome, and W. J. Weber, "Damage and microstructure evolution in GaN under Au ion irradiation," *J. Phys. D. Appl. Phys.*, vol. 43, no. 8, 2010.
- [101] A. Debelle, A. Boule, F. Rakotovao, J. Moeyaert, C. Bachelet, F. Garrido, and L. Thomé, "Influence of elastic properties on the strain induced by ion irradiation in crystalline materials," *J. Phys. D. Appl. Phys.*, vol. 46, no. 4, 2013.
- [102] S. I. Rao and C. R. Houska, "Residual stress gradients along ion implanted zones - cubic crystals," *J. Mater. Sci.*, vol. 25, no. 6, pp. 2822–2826, 1990.
- [103] S. Leclerc, B. Lacroix, A. Declémy, K. Lorenz, and P. Ruterana, "Mechanisms of damage formation in Eu-implanted AlN," *J. Appl. Phys.*, vol. 112, no. 7, pp. 0–5, 2012.
- [104] A. Macková, P. Malinský, A. Jágerová, Z. Sofer, K. Klímová, D. Sedmidubský, M. Pristovsek, M. Mikulics, J. Lorinčík, R. Böttger, and S. Akhmaliev, "Structural and optical properties of Gd implanted GaN with various crystallographic orientations," *Thin Solid Films*, vol. 638, pp. 63–72, 2017.